SYNTHESIS AND MAGNETIC CHARACTERIZATION OF EPITAXIAL MnGe THIN FILMS ON Si(111)

by

Brett D. MacNeil

Submitted in partial fulfillment of the requirements
for the degree of Master of Science

at

Dalhousie University
Halifax, Nova Scotia
December 2023

To my wife, Alex.

Table of Contents

List of Figures

Abstract

Magnets with broken inversion symmetry possess a chiral interaction that leads to twisting of the magnetic structures. The cubic B20 compounds which include MnSi and FeGe are archetypal chiral magnets where twisting of the magnetization leads to the formation of localized two-dimensional textures known as skyrmions. MnGe is a much less understood member of the B20 family of chiral magnets, in part due to the challenges in synthesizing this metastable material. It is unique as it is proposed to host three-dimensional textures known as spin-hedgehogs.

While others have grown MnGe thin films on magnetic MnSi and FeGe template layers, it is demonstrated in this thesis that a paramagnetic template layer of B20 CrSi serves as a good epitaxial seed layer from the nucleation and growth of B20 MnGe. Smooth, ultrathin CrSi films were produced Si(111) by applying a technique developed for MnSi.

MnGe(111) thin films were grown with thickness ranging from 2 nm to 40 nm, a range that has not been explored in-depth in the literature. The films were characterized using reflection high energy electron diffraction (RHEED), atomic force microscopy (AFM), X-ray diffraction (XRD) and X-ray reflectometry (XRR). It was found in this thesis that growth yielded single phase MnGe(111) films with roughness less than 6 Å that are suitable for further characterization with polarized neutron reflectometry (PNR) or synchrotron X-ray scattering.

Magnetometry measurements were conducted and reveal that the ground state is a helical modulation which is distorted into a helicoidal state for field applied along $[1\bar{1}0]$ (in-plane), or a conical state for field applied along [111] (out-of-plane). Magnetometry did not show evidence for a three-dimensional hedgehog state like reported by others. Magnetotransport for out-of-plane fields indicates the presence of an additional low-temperature phase which is not observed in the magnetometry. The true nature of this state remains unknown, but it is proposed to be a topological spin-hedgehog lattice, or a multi-domain helical state. Neutron or resonant X-ray scattering experiments are necessary to determine the magnetic structure of this phase and why it is not evidenced by magnetometry.

List of Abbreviations and Symbols Used

AFM: atomic force microscopy

DMI: Dzyaloshinskii-Moriya interaction

EMF: electromotive force

FWHM: full width at half maximum

GMR: giant magnetoresistance

LEED: low energy electron diffraction

LTEM: Lorentz transmission electron microscopy

MBE: molecular beam epitaxy

MPMS: magnetic properties measurement system

PNR: polarized neutron reflectometry

PPMS: physical properties measurement system

QL: quadruple layer

RHEED: reflection high energy electron diffraction

RMS: root mean square

RRR: residual resistivity ratio

RSO: reciprocating sample option

SANS: small-angle neutron scattering

SLD: scattering length density

SP-STM: spin-polarized scanning tunneling microscopy

SQUID: superconducting quantum interference device

STM: scanning tunneling microscopy

STT: spin transfer torque

UHV: ultra high vacuum

XPS: X-ray photoelectron spectroscopy

XRD: X-ray diffraction

XRR: X-ray reflectometry

A: continuum exchange constant

a: lattice parameter

$\mathbf{a}_i$, $\mathbf{b}_i$, $\mathbf{q}_i$: hedgehog modulation vectors

$\mathbf{B}$: magnetic field

$B(2\theta)$, b_i: XRD background function, its parameters

$\mathbf{D}$, D: Dzyaloshinskii vector, continuum Dzyaloshinskii constant

d: sample position in SQUID magnetometer

$d_{h,k,\ell}$: plane spacing

d_{f}: film thickness

d_{k}: kinetic diameter

$\mathbf{E}$: electric field

E: energy $\mathbf{F}$: force

$|F|$: structure factor

$f(v)$, v: Maxwell-Boltzmann distribution, velocity of gas particle

f', f'' real and imaginary parts of X-ray scattering factor

$\mathbf{G}$: reciprocal lattice vector

$\mathcal{H}$: Hamiltonian

H_α: transition field from helicoid to twisted ferromagnet

H_{c}: transition field from conical to ferromagnetic state

H_{d}: demagnetizing field

H_{k_1}, H_{k_2}: fields indicating knee points in magnetization curves

H_{s}: field at which a shoulder is observed in the susceptibility

H_{Q}: field for transition Q-phase to conical phase

h, k, ℓ: Miller indices

J: Heisenberg exchange constant

$\mathbf{J}$: electrical current density

K: uniaxial anisotropy constant

L, γ: Lorentzian function, its width

L_{D} helical wavelength

M_{sat}, M_{rem} saturation and remanent magnetization

m: mass of gas particle

N: number of atomic layers

N_p, n_p: number of particles, number density of particles

n: refractive index

n_s: volume density of scatterers

$\hat{\mathbf{n}}$, $\hat{\mathbf{m}}$: normal unit vector, magnetization unit vector

p: pressure

Q: magnetic wavevector

$\mathbf{q}$: wavevector

q_c: XRR critical wavevector

R: reflectivity

$\mathbf{R}$, $\mathbf{x}$: direct lattice point, position vector within unit cell

R_0: ordinary Hall constant

r: SQUID coil radius

r_c: correlation between roughness of interfaces in XRD.

r_e: Thomson radius

S: spin

S': base area of slant cylinder

T_N: ordering (Néel) temperature

T_α: transition temperature from helicoid to twisted ferromagnet

T_c: temperature for transition from conical to ferromagnetic state

T_s: temperature at which a shoulder is observed in the susceptibility

T_Q: temperature for transition Q-phase to conical phase

t: time

u_Mn, u_Ge: basis vector parameters for Mn and Ge atoms

V: scattering potential

V_f: film volume

V_RSO: SQUID voltage in RSO mode

w: magnetic free energy density

z_0, ℓ_0: constant and linear offset parameters in V_RSO

β: SQUID gradiometer loop separation

$\Gamma(\mathbf{q}, \mathbf{q}')$: transition rate per unit time for scattering between states $\mathbf{q}, \mathbf{q}'$

ε: EMF

θ', ϕ': polar and azimuthal angle

θ_{c} XRR critical angle

θ: inident angle for X-rays

2θ: angle between incident and specularly scattered X-rays

ϑ: cone angle

κ_0, κ: power law fitting parameters

λ: X-ray wavelength

λ_{MFP}: mean free path of gas atoms

μ: sample dipole moment

ρ: density of electrons

ρ_{xx}, ρ_{yx}: longitudinal and Hall resistivity

ρ_{yx}^{O}, ρ_{yx}^{A}, ρ_{yx}^{T}: ordinary, anomalous and topological Hall resitivity

ρ_e: electron density

ρ_m, σ_m: magnetic surface and volume charge density

σ: cross-sectional area of particles

$\sigma_{\mathrm{L}}, \sigma_{\mathrm{U}}$: roughness of lower and upper interfaces in XRD

σ_{H}: Hall conductivity

Φ: atomic flux

Φ_{B}, Φ_0: magnetic flux, flux quantum

ϕ: electrostatic potential

ϕ_0: helicoid phase offset

φ: azimuthal angle to describe twisted ferromagnetic state

χ_{Si}, χ_{HF}: substrate susceptibility and MnGe high-field susceptibility above saturation

ψ: angle between orthogonal helices in hedgehog lattice and [111]

Ω': solid angle

ω: XRD sample angle

$\Delta\omega$: XRD sample offset

Acknowledgements

There is perhaps no greater contributor to my physics education than my supervisor, Dr. Theodore L. Monchesky. It has been a pleasure to work with Ted for the past five years, and I am lucky to also call him my friend. He has always remained calm and levelheaded throughout my learning, and was always willing to lend a hand and help me improve. His commitment to always give his best for every task has served as a tremendous inspiration to me, and my labmates. I have learned a great deal from Ted, about magnetism, experimental techniques, or unconventional and tasty pizza toppings. Ted, without your support I would never have made it this far.

I would also like to thank my labmates. Dave, you are the glue that holds the lab together and I have many fond memories to look back on. Jason, our "coffee walks" have always been productive and enjoyable, and you have taught me a great deal in the time we have been working together. I have always enjoyed bouncing ideas off each other, and of course we have the shared struggle of maintaining and using the MBE. Cameron, thank you for performing the micromagnetic simulations in this thesis, and for the insightful conversations in the Tim Hortons line. The reader may now understand that the majority of the problems in our group are sorted whilst procuring caffeine. Andrey, thank you for your insightful inputs.

I would like to thank my supervisory committee, Dr. Martin Plumer and Dr. Kevin Hewitt for taking time out of their busy schedules to read and oversee this thesis. I would be remiss if I did not thank the departmental technologists, Andy George, Kevin Borgel, and John Noddin for their help with X-ray measurements, the MBE, and ensuring that we always had liquid nitrogen. Without them, there would be no samples to study in this thesis. I would also like to thank Dr. Graeme Luke and Mathew Pula from McMaster University, for generously allowing us to measure our samples with their SQUID. Without their collaboration, this thesis would be a lot shorter. I also want to recognize Dr. Christy Kinane, Dr. Andrew Caruana and Andy Church at the ISIS Neutron and Muon Source for their hospitality and assistance in PNR measurements, although the data did not make it into this thesis.

As with all research, I stand on the shoulders of giants, and I am particularly indebted to those who came before me. I would like to thank Dr. Eric Karhu, Dr. Samer Kahwaji, Dr. Murray Wilson and Dr. Simon Meynell for their previous work in this lab, and all the problems they solved so we did not have to.

Lastly, none of this would have been possible without the support from my wife, Alex. She has put up with the late nights in the lab, and she has been there for all of the setbacks and successes. I am incredibly lucky to have had her by my side since I first started learning physics in grade 11. This thesis is dedicated to her.

Chapter 1

Introduction

With development in the complexity of electronic computing, there is demand for improvement in data storage technology. The largest technology companies, Amazon, Google, Facebook and Microsoft are estimated to store over 1 billion gigabytes of information between them, and this figure will continue to rise exponentially as technology takes on a larger role in our lives. However, fundamental material limitations have caused a plateau in the improvement of the size and speed of memory devices. In traditional magnetic storage, data is encoded in the magnetic domains of a thin metallic film. The direction of the magnetization (up or down, for example) represents two bits, and the energy cost of writing information is associated with the energy required to flip the magnetization in one domain.

The field of spin-transport electronics, or spintronics, is an emerging field that differs from traditional electronics in that it makes use of both the charge and spin states of the electron to store information. The field began in the 1980's with the discovery of giant magnetoresistance (GMR) [1, 2], for which Albert Fert and Peter Grünberg won the Nobel prize in 2007. GMR was first observed in Fe/Cr multilayers, where a drastic change in the electrical resistance was observed when the spins in adjacent ferromagnetic layers are aligned parallel or anti-parallel to one another. GMR devices where the first generation of spintronic technology, and their incorporation into read/write heads of magnetic hard drives is partially responsible for the swift increase in information storage density over the past few decades.

Another effect in spintronics is spin transfer torque (STT). It was demonstrated if a spin polarized current flows through a ferromagnetic material, it will drag domain walls along with it [3, 4]. One particularly useful application of STT in information storage is that it can induce a magnetization reveral on timescales less than 1 ns [5]. In contrast to the current densities of $10^9\,\mathrm{A\,m^{-2}}$ needed to move ferromagnetic domain walls [6], it was shown that STT can be used to manipulate novel

magnetic textures called skyrmions with less than $10^6\,\mathrm{A\,m^{-2}}$ [7]. These novel textures have been observed in a wide array of materials where inversion symmetry is broken. Storage devices made from these materials, known as racetrack memory [8, 9], have the potential to revolutionize data storage with increased information density, faster read/write times, and lower power consumption. More recently, neuromorphic computer architectures have been proposed to make use of topological magnetic states like skyrmions or hedgehogs [10]. Furthermore, topologically trivial helical phases, the ground state of many skyrmion materials, have been even been proposed for spintronic applications [11, 12, 13].

To create these devices, the magnetic materials must be created and their magnetism must be well understood. This thesis reports on the synthesis and magnetic characterization of the cubic helimagnet MnGe, a material whose magnetic structure is not well understood, is currently under debate.

1.1 MnGe and other cubic helimagnets

MnGe is a cubic helical magnet which belongs to the group of compounds with strukturbericht designation B20 and space group $P2_13$. The crystal lattice can be thought of as a distorted NaCl-type (rock salt) structure with the following basis:

$$(u,u,u)\,;\quad (1/2+u,1/2-u,-u)\,;\quad (-u,1/2+u,1/2-u)\,;\quad (1/2-u,-u,1/2+u)\,.$$

There are four Mn atoms and four Ge atoms in the unit cell, each specified by the basis, with $u_{\mathrm{Mn}} = 0.136$ and $u_{\mathrm{Ge}} = 0.846$ at 200 K [14, 15]. The B20 structure is chiral, meaning it lacks inversion symmetry. The left- and right-handed crystal structures are related by replacing u with $1-u$. Its cubic lattice parameter is $a = 4.79\,\text{Å}$ [14].

The MnGe crystal structure is detailed in Figure 1.1. All crystal visualization in this thesis used the `VESTA` software [16]. The Mn and Ge atoms comprise a helix which winds around the [111] directions according to the chirality of the crystal. The stacking of atoms along [111] can be described in terms of a quadruple layer (QL), which has a thickness corresponding to the (111) plane spacing of 2.77 Å. A QL consists of a dense layer of Mn atoms, followed by a sparse Ge layer, sparse Mn layer and dense Ge layer. The stacking unit along [111] is comprised of twelve layers of atoms, which can be described as ABC stacking of the QL.

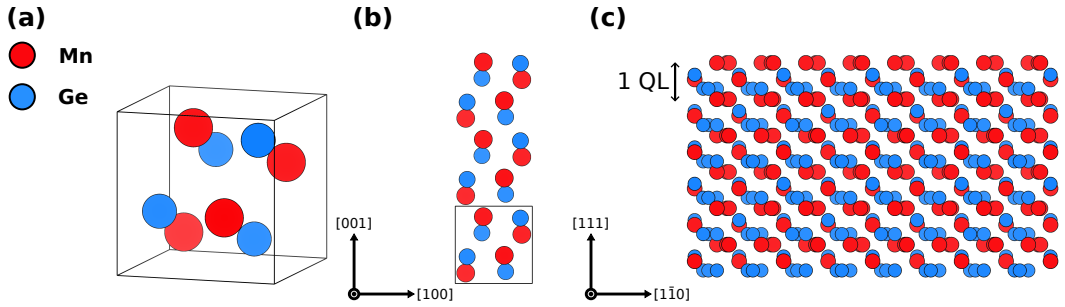

Figure 1.1: Illustration of the B20 crystal structure. (a) The primitive unit cell of MnGe. (b) Several unit cells along the [001] direction to illustrate the chiral crystal structure. (c) Illustration of the QL stacking sequence along [111]. One QL is indicated and consists of two dense and two sparse atomic layers.

A magnetic helical phase is one where the magnetic moments lie in the plane and ferromagnetically align within each layer. The helix is characterized by its propagation wavevector $\mathbf{Q}$ around which successive planes of magnetization rotate. The spatial period over which the magnetization completes one rotation in the plane is the helical pitch (or helical wavelength), given by $L_{\mathrm{D}} = 2\pi/Q$. When a magnetic field is applied perpindicular to the plane of the spins, they cant toward this field, creating a conical phase. Bulk MnGe is a helimagnet with a helical pitch that is much shorter than other B20 compounds. Below the ordering temperature of $T_{\mathrm{N}} = 170\,\mathrm{K}$, the helices align to the [100] orientations with a wavelength which varies from 3.8 nm below 30 K to 5.9 nm, just below T_{N} [15, 17].

Possible magnetic configurations for B20 magnets are given by solutions to the continuum model free energy determined by Bak and Jensen [18]. The minimum model to describe thin film B20 compounds, including a uniaxial anisotropy due epitaxial strain is:

$$w(M) = A(\boldsymbol{\nabla}\hat{\mathbf{m}})^2 + D\,\hat{\mathbf{m}}\cdot(\boldsymbol{\nabla}\times\hat{\mathbf{m}}) - K(\hat{\mathbf{m}}\cdot\hat{\mathbf{n}})^2 - \mu_0\mathbf{H}\cdot\mathbf{M} - \frac{\mu_0}{2}\mathbf{H}_{\mathrm{d}}\cdot\mathbf{M}\,. \quad (1.1)$$

The direction of the magnetization is given by $\hat{\mathbf{m}} = \mathbf{M}/M_{\mathrm{sat}}$ where M_{sat} is the saturation magnetization. The terms in Equation 1.1 represent different energy scales. The first term is the exchange energy, which is of quantum mechanical origin, for which the discrete Hamiltonian can be written as

$$\mathcal{H}_{\mathrm{ex}} = -2J\mathbf{S}_i\cdot\mathbf{S}_j\,, \quad (1.2)$$

which prefers the collinear alignment of neighbouring spins $\mathbf{S}_i$ and $\mathbf{S}_j$. This is typically the dominant energy and its strength is related to exchange constant in the continuum model (also known as the spin wave exchange stiffness), which is written $A = JS^2/a$ for a simple cubic material. [19].

The second term is the due to the Dzyaloshinskii-Moriya interaction (DMI). This interaction favours anti-parallel alignment of neighbouring spins,

$$\mathcal{H}_{\mathrm{DM}} = \mathbf{D}_{ij} \cdot (\mathbf{S}_i \times \mathbf{S}_j)\,, \tag{1.3}$$

and its strength is given by the Dzyaloshinskii vector $\mathbf{D}$. This vector is only nonzero in materials which are non-centrosymmetric, *e.g.* B20 magnets. In some centrosymmetric systems, a net DMI can be induced by breaking of inversion symmetry at interfaces, such as metallic multilayers. The constant D for the continuum case is proportional to the magnitude of $\mathbf{D}_{ij}$.

The third term in Equation 1.1 represents a uniaxial magnetocrystalline anisotropy, with $\hat{\mathbf{n}}$ being a unit vector along the normal of the film. This creates an energetic penalty for the magnetic moments to lie along or perpendicular to $\hat{\mathbf{n}}$. This is dictated by the sign of the anisotropy constant K, which is positive when the spins are favoured to point out of the plane of the film (easy axis), and negative when they are favoured to point in the plane (easy plane). Cubic materials also have additional cubic anisotropies. This includes a cubic magnetocrystalline anisotropy and a cubic exchange anisotropy. In a cubic system, there are many equivalent directions (rather than one for the uniaxial case) owing to the high symmetry of the lattice [19]. In thin film B20 materials, cubic anisotropy is typically ignored since it is small compared to the uniaxial anisotropy.

The final term is the Zeeman interaction, which couples the magnetic moments to an external field $\mathbf{H}$. There is also a contribution from the demagnetizing field, $\mathbf{H}_{\mathrm{d}}$, which arises from the magnetization configuration [19]. This can be calculated by considering the density of fictitious magnetic charges, $\rho_m = \boldsymbol{\nabla} \cdot \mathbf{M}$, as well as magnetic surface charges, $\sigma_m = \mathbf{M} \cdot \hat{\mathbf{n}}$. For magnetic textures in which the moments lie in the plane of the film, but vary along its depth (like a helical state), the contribution to the demagnetizing field is entirely due to surface charges since magnetic volume charge density is identically zero.

The simplest solution to the Bak-Jensen functional in the absence of an external field and anisotropy is a one-dimensional helical modulation of the magnetization, given by

$$\hat{\mathbf{m}} = (\cos Qz,\, \sin Qz,\, 0)\,. \tag{1.4}$$

The helical phase consists of successive planes of ferromagnetically aligned moments, which spiral around the helical wavevector $\mathbf{Q}$. This is pictured in Figure 1.2(a). In Equation 1.4, $\mathbf{Q}$ is represented as $Q\hat{\mathbf{z}}$. The pitch of the helix (helical wavelength) is given by $L_{\mathrm{D}} = 2\pi/Q$. This is related to the exchange and DMI constants by $L_{\mathrm{D}} = 4\pi A/D$.

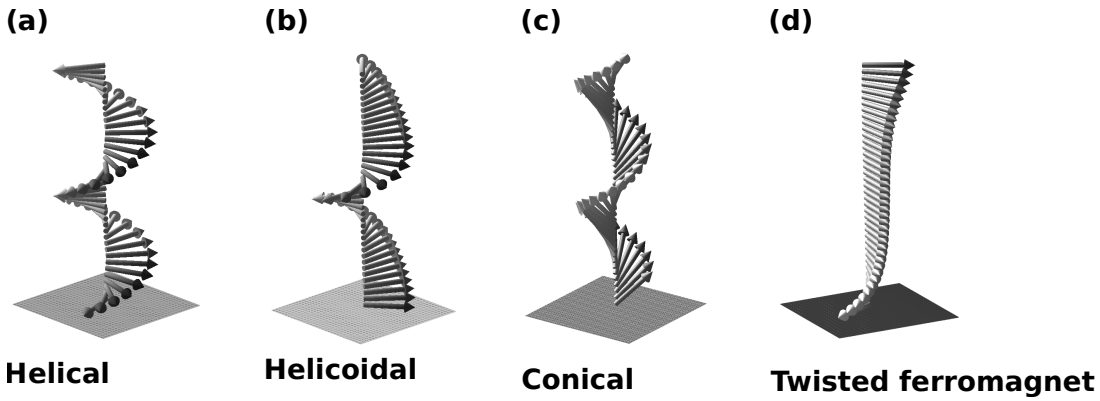

Figure 1.2: One-dimensional magnetic states in B20 thin film magnets. (a) A helical phase described by Equation 1.4. (b) A distorted helix (helicoid) caused by the application of a magnetic field perpindicular to the propagation vector. (c) A cone phase, caused by the application of a magnetic field parallel to the helical propagation vector. (d) A twisted ferromagnetic state comprised of uniform magnetization at the centre of the film, with surface twists near the interfaces.

When a field is applied to the helical state along $\mathbf{Q}$, the spins will cant out of the plane to align with the field. This gives a conical modulation,

$$\hat{\mathbf{m}} = (\cos Qz \cos\vartheta,\, \sin Qz \cos\vartheta,\, \sin\vartheta)\,. \tag{1.5}$$

The cone angle is ϑ, the angle between $\mathbf{Q}$ and the spins. It does not vary spatially. The cone phase will continuously deform from into a field-induced ferromagnetic phase with increasing field. This is a second-order transition and corresponds to the cone angle varying continuously from $\vartheta = 0$ to $\vartheta = \pi/2$ with increasing field. Substituting

Equation 1.5 into Equation 1.1 and minimizing for ϑ gives

$$\vartheta = \arcsin\left(\frac{2\mu_0 H A M_{\mathrm{sat}}}{D^2}\right), \tag{1.6}$$

where and the critical field for the ferromagnetic transition is $\mu_0 H_{\mathrm{c}} = D^2/2AM_{\mathrm{sat}}$.

In bulk crystals, the application of a field perpindicular to $\mathbf{Q}$ will cause a reorientation of $\mathbf{Q}$ to the direction of the applied field. For the case of a thin film, addition of an easy plane anisotropy stabilizies state with the moments in-plane and the field does not reorient the helix. Instead the helical state is distorted into a helicoid. The solution to the magnetization is given in terms of elliptic integrals, which for small fields which can be approximated by a Fourier expansion. [20]. The depth profile $M(z)$ of a helicoid is modulated by higher-order sinusoids. The magnetization of a distorted helicoid can be modelled by [20, 21, 22]:

$$M(z) = M_0 + M_1 \sin(Qz + \phi_0) + M_2 \cos^2(Qz + \phi_0), \tag{1.7}$$

where $M_0 = M_2 = 0$ corresponds to the pure helical state and ϕ_0 is a phase offset. In Reference [23], it was demonstrated for MnSi thin films using polarized neutron reflectometry (PNR) and micromagnetic simulations that field-induced unwinding of the helicoids occured in discrete steps. Finite size effects confine the wavelength and lead to a quantization of the number of turns in the helicoid. It was shown for a film with thickness 1.92 L_{D} that the ground state was a helix with two turns. This was deformed into a single-turn helicoid, and then into a twisted ferromagnetic state. Instead of fully saturating at high fields, the sample enters a twisted ferromagnetic state where the majority of the helical modulation is suppressed, except for small twists which exist at the surfaces, stabilized by the DMI [23, 24]. The analytic form is derived for the twisted ferromagnetic state in Reference [24]. Similar to Equation 1.4, the magnetization is $\hat{\mathbf{m}} = (\cos\varphi(z), \sin\varphi(z), 0)$ where the azimuthal angle of the magnetization is given by

$$\varphi(z) = 4\arctan\left[\left(2\sqrt{H/H_{\mathrm{c}}} - \sqrt{4H/H_{\mathrm{c}} - 1}\right)\exp\left(-Qz\sqrt{H/H_{\mathrm{c}}}\right)\right]. \tag{1.8}$$

The twisted ferromagnetic state is represented in Figure 1.2(d). The magnetization is almost completely uniform at the centre of the film, with the twisting occuring near the surfaces.

It is also possible to observe magnetic states which are characterized by multiple wavevectors. Two relevant multi-Q states to this thesis are the skyrmion and spin-hedgehog lattices. Magnetic skyrmions were first proposed by Bogdanov and Yablonskii in 1989 [25], predicted to exist in cubic helimagnets by Rößler *et al.* in 2006 [26], and observed in bulk MnSi by Mühlbauer *et al.* in 2009 [27]. Skyrmions are topologically nontrivial solitons which consist of region of twisting around an energy costly core in a ferromagnetic background. The DMI and exchange alone are not sufficient to stabilize skyrmions. Additional interactions, such as magnetocrystalline anisotropy [25, 28] or spin-fluctuations [27] are required to favour skyrmions over competing one-dimensional modulations. Finite size effects also contribute to determining the spin structure [29, 30, 31]. Though inherently nonlinear, a crude ansatz for a skyrmion lattice can be constructed as a superposition of coplanar helices, propagating perpendicular to the applied field. They are effectively two-dimensional modulations and exhibit a cylindrical-like symmetry.

The term spin-hedgehog lattice is used to explain the three-dimensional skyrmion lattice structures reported in bulk MnGe [32, 33]. It can be described by the superposition of three orthogonal helices leading to a crystal of emergent magnetic monopoles (hedgehogs) and anti-monopoles (anti-hedgehogs). The magnetization profile of the cubic spin-hedgehog lattice state is given in Reference [34] as:

$$\mathbf{M}(\mathbf{r}) = \sum_{i=1,2,3} \mathbf{a}_i \cos \mathbf{q}_i \cdot \mathbf{r} + \mathbf{b}_i \sin \mathbf{q}_i \cdot \mathbf{r}\,, \tag{1.9}$$

where:

$$\begin{aligned}
&\mathbf{q}_1 = (\sin\psi,\, 0,\, \cos\psi),\\
&\mathbf{q}_2 = (-\tfrac{1}{2}\sin\psi,\, \tfrac{\sqrt{3}}{2}\sin\psi,\, \cos\psi),\\
&\mathbf{q}_3 = (-\tfrac{1}{2}\sin\psi,\, -\tfrac{\sqrt{3}}{2}\sin\psi,\, \cos\psi),\\
&\mathbf{a}_1 = (\cos\psi,\, 0,\, -\sin\psi),\\
&\mathbf{a}_2 = (-\tfrac{1}{2}\cos\psi,\, \tfrac{\sqrt{3}}{2}\cos\psi,\, -\sin\psi),\\
&\mathbf{a}_3 = (-\tfrac{1}{2}\cos\psi,\, -\tfrac{\sqrt{3}}{2}\cos\psi,\, -\sin\psi),\\
&\mathbf{b}_1 = (0,\, 1,\, 0),\\
&\mathbf{b}_2 = (-\tfrac{\sqrt{3}}{2},\, -\tfrac{1}{2},\, 0),\\
&\mathbf{b}_3 = (\tfrac{\sqrt{3}}{2},\, -\tfrac{1}{2},\, 0).
\end{aligned}$$

In this prescription, ψ is the angle between the three helices and the $\langle 111 \rangle$ direction. In bulk MnGe, the helices propagate along the $\langle 100 \rangle$ directions, so $\psi = \arccos\left(1/\sqrt{3}\right) \approx 54.7°$. When ψ decreases, the helices are tilted toward the film normal. In this sense, ψ is related to the strength of the uniaxial anisotropy. When $\psi = 0$, Equation 1.9 simply describes a single helix with $\mathbf{Q}$ along [111].

A representation of the cubic spin-hedgehog lattice is given in Figure 1.9. The z-component of the magnetization (coloured red and blue in the figure for positive and negative, respectively) varies periodically in the z-direction. The hedgehogs are singular regions where the magnetization reverses sign (meeting of blue and red regions). The local field at these points behaves as an emergent magnetic monopole or anti-monopole.

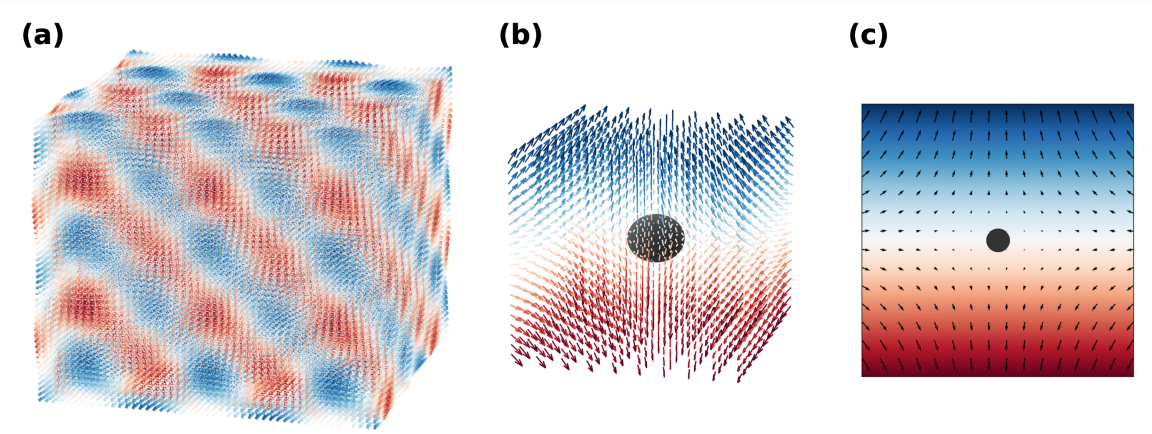

Figure 1.3: (a) Representation of the cubic spin-hedgehog lattice in MnGe. The spin is coloured blue (red) if its z-component is positive (negative). The lattice is comprised of chains of alternating hedgehogs and anti-hedgehogs. In this representation, the vertical direction is [111] and the three superposed helices lie along $\langle 100 \rangle$. (b) A representation of one hedgehog. The dark sphere shows the location of the Bloch point. (c) Two-dimensional slice of the hedgehog in (b). The colour again represents the z-component of the spins. The magnetization around the Bloch point behaves similarly to a gradient field near a saddle point. The configuration of an anti-hedgehog is such that it will produce zero net magnetization when superposed with the hedgehog.

1.2 Bulk and thin film MnGe

The equilibrium phase diagram of the binary Mn-Ge system does not include the B20 phase; it is a metastable phase [35]. Bulk MnGe powder was first synthesized in 1988

at 1000 °C and high pressures exceeding 4 GPa [14]. Upon further annealing at 600 °C and ambient pressure, it was found to decompose into the orthorhombic ferromagnet $Mn_{11}Ge_8$ and Ge. Reference [14] claims that MnGe is antiferromagnetic with a Néel temperature of 197 K. It is now known that MnGe is not antiferromagnetic, but a short-period helimagnet. Further measurements of the magnetism in MnGe were not reported until after the discovery of skyrmions in MnSi led to a drastic increase in the number of published papers studying B20 compounds.

A large majority of the literature surrounding B20 MnGe has been published by the group from RIKEN. Kanazawa *et al.* synthesized polycrystalline MnGe in 2011 and performed small-angle neutron scattering (SANS), observing an incommensurate helical structure with a pitch that elongates from 3 nm at 20 K to 6 nm just below the ordering temperature T_N of 170 K [17]. They also performed electrical resistivity measurements and inferred a large topological Hall effect from the residual of fitting the ordinary and anomalous Hall effects. The temperature dependence of the helical wavelength was confirmed by Makarova *et al.* using neutron diffraction and the magnetic moment was measured to be 2.3 μ_B per Mn atom at 2 K [15]. Refinement of neutron diffraction patterns reported several acceptable magnetic configurations, including single-Q and triple-Q structures [36]. The existence of a triple-Q phase was claimed to be supported by the existence of a topological Hall effect.

Further SANS measurements by the RIKEN group observed a peak with wavevector perpindicular to the direction of an applied field, which was attributed to a multi-Q ground state [37]. Based on their interpretation of the extracted topological Hall resistivity, they argued that the cubic spin-hedgehog lattice was the most likely candidate for the ground state, at zero and finite field.

Supporting evidence for this texture was obtained from Lorentz transmission electron microscopy (LTEM) in Reference [32]. Grains of the [001] orientation were extracted from a polycrystalline sample by focused ion beam. Stripe contrasts were observed along the [100] and [010] directions which disappeared above T_N and were attributed to the magnetic structure. At 30 K under an applied field of 2.4 T, densely-packed spin spirals similar to those in Figure 1.3(a) were reported which has been used (along with their extracted topological Hall effect) to confirm the presence of the spin-hedgehog crystal [38, 39].

There is controversy surrounding the presence of the spin-hedgehog state in MnGe. The controversy arises from the difficulty in distinguishing the triple-Q state from a multidomain single-Q helical state using SANS. Several studies have proposed a multidomain helical state [40, 41, 42, 43, 44] in MnGe, rather than the hedgehog lattice. Analysis in Reference [42] of muon spin rotation data from 10 K in Reference [45] was consistent with helimagnetic order. This probe of the local structure is in disagreement with the LTEM images in Reference [32].

In 2015, Viennios *et al.* reported a phase diagram of bulk MnGe based on magnetometry measurements [46]. They find helical, conical, and ferromagnetic phases as expected by Equation 1.1 for a B20 magnet. They also report a pocket which they label as the A phase that is in an analagous to the skyrmion phase pocket in the MnSi phase diagram (near the ordering temperature, at finite fields). Their identification of a helical phase at low temperatures and fields does not explain the topological Hall effect measured by other groups. They also identify a second phase, the B phase, but its origin is unknown. This paper suggests that the magnetism in MnGe is more similar to other B20 materials, in contrast to those who claim its ground state is the topological spin-hedgehog crystal and do not report an A phase pocket near the ordering temperature.

Thin film MnGe was first grown using MBE on Si(111) substrates in 2013 [47]. To help nucleate the B20 phase, a template layer of MnSi was crystallized before deposition of Mn and Ge. This produced single-orientation MnGe, although there is evidence for secondary phases in the reported X-ray data. The films also appear to have a high roughness based on the lack of Kiessig fringes. Reference [47] only reported minimal information on the magnetic properties of their MnGe films, and found the signal to be dominated by the 2 nm MnSi seed layer below its ordering temperature of approximately 40 K. The group from RIKEN also used a 2 nm MnSi template to produce MnGe films with thicknesses 160 nm, 735 nm and 1.8 µm [34]. They used SANS to show that in the thick film ($\approx$ bulk), the Q vectors pointed along $\langle 100 \rangle$. With decreasing film thickness and increasing uniaxial anisotropy, they found that the Q vectors canted toward the film normal (described by ψ in Equation 1.9). At 2 K and zero field, the 160 nm film is in a triple-Q state. At 100 K, there is a reorientation of the helical wavevectors to the direction of the film normal ($\psi = 0$)

and the magnetization is an out-of-plane helix. Whether the low-temperature state is a hedgehog lattice or comprised of multiple helicoidal domains, SANS suggests that helical and conical states exist above 100 K for zero and finite fields, respectively. Both References [34, 47] report an enhancement in the ordering temperature from $T_N = 170$ K in bulk to approximately 200 K in films with thicknesses ranging from 4.5 nm to 160 nm. More recently, the group from RIKEN have used thin films to study the large anomalous and topological Hall signals [48, 49] in MnGe.

Spin-polarized scanning tunneling microscopy (SP-STM) was used by Repicky *et al.* to measure the real-space magnetic textures on the (111) surface of MnGe. Their 80 nm thick film was grown with MBE using a buffer layer of FeGe. At 5 K (within the triple-Q region in Reference [34]), stripe domains were observed, consistent with a helix. The periodicity was measured to be 6 nm, much longer than the 3 nm reported by others below 30 K. Interestingly, multiple helical domains were imaged. At some regions, three *distinct* orthogonal helices were observed. This configuration would manifest as a triple-Q state in a SANS experiment. Furthermore, topological defects were imaged, formed by the intersection of these stripe domains. These results support the presence of a multidomain helioid state, rather than the hedgehog lattice. The presence of disclinations would contribute to a topological Hall anomaly, but the density of these defects observed in the SP-STM data likely cannot explain the size of the Hall signal.

A wide range of theoretical works have calculated D [50, 51, 52, 53, 54] and A [53] for MnGe or $Mn_{1-x}Fe_xGe$, but the values they obtain are not consistent. The consensus is that the DMI alone is too weak to stabilize the tight pitch of the magnetic structure. A comprehensive theory on why this is the case has yet to emerge. More work has gone into calculating the viability of the spin-hedgehog phase. One poposal by Grytsiuk *et al.* is a novel topological chiral interaction which does not exist in other B20 compounds, which favours non-collinear spin structures [55]. Another study claimed that the consideration of weak higher-order exchange interactions would stabilize the hedgehog lattice over the helical state [56].

Recent numerical work by Rudderham *et al.* modelled the effect of uniaxial anisotropy and finite-size effects on the formation of skyrmions in B20 thin films [31]. It was found that the stability of in-plane skyrmion lattices and/or in-plane helicoids

was strongly dependent on film thickness for small values of anisotropy. This is an interesting avenue for an experimental study in which the film thickness can be tailored in search of skyrmion lattices with a specified number of layers, or helicoids with a certain number of twists. The disappearance and reemergence of skyrmion states as a function of film thickness can also be used to estimate the strength of the anisotropy in the film.

1.3 Scope of this thesis

To date, all MnGe thin films have been grown using a $\sim 2\,\text{nm}$ template of the magnetic B20's MnSi or FeGe. This makes the measurement of the magnetic properties of MnGe thin films difficult, since the observed signal will also contain the contribution from the template. This exacerbated by the tight helical pitch which means that the study of confinement effects predicted by Rudderham *et al.* occurs for thicknesses in the range of 3 nm to 30 nm. Perhaps due to the necessity of a B20 seed layer (deposition of Mn and Ge on Si(111) result in $P6_3/mcm$ Mn_5Ge_3, shown in Figure 1.4), for which magnetic compounds (MnSi, FeGe) are the most easily reproduced, there have been no comprehensive reports on the magnetic properties for MnGe films with thicknesses below 80 nm.

The aim of this thesis is to study MnGe thin films of thickness less than 40 nm, a range where a magnetic template layer is not appropriate. A non-magnetic template layer is used and represents the first growth of magnetically isolated MnGe thin films.

One may question the need for a non-magnetic template, if the properties of the template can be measured and subtracted. The danger in such an approach for MnGe is illustrated in Reference [22], which studied the impact of a ferromagnetic Fe pinning layer below the FeGe helix using PNR. Isolated FeGe is subject to symmetric boundary conditions at the top and bottom interfaces, resulting in a modulation which was symmetric about the centre of the film. A Fe pinning layer breaks this symmetry and leading to the exchange coupling of the spins at the bottom of the helix. The helix was then able to be manipulated by this Fe layer. It is quite possible that the properties of MnGe may be influenced by an underlying magnetic template layer. Given that the magnetic structure of MnGe is not precisely known, the effect of this interaction is impossible to disentangle. Furthermore, the triple-Q region observed in

the 160 nm film by the RIKEN group occurs exclusively below 50 K, approximately the same window in which the MnSi template layer is magnetic (below $\sim$ 40 K). Understanding the origin of this phase necessitates the decoupling of the magnetism of MnGe and MnSi.

The isostructural B20 compound CrSi was chosen to act as a template layer for the growth of MnGe since it is known to be paramagnetic down to low temperature [57, 58]. Reference [59] reports an extremely weak ferromagnetic moment less than 0.04 μ_B per Cr atom below low 20 K but it is difficult to rule out the presence of impurities in their sample based on the available data. In addition to the trivial magnetic behaviour of CrSi, the possible side products Cr and CrGe are also paramagnetic. This provides an advantage to CrSi over FeSi (also paramagnetic), for example, which may produce ferromagnetic Fe or FeGe as magnetic impurities.

The nucleation of CrSi was on Si substrates was investigated by Wetzel *et al.* where Cr overlayers were deposited and subsequently annealed. [60, 61] It was found that epitaxial B20 CrSi formed below 400 °C, and above this temperature, hexagonal $CrSi_2$ (space group $P6_222$) formed. This was evidenced by low energy electron diffraction (LEED) and X-ray photoelectron spectroscopy (XPS). The crystal structure of $CrSi_2$ is shown in Figure 1.4.

Investigations into the nucleation of MnSi on Si(111) were performed by Higashi *et al.* using STM. It was found that the B20 structure forms when Mn overlayers react with the underlying substrate. If the Mn layer is too thick, the Si will leave behind caves in the substrate which leads to a rough film. A similar behaviour was also observed in Reference [62]. Higashi *et al.* found that the resultant film quality would be drastically improved by depositing a stack which already contained the necessary Si to form MnSi. When a stack consisting of 0.5 QL Si / 1 QL Mn / 0.5 QL Si was deposited, the resulting 2 QL layer of MnSi was atomically flat. A small number of holes were observed, but nearly the entire surface (98%) was covered. This recipe was applied in this thesis to yield a 2 QL template of CrSi.

The scope of this thesis is twofold. Firstly, this work aims to synthesize B20 MnGe films of thickness below 40 nm using a non-magnetic template layer. This will fill a gap in the present literature. Secondly, this thesis aims to investigate the magnetic properties of these films. The goal is to understand the influence of finite size effects

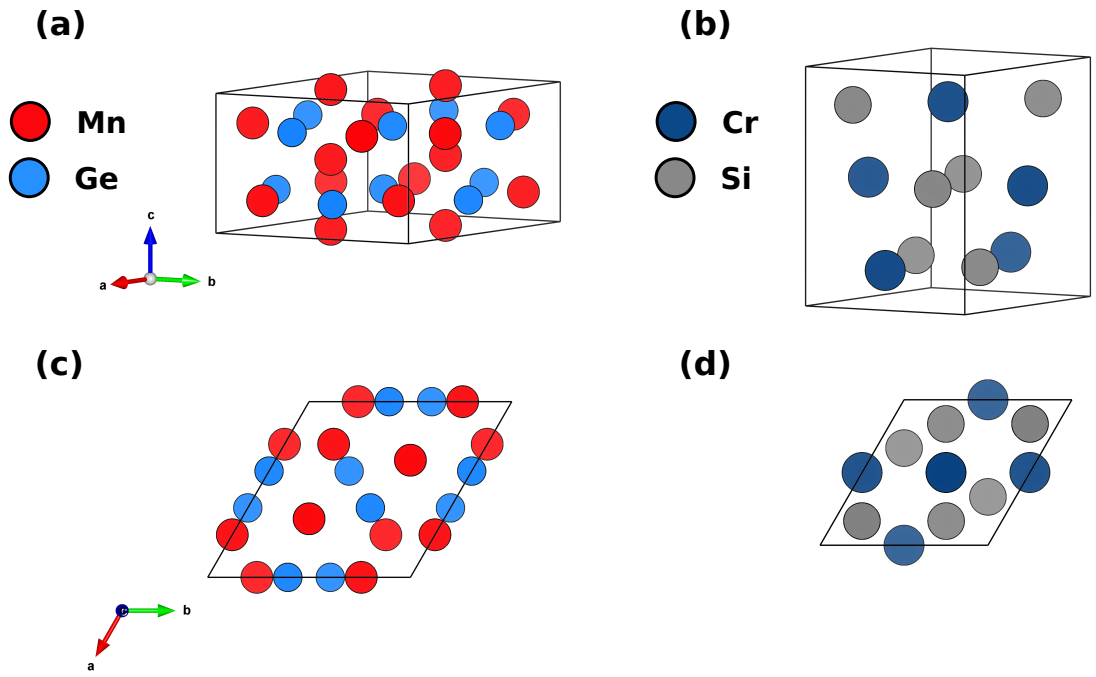

Figure 1.4: (a) and (c) Crystal structure of hexagonal Mn_5Ge_3. (b) and (d) Crystal structure of hexagonal $CrSi_2$.

on MnGe, a system where the helical wavelength is substantially smaller than the other B20 compounds.

Chapter 2

Experimental techniques

This chapter presents an overview of the experimental techniques used in this thesis. The method used to grow the samples is introduced, as well as various diffraction and reflectometry techniques used to characterize their structure. Finally, the techniques used for magnetic characterization of the sampes are discussed.

2.1 Molecular beam epitaxy

The MnGe films studied in this thesis were grown using molecular beam epitaxy (MBE). The term *epitaxy*, from the Greek words *epi* (upon) and *taxis* (arrangement) refers to the growth of a crystalline overlayer, which shares a well-defined orientation with respect to the substrate crystal. During growth, the precursor elements are deposited on the substrate at a rate sufficiciently low (typically $1\,\text{Å}\,\text{min}^{-1}$ to $100\,\text{Å}\,\text{min}^{-1}$) so as to allow the film to grow one atomic layer at a time, so long as the film and substrate are lattice matched. There are three main modes of film growth, dictated by the interaction between the precusror atoms and substrate, and the precursor self-interaction [63]. If the precursor atoms are more attracted to the substrate than themselves, they will tend to wet the substrate and the film can grow layer-by layer. This is Frank-Van der Merve growth. In the other extreme, Volmer-Weber growth, the precusror atoms are strongly attracted to themselves which leads to the nucleation of islands which only coalesce for large film thicknesses. The intermediate case consists of a smooth wetting layer upon which islands nucleate above some critical thickness, known as Stranski-Krastanow growth. Each of these growth modes are depicted in Figure 2.1.

Film growth by MBE occurs in an ultra high vacuum (UHV) environment, in order to minimize time interval over which contaminant species will impinge on the surface of the sample. To estimate the maximum allowable pressure for MBE growth, consider a flux $\Phi = \mathrm{d}N_\mathrm{p} \,/\, \mathrm{d}S'\,\mathrm{d}t$ consisting of $\mathrm{d}N_\mathrm{p}$ contaminant particles adsorbing on

a sample area $\mathrm{d}S'$ in time $\mathrm{d}t$. The particles which contribute to the flux have velocity v and will be within a distance $v\,\mathrm{d}t$ of the surface, and come from a particular direction within solid angle $\mathrm{d}\Omega'$. It is useful to consider an infinitesimal volume which forms a slant cylinder with base area $\mathrm{d}S'$ and height $v\,\mathrm{d}t\cos\theta'$, and integrate $\mathrm{d}\Omega'$ over all of these cylinders. The number of particles in this volume depends on their volume density n_p, and the probability of one particle having velocity between v and $v+\mathrm{d}v$ is given by the Maxwell-Boltzmann distribution, $f(v)$. This means that the total number of particles within one slant cylinder with velocity v is given by:

$$\mathrm{d}N_\mathrm{p} = n_\mathrm{p}\,\mathrm{d}V\,f(v)\,\mathrm{d}v\,\frac{\mathrm{d}\Omega'}{4\pi} = n_\mathrm{p}\,\mathrm{d}S'\,v\cos\theta'\,\mathrm{d}t\,f(v)\,\mathrm{d}v\,\frac{\sin\theta'\,\mathrm{d}\theta'\,\mathrm{d}\phi'}{4\pi}\,. \tag{2.1}$$

Integrating over all velocities and restricting the solid angle to account for contamination which comes from above the sample, one obtains

$$\Phi = \int\frac{\mathrm{d}N_\mathrm{p}}{\mathrm{d}S'\,\mathrm{d}t} = n_\mathrm{p}\int_0^\infty \mathrm{d}v\,vf(v)\frac{1}{4\pi}\int_0^{\pi/2}\mathrm{d}\theta'\sin\theta'\cos\theta'\int_0^{2\pi}\mathrm{d}\phi' = \frac{1}{4}n_\mathrm{p}\left\langle v\right\rangle\,, \tag{2.2}$$

where $\langle v\rangle = (8k_\mathrm{B}T/\pi m)^{1/2}$ is the thermal velocity of the particles, with mass m at temperature T. Substituting the equation of state for an ideal gas, one obtains an estimate of the pressure:

$$p = \Phi\sqrt{2\pi m k_B T}\,. \tag{2.3}$$

Consider CO, one of the most common contaminant species inside an MBE chamber, which has mass of $4.65\times10^{-27}\,\mathrm{kg}$ and surface density of $2.33\times10^{19}\,\mathrm{m}^{-2}$. Constraining the monolayer arrival time to be longer than 1 hour (the timescale of MBE film deposition), the criterion is obtained: $p < 4.00\times10^{-8}\,\mathrm{Pa}$ at $298\,\mathrm{K}$.

It is illustrative to estimate the mean free path of the gas molecules inside an MBE chamber. This is simply the ratio of the distance travelled and the number of collisions in time interval $\mathrm{d}t$. The distance travelled by one particle in $\mathrm{d}t$ is simply $\langle v\rangle\,\mathrm{d}t$. If the cross-sectional area of the particles is σ, the effective volume of the interaction can be written in terms of their relative velocity as $\sigma\left\langle v_\mathrm{rel}\right\rangle\mathrm{d}t$. The square of their relative velocity is given by $\langle(\mathbf{v}_1-\mathbf{v}_2)^2\rangle = \langle 2v^2 - \mathbf{v}_1\cdot\mathbf{v}_2\rangle$. If these particles are in equilibrium, their velocities are uncorrelated and $\mathbf{v}_1\cdot\mathbf{v}_2 = 0$, meaning the relative velocity is $\left\langle v_\mathrm{rel}\right\rangle = \sqrt{2}\left\langle v\right\rangle$. Knowing the interaction volume and the density of particles, one obtains an estimate for the mean free path:

$$\lambda_\mathrm{MFP} = \frac{1}{\sqrt{2}\sigma n_\mathrm{p}} = \frac{k_\mathrm{B}T}{\sqrt{2}\sigma p}\,. \tag{2.4}$$

The particles may be approximated as spherical by using $\sigma = \pi d_{\mathrm{k}}^2$ where d_{k} is the kinetic diameter ($d_{\mathrm{k}} = 376\,\mathrm{pm}$ for CO) [64]. At $4.00 \times 10^{-8}\,\mathrm{Pa}$ and $298\,\mathrm{K}$, the mean free path is $\lambda_{\mathrm{MFP}} = 232\,\mathrm{km}$, much larger than the size of the MBE chamber. It can safely assumed that all particles travel undisturbed in ballistic trajectories.

A schematic of the MBE chamber used to grow the films studied in this thesis is shown in Figure 2.1. The base pressure is less than $8 \times 10^{-9}\,\mathrm{Pa}$ and remains below $3 \times 10^{-8}\,\mathrm{Pa}$ during growth with the use of a liquid nitrogen cryoshroud. The substrate wafers are placed in a sample holder and inserted into the sample manipulator for the growth. The manipulator allows for azimuthal rotation of the substrate to ensure uniform flux from the molecular beams, and includes a heater capable of reaching temperatures in excess of $1000\,^{\circ}\mathrm{C}$. Cr and Mn are deposited using thermal effusion cells, while Si and Ge evaporated by electron beam bombardment. The substrate is obsured from molecular beams by shutters while the desired deposition rate is achieved. The deposition rates of Si, Cr and Ge are measured using quartz crystal oscillator and the Mn rate is found using a calibrated ionization gauge. The Mn flux is determined by recording the pressure difference between gauges inside and outside the beam of Mn atoms. During Mn deposition, the typical differential pressure is $5 \times 10^{-6}\,\mathrm{Pa}$. An electron gun and fluorescence screen allow *in-situ* surface characterization, discussed in Section 2.2.2.

2.2 Diffraction

2.2.1 X-ray diffraction

X-ray diffraction (XRD) is a workhorse technique for *ex-situ* characterization of the structure of the MnGe films. X-rays are scattered from the electronic distribution in the material which reveals information about the film structure and quality. Consider an X-ray (which will described as a plane wave) of wavevector $\mathbf{q}$ incident on a particular material, which scatters into wavevector $\mathbf{q}'$. Fermi's golden rule describes the transition rate $\Gamma(\mathbf{q}, \mathbf{q}')$ per unit time for scattering between states $\mathbf{q}$ and $\mathbf{q}'$ [65]:

$$\Gamma(\mathbf{q}, \mathbf{q}') = \frac{2\pi}{\hbar} |\langle \mathbf{q}| \, V \, |\mathbf{q}'\rangle|^2 \delta(E_{\mathbf{q}'} - E_{\mathbf{q}}) \,, \tag{2.5}$$

where the Dirac delta function ensures conservation of energy, and the matrix element is proportional the Fourier transform of the scattering potential V. A periodic

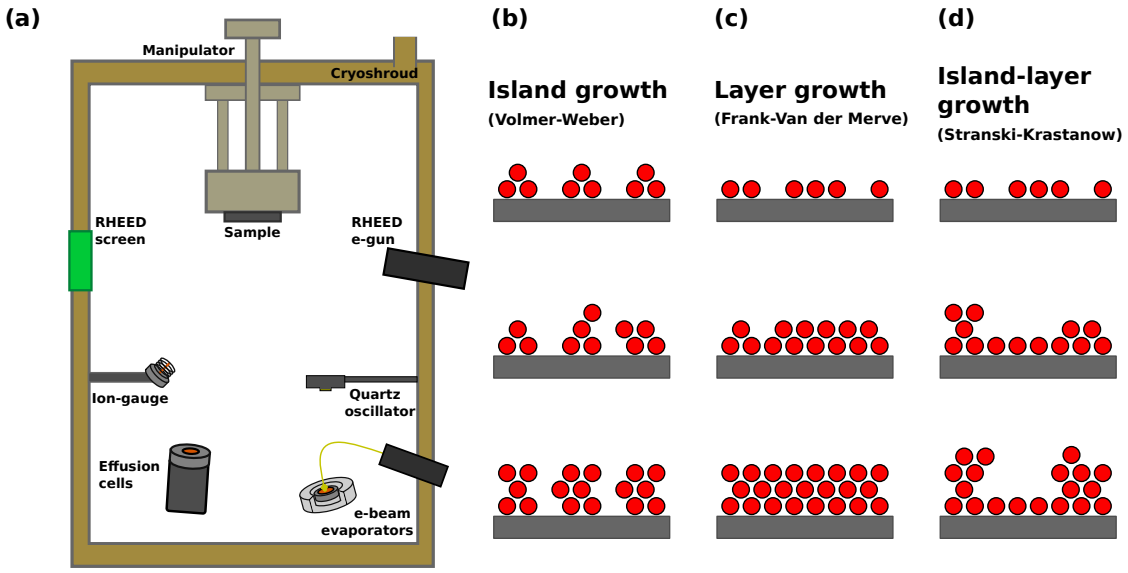

Figure 2.1: (a) Schematic of the MBE chamber used to grow the films studied in this thesis. Precursor atoms are evaporated via effusion cell or electron-beam bombardment. Depositition rates are determined with a quartz oscillator or calibrated ion gauge. The sample sits face-down in the manipulator. (b)-(d) Representation of the three main modes of film growth. Growth time increases as each cartoon is viewed top-to-bottom.

scattering potential yields $V(\mathbf{R}+\mathbf{x}) = V(\mathbf{x})$, where $\mathbf{R}$ is a lattice vector and $\mathbf{x}$ resides within the unit cell. This means that the matrix element in Equation 2.5 becomes:

$$\langle \mathbf{q} | \, V \, | \mathbf{q}' \rangle = \sum_{\mathbf{R}} \exp\left(-i(\mathbf{q}' - \mathbf{q}) \cdot \mathbf{R}\right) \iiint_{\text{unit cell}} \mathrm{d}^3\mathbf{x} \, V(\mathbf{x}) \exp\left(-i(\mathbf{q}' - \mathbf{q}) \cdot \mathbf{x}\right). \qquad (2.6)$$

The definition of the reciprocal lattice ensures that the first term in Equation 2.6 is identically zero unless $\mathbf{q}' - \mathbf{q}$ is equal to a reciprocal lattice vector $\mathbf{G}$. This yields the Laue condition,

$$\mathbf{q}' - \mathbf{q} = \mathbf{G}\,, \qquad (2.7)$$

which ensures conservation of crystal momentum. This concept is easily demonstrated with the Ewald sphere construction in Figure 2.2. A sphere of radius q is drawn with the tip of the incident wavevector $\mathbf{q}$ placed at the origin. Only scattered wavevectors $\mathbf{q}'$ which lie on the sphere satisfy conservation of energy. At points on the Ewald sphere where $\mathbf{q}'$ touches a reciprocal lattice point, crystal momentum is conserved and the scattering vector $q' - q$ is equal to a reciprocal lattice vector. Rotating the

sphere about the origin of reciprocal space (which is equivalent to rotating the crystal or X-ray source) will reveal all allowable reflections from the crystal; they are planes corresponding to reciprocal lattice vectors that touch the surface of the sphere.

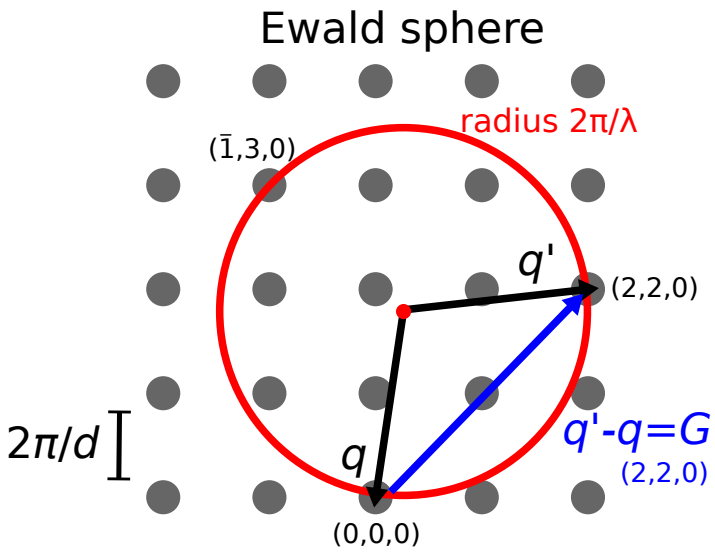

Figure 2.2: Ewald sphere construction for X-ray diffraction. A representative reciprocal lattice is shown as grey dots. The wavevectors $\mathbf{q} = (0, 0, 0)$ and $\mathbf{q}' = (2, 2, 0)$ are noted. The scattering vector $\mathbf{q}' - \mathbf{q}$ is equal to a reciprocal lattice vector $\mathbf{G} = (2, 2, 0)$ and in this geometry, Bragg diffraction occurs for the (220) planes. Another valid Bragg reflection in this geometry is from the $(\bar{1}30)$ planes.

Squaring both sides of Equation 2.7 gives $q^2 = {q'}^2 - 2\mathbf{q}' \cdot \mathbf{G} + G^2$. Considering elastic scattering ($q' = q$) and substituting $q = 2\pi/\lambda$ and $G = 2\pi n/d_{h,k,\ell}$, Bragg's law is obtained:

$$2d_{h,k,\ell} \sin\theta = n\lambda\,, \tag{2.8}$$

where λ is the X-ray wavelength, $d_{h,k,\ell}$ is the spacing between successive scattering planes and θ is the scattering angle. The geometry of Bragg's law is shown in Figure 2.3.

The X-rays are incident on the sample at an angle ω, and the angle between incident X-rays and X-rays scattered into the detector is 2θ. When the sample angle ω is fixed to be equal to θ, it is referred to as a θ–2θ measurement, where the scattering vector remains parallel to the film normal. An XRD experiment is performed by varying the scattering angle θ and monitoring the intensity of scattered X-rays at a

detector angle 2θ with respect to the X-ray source. Peaks in a graph of intensity versus 2θ identify plane spacings given by Equation 2.8.

XRD measurements were performed on a Siemens D500 diffractometer, depicted in Figure 2.3. A source of nearly-monochromatic Cu Kα X-rays irradiates the sample and is collimated with various slits. In the figure, S_1 and S_2 collimate the incident beam. S_3 is an anti-scatter slit. S_4 and S_5 are monochromator slits and M is the monochromator. The slits yield an angular resolution of 0.02°. This is the minimum value of the full width at half maximum (FWHM) in ω that is observable due to instrumental broadening. X-rays are produced from high-voltage electrons striking a Cu anode. When the electrons that have been excited to the 2p orbital decay to the 1s, Kα radiation is produced. The spin-orbit splitting of the 2p orbital into the $2p_{1/2}$ and $2p_{3/2}$ orbitals yields a doublet emission of Cu Kα_1 = 1.540 562 Å, and Cu Kα_2 = 1.544 398 Å, where intensity ratio of Cu Kα_1 to Cu Kα_2 is approximately 2:1.

For each measurement, the sample was aligned to the Si subtrate by setting $2\theta = 28.44°$ (corresponding to the Si(111) peak) and scanning ω while 2θ remains fixed. In this measurement the scattering vector remains fixed in magnitude, while it scans in a direction perpendicular to the film normal. This is known as a rocking curve scan, which yields a peak in intensity as a function of ω. The difference between the ω of maximum intensity and $2\theta/2$ is the offset which is applied to the sample for the duration of the X-ray scan. A rocking curve is used to align the sample before a $\theta - 2\theta$ measurement to ensure that the crystallographic planes of interest are normal to the scattering vector. By scanning both ω and 2θ, a reciprocal space map can be constructed. This is a two-dimensional representation of reciprocal space; while a $\theta - 2\theta$ measurement scans q_z, a reciprocal space map measures XRD in the $q_z - q_x$ plane. The relationship between instrument angles and reciprocal space vectors is

$$q_x = \frac{2\pi}{\lambda}(\cos\omega - \cos(2\theta - \omega)), \tag{2.9}$$

$$q_z = \frac{2\pi}{\lambda}(\sin\omega + \sin(2\theta - \omega)). \tag{2.10}$$

The location of the Si(111) peak for Cu Kα X-rays is ($\omega = 14.22°$, $2\theta = 28.44°$) which lies on the $q_x = 0$ line. The Si(531) peak, on the other hand, is accessible at ($\omega = 28.4°$, $2\theta = 114.2°$). This technique is particularly useful for structural analysis of epitaxial thin films, which only have a limited number of peaks visible in q_z. In the

case of epitaxial MnGe(111), only the (111) and (333) peaks are accessible by $\theta - 2\theta$ measurement. The presence of additional peaks such as the (112), (221) and (331) reflections on a reciprocal space map were used to confirm the B20 structure.

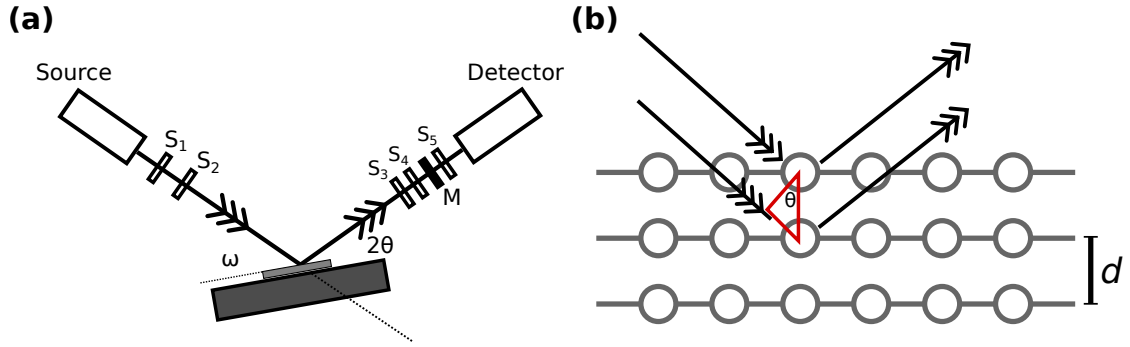

Figure 2.3: (a) Depiction of the diffractometer used for the structural analysis of the MnGe films. The sample stage and detector rotate to vary the diffraction angle 2θ. The X-ray beam is collimated onto the sample using two slits, S_1 and S_2. Diffracted X-rays then travel through an antiscatter slit S_3 (to limit stray X-rays from entering the detector) and two monochromator slits, S_4 and S_5 as well as the monochromator M. (b) Visual representation of Bragg's law. For two scattered X-rays to be seen at the detector, they must constructively interfere. Their path length difference can be calculated using the red triangle, yielding Equation 2.8.

In Equation 2.6, the term in front of the integral is called the geometric structure factor and determines the allowed scattering vectors $q' - q$. The integral is called the structure factor and describes contributions to the scattering due to the distribution of scatters within the unit cell. The diffracted intensity is given by the square modulus of this equation. Other factors such as the Lorentz polarization factor (related to experimental geometry) and Debye-Waller factor (associated with thermal vibrations) contribute corrections to the intensity. In this thesis, the main focus is on analyzing the impact of the geometric structure factor to the XRD data.

For a sufficiently large crystal, the geometric structure factor is sharply peaked, whereas for a finite film, this term gives rise to intensity fringes on either side of the diffraction peak. A simple explanation for these Kiessig fringes is that plane waves scattering off sucessive lattice planes will combine at the detector in a Fourier series, whose profile will approach a Dirac delta function for many layers, and remaining broad for thin films, with the presence of Gibbs oscillations. This is illustrated by

calculating a simple model of the geometric structure factor. For N layers of lattice planes with spacing $d_{h,k,\ell}$ corresponding to the $(hk\ell)$ reciprocal lattice vector, one can write the peak instensity as proportional to:

$$\left|\sum_{\mathbf{R}} \exp\left(-i\mathbf{G}\cdot\mathbf{R}\right)\right|^2 = \left|\sum_{n=1}^{N} \exp\left(-Gna\right)\right|^2 = \frac{\cos(4\pi N d_{h,k,\ell}\sin\theta/\lambda) - 1}{\cos(4\pi d_{h,k,\ell}\sin\theta/\lambda) - 1}\,, \qquad (2.11)$$

where a is the lattice parameter. By fitting Kiessig fringes of an XRD peak for N, the thickness $d_{\mathrm{f}} = N d_{h,k,\ell}$ of the film can be estimated. For the MnGe thin films studied, this approach was effective for film thicknesses below approximately 40 nm. Above this thickness, the the fringe spacing diminishes until only a small shoulder on the side of the MnGe(111) peak could be resolved.

It was found by Karhu [66] for the case of MnSi thin films, an analytic expression for the Kiessig fringes which includes interfacial roughness was able to accurately capture both the film thickness and amplitude of the fringes. This was derived in Reference [67] using kinematical scattering theory. For a film with a mosaic structure where there is incoherent scattering from various regions, the intensity is given by

$$I(G) = \frac{|F|^2}{G^2}\left[2 - 2\exp\left(-\frac{1}{2}G^2({\sigma_L}^2 + {\sigma_U}^2 - 2r_{\mathrm{c}}\sigma_L\sigma_U)\right)\cos(NGd)\right], \qquad (2.12)$$

where σ_L (σ_U) is the roughness of the lower (upper) interface, F is the structure factor, and r_{c} is the correlation coefficient between the two interfaces. In the zero roughness limit, this expression approaches Equation 2.11. Figure 2.4 depicts a representative XRD peak for a 22.9 nm MnGe film. A simulation is given using both Equations 2.11 and 2.12.

2.2.2 Reflection high energy electron diffraction

Reflection high energy electron diffraction (RHEED) is the technique used for *in-situ* characterization during the growth of the films. A beam of high energy (12 keV to 15 keV) electrons is focused onto the sample at low incident angle. The electrons undergo diffraction at the sample and the diffraction pattern can be imaged on a fluorescence screen. Due to this glancing incident angle, the RHEED beam only penetrates the first few atomic layers [68, 69]. This makes RHEED extremely surface-sensitive and it is an invaluable tool for monitoring the growth of epitaxial films.

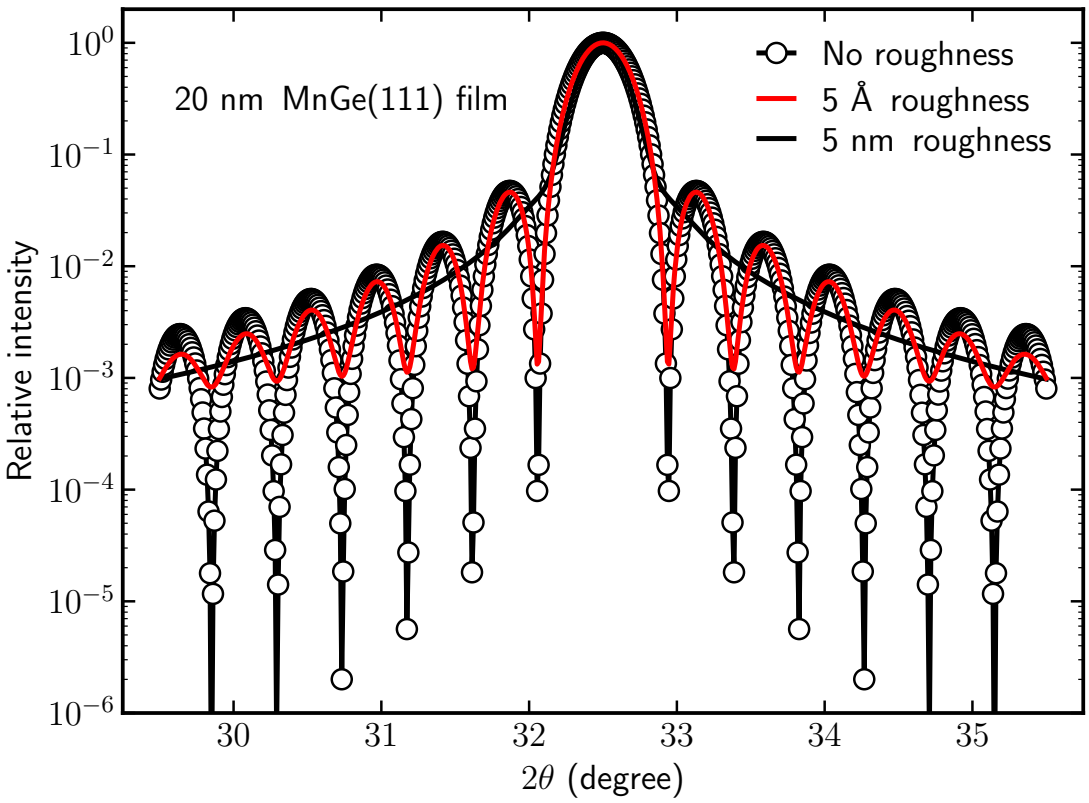

Figure 2.4: Simulation of the MnGe(111) X-ray peak for a film thickness of 20 nm. The curve with open circles is generated with Equation 2.11 with no interface roughness. The red (black) curve was generated with Equation 2.12 using an interfacial roughness of 5 Å (5 nm). Diffuse scattering from the roughness diminishes the sharp Kiessig fringes. For a sufficiently rough film, the fringes are completely washed out.

Diffraction in RHEED can again be understood by Equation 2.7 and the Ewald sphere construction. For this case, the lattice in real space is effectively two-dimensional and therefore the reciprocal space is a series of rods with very large extent in the q_z direction. The intersection between the Ewald sphere and reciprocal rods are points, which satisfy the diffraction condition. Because of this geometry, the diffraction spots lie on concentric circles, if the film is flat. The RHEED screen reveals the intensity of diffracted electrons, and all information about their phase is lost. For this reason, a RHEED pattern does not contain enough information to completely describe the surface lattice that produced it. Analysis of RHEED is a game of pattern recognition: the experimenter calculates a diffraction pattern based on a proposed surface lattice, which is compared to the observed RHEED spots.

Defects or features in the surface will have a notable impact on the resultant RHEED pattern. Real crystals and films are not always ideal. It is uncommon for heteroepitaxial structures to form a completely uniform overlayer and there will often be small islands or domains of finite size. The size of these domains is typically smaller than the coherence length of electron beam, allowing them to be imaged. This broadens the horizontal extent of the reciprocal rods, leading to a broadening of diffraction spots into streaks [68, 69]. The spacing between the islands determines the thickness of the streaks, with larger domains yielding sharper streaks (or points). It should be noted that if a film is composed of finitely sized domains, this does not imply that it is polycrystalline. The diffraction in polycrystalline films will be averaged over all possible orientations of the crystallites, resulting in concentric circles of intensity, rather than distinct spots or streaks which lie on the Laue circles. Depictions of various surfaces and their resultant RHEED patterns are shown in Figure 2.5. In this work, RHEED of the MnGe predominantly featured spots and thin streaks, indicating a relatively flat crystalline surface.

The surface structure of a crystal is often different from that of the bulk. The surface atoms form bonds with their neighbours on the surface in a reconstruction: the resulting dimers lower the symmetry of the surface and this is observable with RHEED. For example, a clean Si(111) surface will undergo a (7×7) reconstruction when heated in vacuum to sufficiently high temperature. The reconstructed surface unit cell is larger than the bulk by a factor of 7 in both in-plane directions and produces fractional-order diffraction spots between the spots owing to the bulk.

In the case of CrSi(111) on Si(111), the film is lattice matched to Si with a 30° rotation. The epitaxial relationship is:

$$\mathrm{CrSi}[0\bar{1}1] \parallel \mathrm{Si}[\bar{1}\bar{1}2]$$
$$\mathrm{CrSi}[111] \parallel \mathrm{Si}[111]$$
$$\mathrm{MnGe}[0\bar{1}1] \parallel \mathrm{CrSi}[0\bar{1}1]$$
$$\mathrm{MnGe}[111] \parallel \mathrm{CrSi}[111]$$

The surface of the CrSi/Si(111) system is shown in Figure 2.6. The surface unit cell of CrSi(111) is $\sqrt{3}$ times larger than that of Si(111). Therefore the RHEED spot separation for CrSi(111) is 3 times smaller than that of Si(111) for a beam along the

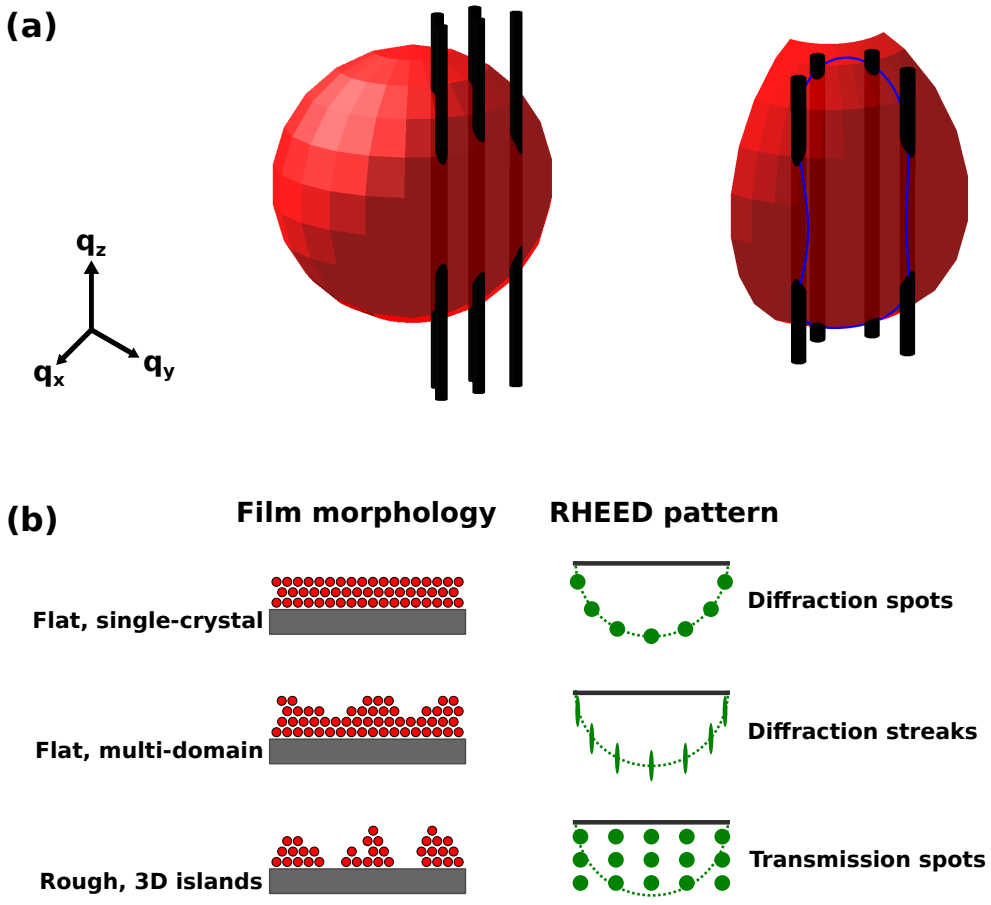

Figure 2.5: (a) Ewald sphere construction for RHEED, depicting the intersections of reciprocal rods which appear on a Laue circle, shown in blue. (b) Relation of the film morphology to the resultant RHEED pattern. Flat films give sharp spots or streaks which lie on the Laue circles. Rough films yield transmission spots, similar to the case of XRD.

Si[$1\bar{1}0$] direction. When the beam is along Si[$\bar{1}\bar{1}2$], the periodicity is the same. This is falsely referred to in the literature as a $\sqrt{3} \times \sqrt{3}$ reconstruction, but there is no reconstruction of the CrSi(111) surface. A sketch of the predicted RHEED pattern for this sytem is also given in Figure 2.6, wherein the pattern consists of only integer order diffraction spots for one orientation, and two fractional order spots between each integer spot when the sample is rotated.

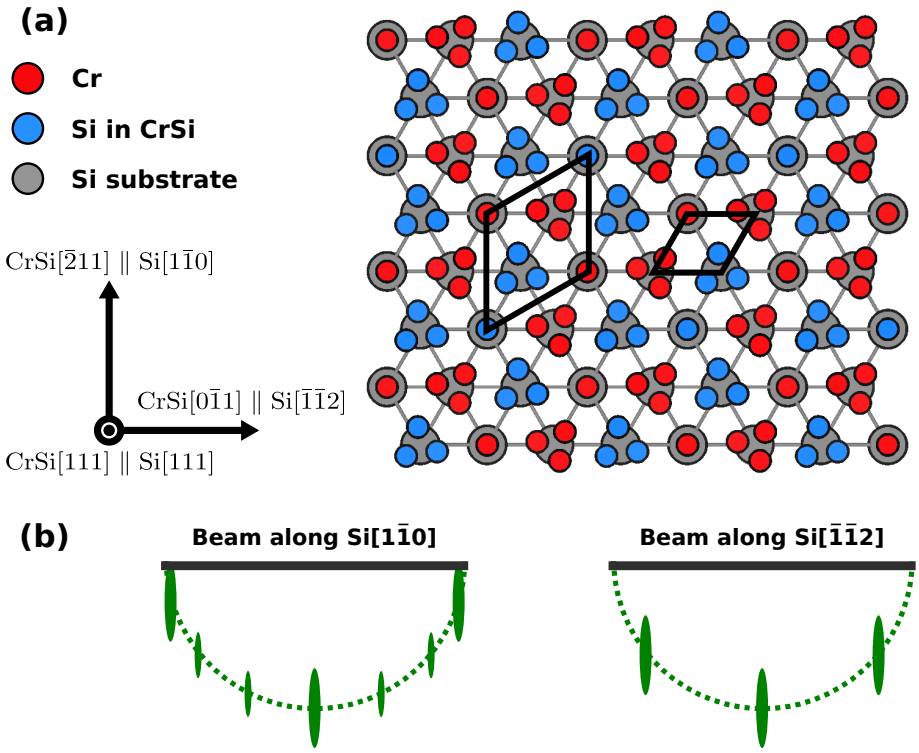

Figure 2.6: (a) Representation of the epitaxial relationship of a pseudomorphic (111)-oriented B20 film on Si(111). In this case, CrSi is shown. The surface unit cell of CrSi (Si) is shown on the left (right). The surface unit cell of CrSi is $\sqrt{3}$ times larger than that of Si, and rotated by 30°. (b) Calculated RHEED pattern for this system. The additional dim spots appear as fractional-order spots for sufficiently thin layer of CrSi. For a thicker B20 film, the intensity appears similar for all the spots.

2.3 X-ray reflectometry

In XRD, the wavelength λ is on the order of the plane spacing $d_{h,k,\ell}$, which allows for the identification of structures ranging from 1 Å to 9 Å at intermetiate to high angles. As the scattering angle is decreased, larger-scale structures are being probed. X-ray reflectometry (XRR) is a technique which uses grazing incidence angles and is sensitive to interfacial spacing. XRR was used to determine the thickness and roughness of the MnGe films.

Since $q' - q$ is much smaller than the G which give rise to Bragg diffraction, one can employ a continuum model for XRR. The sample will appear as an ideal Drude material due to the high frequency of the X-rays. This results in a complex index of

refraction which is slightly less than unity [70]. This can be written as

$$n = 1 - \frac{\lambda^2}{2\pi} r_e n_s (f' + if'') \tag{2.13}$$

where n_s is the scatterer number density, $r_e = 2.82\,\text{fm}$ is the Thomson scattering length (the classical radius of the electron), and $f' + if''$ is the X-ray scattering factor. The imaginary part of the refractive index describes the absorption of X-rays, which is typically negligible for energies not near resonance. Cu Kα is sufficiently far from any absorption edges for Mn and Ge. In the absence of absorption, the refractive index may be approximated in terms of the effective density of electrons, $\rho_e \approx n_e f'$:

$$n = 1 - \frac{\lambda^2}{2\pi} r_e \rho_e \,. \tag{2.14}$$

Below a critical angle θ_c, the incident X-rays undergo total *external* reflection [70]. This is related to the refractive index by $\cos\theta_c = n$, where θ_c is small. This is approximately given by

$$\theta_c = \lambda \sqrt{\frac{r_e \rho_e}{\pi}} \,, \tag{2.15}$$

The quantity $r_e\rho$ is the scattering length density (SLD), which measures the effective scattering ability of a material.

The X-rays incident on an interface are modelled as plane waves consisting of an indicent, transmitted and reflected wave. By applying the appropriate boundary conditions, the reflectivity can be related to the scattering wavevector as:

$$R = \left| \frac{q_z - \sqrt{{q_z}^2 - {q_c}^2}}{q_z + \sqrt{{q_z}^2 - {q_c}^2}} \right|^2 , \tag{2.16}$$

which simplifies to $R = (q_c/2q_z)^4$ for wavevectors sufficiently far above the critical wavevector q_c. This is the Fresnel reflectivity for an infinite material. A sample Fresnel reflectivity curve is given in Figure 2.7. Above the critical angle, the reflectivity is unity as the X-rays are totally externally reflected. As 2θ increases, the reflectivity drops drastically. The penetration depth of the X-rays is relatively small (typically no more than 3 nm) below the critical angle, and sharply increases to several µm above the critical angle.

For more complicated systems such as an MBE-grown thin film, interference between reflected X-rays from each layer will give rise to Kiessig fringes on the Fresnel

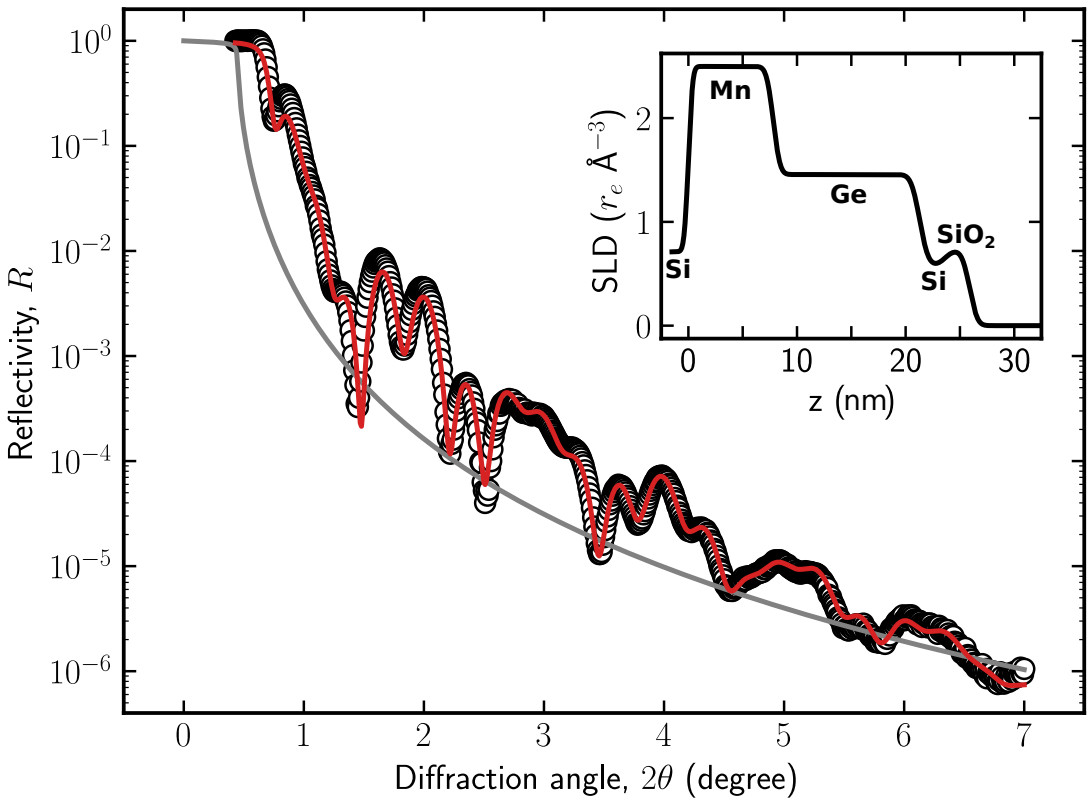

Figure 2.7: Sample XRR curves. The dots show experimental data for a trilayer consisting of 7.8 nm Mn/13.7 nm Ge/2.6 nm Si on a Si substrate. The red line is a fit to this data using `GenX`. The grey line shows simulated Fresnel reflectivity from an infinite Si substrate. The critical angle of the trilayer is larger than that of the Si due to its larger scattering length density. The inset shows the calculated SLD as a function of depth in the trilayer, in units of the Thomson radius per cubic angstrom.

reflectivity. Modelling these is best done numerically. Figure 2.7 shows an example XRR curve for a 7.8 nm Mn/13.7 nm Ge/2.6 nm Si trilayer. Samples of this kind were used to calibrate the MBE deposition rates. All XRD data shown in this thesis was fit using the `GenX` software [71].

Measurements were taken with the same diffractometer used for XRD. The sample was aligned by use of a rocking curve below the critical angle. This ensures that the diffractometer scans reciprocal space normal to the surface of the sample, which may not necessarily correspond directly to the Si(111) planes. If the substrate is miscut, the surface will be a small angle misaligned relative to the planes. For the substrates used in this thesis, the miscut is less than 0.5°, per the manufacturer.

2.4 Magnetometry

The magnetic properties of select MnGe films were studied with a superconducting quantum interference device (SQUID) magnetometer. This technique relies on Faraday's induction law, and the Josephson effect. The former states that a time varying magnetic flux Φ_B will produce an electromotive force (EMF) ε in a conducting loop,

$$\varepsilon = -\frac{\partial \Phi_{\mathrm{B}}}{\partial t}\,. \tag{2.17}$$

The Josephson effect is a phenonemon which causes a superconducting current to flow across a thin insulating barrier separating two superconductors: a Josephson junction [72]. For sufficiently low current, there will be no voltage across the junction and above a particular critical current, the voltage will increase.

A SQUID magnetometer consists of several important parts. A superconducing magnet is used to generate large magnetic fields and a superconducting decection coil couples inductively to the sample, which is connected to the SQUID. When the sample is oscillated through the pickup coil, its time-varying flux induces a supercurrent in the wire to oppose the change. Since the flux inside a superconducting loop is quantized by $\Phi_0 = h/2e$ (where h is Planck's constant and e is the elementary charge), the induced supercurrent will vary to set the flux to the nearest integer multiple of the flux quantum [73]. The SQUID is coupled to the pickup coil, so an identical current flows trough the SQUID.

A SQUID consists of a closed superconducting loop inside of which there may be one or several Josephson junctions bridging the path of the supercurrent [74]. A bias current is applied such that small changes in flux will result in a large voltage across the Josephson junctions. The SQUID in this configuration is therefore an extremely sensitive flux-to-voltage transducer, with sensitivity set by Φ_0 [72]. By interpolating between flux quanta, this resolution can be improved further in data processing. Because the SQUID resolution is in the fT range, whereas the Earth's magnetic field is on the order of 50 µT (corresponding to hundreds of flux quanta over the size of a SQUID sensor), the magnetometer includes a superconducting magnetic shield to isolate the SQUID from the outside. In addition to its immense sensitivity, a SQUID can be made to operate in magnetic fields as large as 7 T.

The magnetometry measurements collected in this thesis used the reciprocating

sample option (RSO) of a Quantum Design Magnetic Properties Measurement System (MPMS) SQUID magnetometer, capable of magnetic fields up to 7 T. In the RSO mode, the sample is moved vertically about the centre of the detection coil, which is configured as a second-order gadiometer. This gradiometer is only sensitive to the second spatial derivative of the time-dependent flux, which eliminates many sources of noise in the signal. Samples with total magnetic moment as low as $1 \times 10^{-11}\,\mathrm{A\,m^2}$ can be accurately measured by measuring the SQUID voltage versus sample position, and modelling the sample as a perfect dipole. The coils in the second-order gadiometer have longitudinal radius of $r = 0.97\,\mathrm{cm}$ and the upper/lower loops are situated a distance $\beta = 1.519\,\mathrm{cm}$ from the two central loops. Given these parameters, the optimal extent of a sample in the direction of the RSO mode oscillation is approximately 4 mm so it can be treated as a point dipole.

A schematic of the setup is shown in Figure 2.8. The equation which describes the voltage V_{RSO} as a function of distance d produced by an ideal dipole traversing through a second-order gradiometer is:

$$V_{\mathrm{RSO}}(d) = z_0 + \ell d + \mu\eta\left[\frac{2}{(r^2+d^2)^{3/2}} - \frac{1}{(r^2+(d+\beta)^2)^{3/2}} - \frac{1}{(r^2+(d-\beta)^2)^{3/2}}\right], \tag{2.18}$$

where d is the sample position with respect to the coil centre, μ is the dipole moment, η is a sensitivity factor, and r and β are the coil radius and separation, respectively. An electronic drift which is linear in position is parameterized by ℓ and z_0 is a constant voltage offset. A sample RSO curve and accompanying fit are given in Figure 2.9. It is sometimes the case that significant time-dependent drift must also be subtracted. This is also approximated as linear (d is sinusoidal in time) and subtracted before fitting the voltage.

The samples were oriented such that the field was either parallel or perpindicular to the plane of the film. When the field is applied along MnGe[111], this is referred to as out-of-plane. There are two in-plane directions for a MnGe(111) film. These are MnGe[$0\bar{1}1$] and MnGe[$\bar{2}11$]. Because the magnetic anisotropy for a cubic material is isotropic in the (111) plane, these directions should be equivalent. For consistency, the field was always applied in the MnGe[$0\bar{1}1$] direction; this was chosen because it is a higher symmetry direction. For the rest of this work, in-plane refers to MnGe[$0\bar{1}1$].

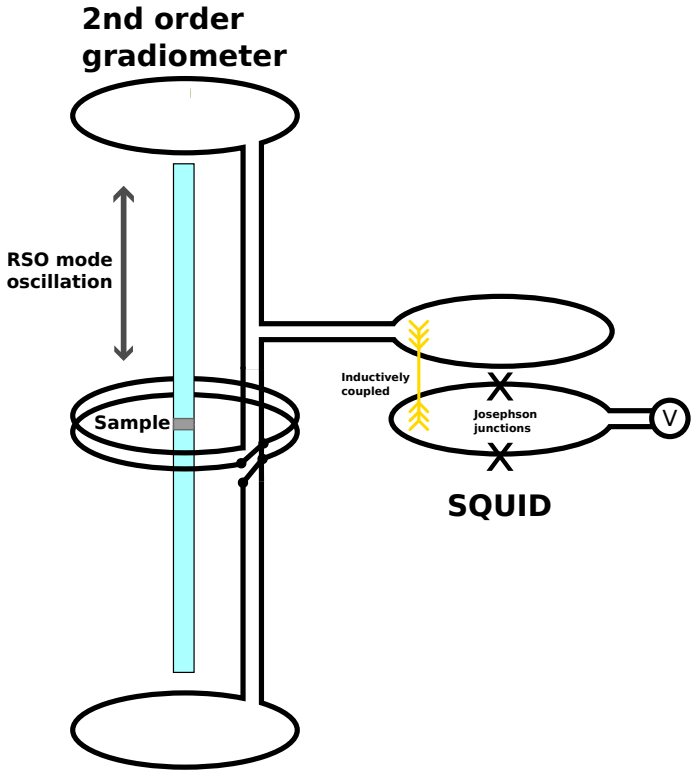

Figure 2.8: Schematic of the 2nd order gradiometer in a SQUID magnetometer. The sample oscillates inside the coils and induces an EMF which is only sensitve the second order derivative in position. The sample is wedged into a plastic straw which is uniform and so will not induce an EMF in the pickup coil. The coils are inductively coupled to a SQUID.

The samples were cleaved into rectangular pieces with nominal dimensions 8 mm × 4 mm (for field to be applied in-plane), or 6 mm × 4 mm (for field to be applied out-of-plane) and inserted into a plastic straw. Since the magetometer measures the total moment of the sample μ, the magnetic signal at high fields is dominated by the diamagnetic response of the substrate. To account for this, the magnetic moment of the substrate was fit at high field (much larger than the critical field for the transition to the field-induced ferromagnetic state) and the substrate susceptibility $\chi_{\mathrm{Si}} = \partial M/\partial H$ was subtracted from the measured moment. The magnetization was calculated by dividing the corrected moment by the film volume, V_{f}. The volume of a sample of MnGe was determined by measuring its area with digital calipers and its thickness using XRR.

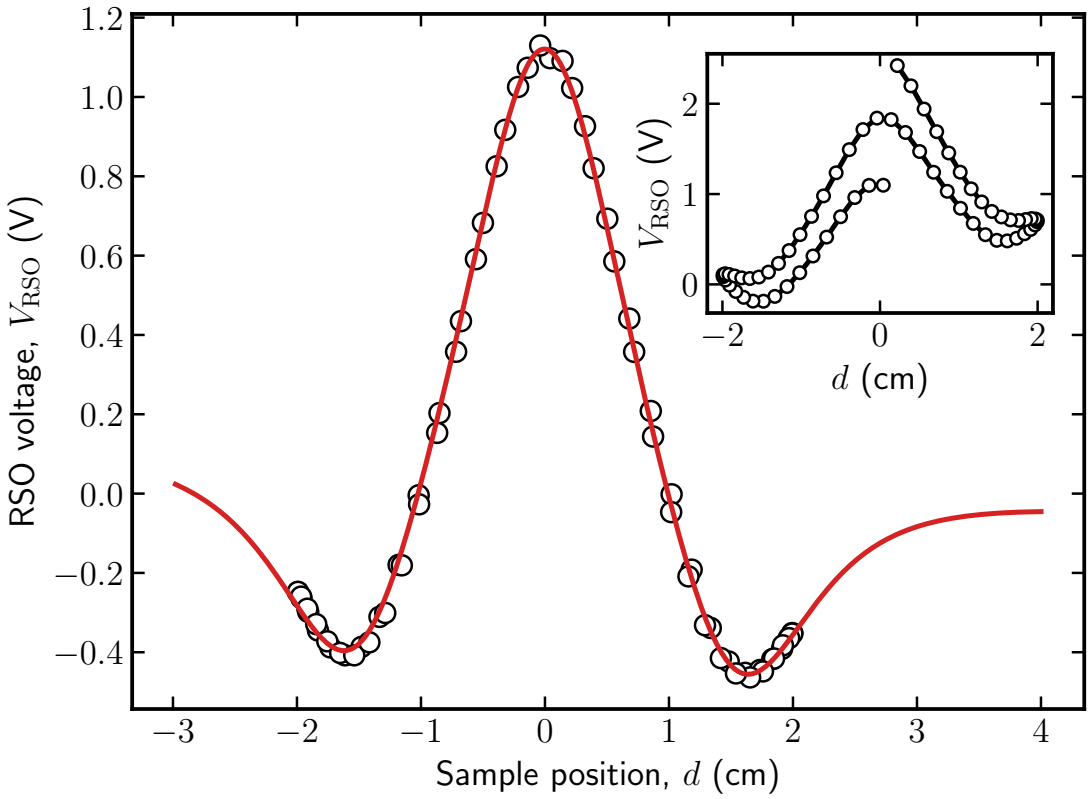

Figure 2.9: Sample SQUID RSO voltage curve with accompanying fit. The sample moment from this particular curve was $1.5 \times 10^{-7}\,\mathrm{A\,m^2}$. The inset shows the form of a voltage curve with significant time-dependent drift.

The diamagnetic susceptibility of Si is only weakly temperature-dependent. The large saturation field of MnGe makes the subtraction of the Si susceptibility impossible at low temperatures, since the film cannot be completely saturated and χ_{Si} cannot be estimated. At higher temperatures, the magnetization more slowly approaches its saturation value. For consistency, the substrate susceptibility was taken to be constant in temperature. A value of χ_{Si} was extracted from the M versus H measurement at an intermediate temperature, which was used for all temperatures. The diamagnetic subtraction is detailed in Figure 2.10. This procedure also includes the assumption that MnGe has zero susceptibility $\chi_{\mathrm{HF}} = 0$ above the saturation field. This is not necessarily correct for itinerant magnets, but the value is small for bulk MnGe, $\chi_{\mathrm{HF}} \approx 6\,\mathrm{kA\,m^{-1}\,T^{-1}}$ at 100 K [17]. Previous studies on MnSi thin films found a high-field susceptibility which was comparable to bulk MnSi, which was also small.

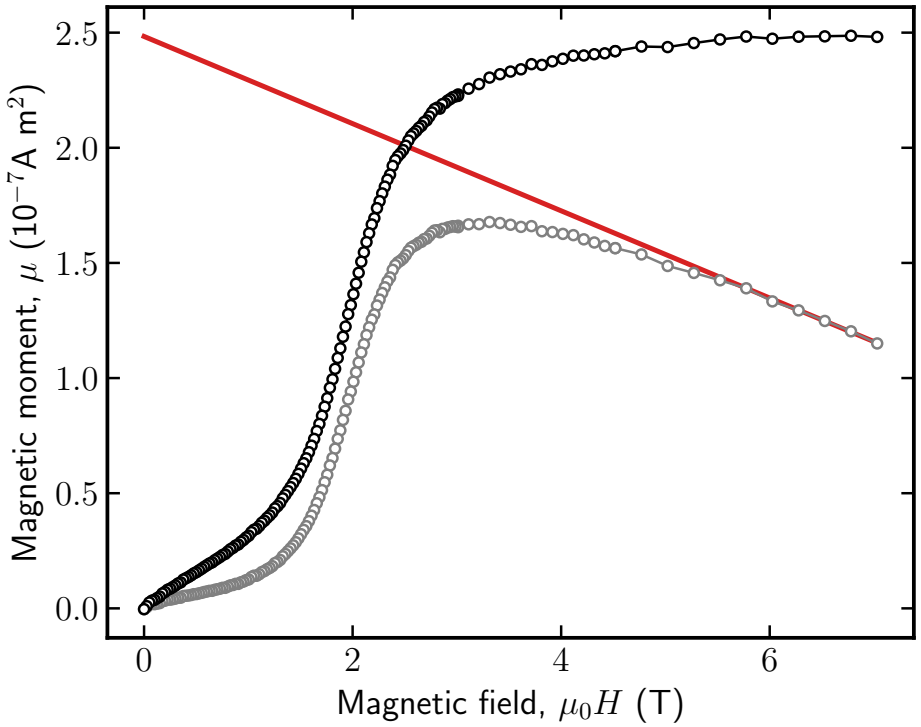

Figure 2.10: Illustration of the procedure used to subtract the magnetic signal from the Si substrate. The grey circles show the magnetic moment extracted from the RSO voltage curves using Equation 2.18. A linear fit shown in red was applied to the data above 6 T. The slope of this line, $-1.893 \times 10^{-8}\,\mathrm{A\,m^{-1}\,T^{-1}}$, represents χ_{Si}. The intercept, $2.48 \times 10^{-7}\,\mathrm{A\,m^2}$ represents the saturated moment of the MnGe film. When $\chi_{\mathrm{Si}}\mu_0 H$ is subtracted, the data shown by black circles is obtained, which is the moment of just the film. The remanent moment is unaffected by this subtraction.

The positive value of χ_{HF} leads to the magnitude of χ_{Si} being underestimated. Measurement of the remanent magnetization is not affected by this subtraction. Furthermore, the magnetization obtained from extrapolating the high-field data to zero (the red line in Figure 2.10) is also insensitive to corrections involving χ_{HF}. Assuming χ_{Si} is temperature-independent and neglecting χ_{HF} only amounts a correction of a few percent in the magnetization.

The moment μ is extracted from the RSO voltage curves using Equation 2.18. The fitting procedure is as follows: before the measurement, the sample is centred within the coils by measuring V_{RSO} for all d within the motor range of the magnetometer.

It was checked that the sample did not move from this position over the course of all measurements. For each RSO voltage curve, the position with respect to the centre of the coils is fixed and Equation 2.18 is applied using a bounded least squares algorithm. The initial moment is set around $5 \times 10^{-8}\,\mathrm{A\,m^2}$ and the drift parameters are initialized to zero, to avoid biasing the refinement. After a sussessful fit has been obtained, the constraints are relaxed and the centre of the curve is allowed to move by at most 1 mm to account for a shift due to thermal expansion or contraction in the apparatus. The previous refined parameters are allowed to vary by a certain amount, typically $\pm 10\%$. The parameters from the current fit of V_{RSO} are then used to initialize the fit of the next V_{RSO} curve. At each field-temperature point, eight V_{RSO} curves were measured, fit and averaged. If the moment from one measurement is greater than 1.4 standard deviations from the mean, it is rejected in the average.

The method described here was proven to be significantly more accurate than the automatic fitting performed by the `MultiVu` program which controls the magnetometer. The main improvement is restricting the sample location in the second refinement, which is effective for the case where the V_{RSO} signal is comparable to the noise. This was particularly important for regions in the $M(H)$ or $M(T)$ scans where the total moment goes to zero. Since the `Multivu` program is specifically calibtrated to each magnetometer, it was verified that calculated moments from V_{RSO} exactly reproduced those fitted by `Multivu`, except for a reduction in unphysical refined moments. A comparison of the two methods is given in Figure 2.11.

2.5 Magnetotransport

To complement the SQUID magnetometry measurements, electrical transport measurements were conducted. This was accomplished by measuring the Hall effect in various temperatures and magnetic fields. The Hall effect involves a transverse voltage that is created when a current-carying material is exposed to a magnetic field. In the traditional geometry for a thin film, the field is applied out-of-plane and the current is applied in-plane. The Hall voltage appears orthogonal to both the electric and magnetic fields and (the ordinary Hall effect) can be explained simply by the Lorentz force law:

$$\mathbf{F} = e(\mathbf{v} \times \mathbf{B})\,, \tag{2.19}$$

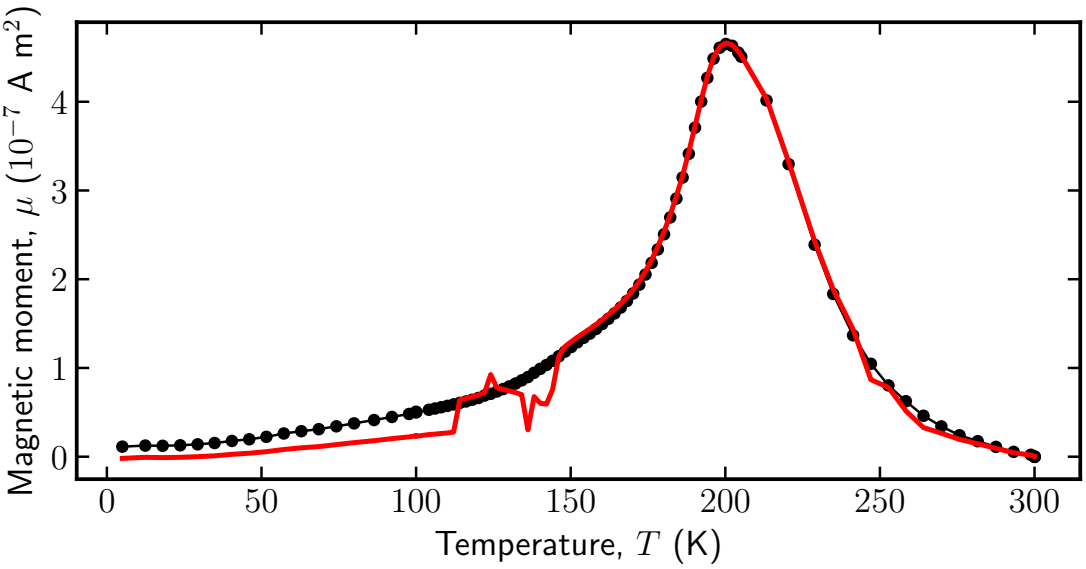

Figure 2.11: Illustration of the algorithm used to fit SQUID magnetometry data. The red line is the moment determined by `Multivu`, and the black circles were obtained from the fitting procedure used in this thesis. The two values agree, except for a reduction in unphysical noise.

which describes the force on a charged particle e with velocity v (collinear with the current) inside the magnetic field $\mathbf{B}$. This force causes the charge carriers to accumulate on one side of the sample, inducing the transverse Hall voltage. The intrinsic quantities which are typically reported are the longitudinal and Hall resistivities, ρ_{xx} and ρ_{yx}, respectively. These appear as diagonal and off-diagonal elements in the resistivity tensor defined from Ohm's law, $E_\alpha = \rho_{\alpha\beta} J_\beta$. The Hall effect in topological magnets contains three contributions:

$$\rho_{yx} = \rho_{yx}^{\mathrm{O}} + \rho_{yx}^{\mathrm{A}} + \rho_{yx}^{\mathrm{T}} \,, \tag{2.20}$$

where ρ_{yx}^{O} is the ordinary Hall effect:

$$\rho_{yx}^{\mathrm{O}} = \mu_0 R_0 H \,, \tag{2.21}$$

and ρ_{yx}^{A} and ρ_{yx}^{T} are the anomalous and topological Hall effects, respectively. The anomalous Hall effect occurs in magnetic materials and depends on the magnetization. The topological Hall effect results from the magnetic field in real space that an electron experiences while adiabatically following a magnetization texture with

nontrivial topology. The presence of a topological Hall effect has been used to argue for the presence of non-coplanar spin textures such as a skyrmion or spin-hedgehog lattice in MnSi and MnGe. It has also been found that an additional contribution to the Hall effect occurs from the conical phase in MnSi.

Complex modelling and fitting of the Hall resistivity has been done by some groups but is outside the scope of this thesis. Instead, it is used to search for magnetic phase transitions. Transport measurements were performed in a Quantum Design DynaCool Physical Properties Measurement System (PPMS). The samples were cleaved into rectangles of length 6 mm and width less than 2 mm. Constant current leads were wire bonded to the short edges of the sample and transverse voltage leads were attached to the long edges of the sample, halfway between the current leads.

The electric potential ϕ was calculated from Laplace's equation $\nabla^2\phi = 0$, with fixed potential at the leads, and additional boundary conditions at the edges of the film given by $\mathbf{J} \cdot \hat{\mathbf{n}} = 0$, where $\hat{\mathbf{n}}$ is a unit vector normal to the sample surface. Laplace's equation was solved using the finite difference method for a rectangle with a length-to-width ratio of 3:1. A plot of the solution is shown in Figure 2.12. It can be seen that the current is extremely uniform over the majority of the sample. This method of preparation is much simpler than photolithographic patterning that has been employed by some, and there appears to be no loss in data quality.

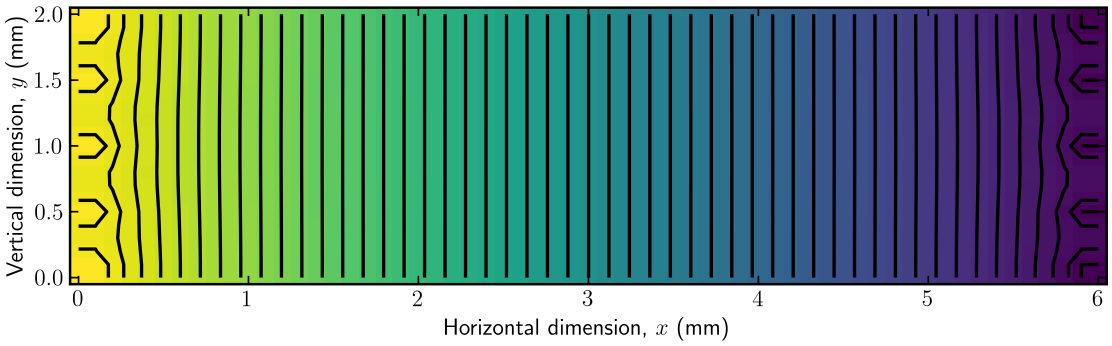

Figure 2.12: Calculated electric field for the rectangular geometry used for transport measurements, obtained by solution of Laplace's equation. There are five constant current leads bonded wire bonded to the edges of the sample. The colour map shows the variation of the potential and the black lines are equipotential contours. In this geometry, the current is extremely uniform.

The longitudinal resistivity is necessarily symmetric in the magnetic field, whereas

the Hall resistivity is necessarily antisymmetric. The observed data was properly symmetrized prior to analysis, using the following relations:

$$\rho_{xx}(H) = \frac{1}{2}(\rho_{xx}(H) + \rho_{xx}(-H))\,; \tag{2.22}$$

$$\rho_{yx}(H) = \frac{1}{2}(\rho_{yx}(H) - \rho_{yx}(-H))\,. \tag{2.23}$$

Due to limitations on number of simultaneous measurements in the PPMS, the longitudinal resistivity was not measured during the experiment. It was instead extracted from the transverse resistivity resulting from the small horizontal misalignment of the voltage leads. This separation is on the order of 50 µm and the uncertainty in this measurement is as large as 10%. As a result, the longitudinal resistivities reported in this thesis will be given as a ratio, either $\rho_{xx}(T)/\rho_{xx}(T = 5\,\mathrm{K})$ or $\rho_{xx}(H)/\rho_{xx}(H = 0)$. The field and temperature dependence of the measured resistivity is assumed to be unaffected by the calculation so meaningful analysis can still be extracted. If an accurate measure of the longitudinal resistivity is required, *i.e.*, for calculating the Hall conductivity, $\sigma_{\mathrm{H}} = \rho_{yx}/(\rho_{xx}^2 + \rho_{yx}^2)$, the voltage leads should be re-bonded to the sample in a longitudinal configuration and the measurements repeated in a future study.

Chapter 3

Structural characterization

In this chapter, the growth of the MnGe thin films is discussed. It is shown that B20 MnGe thin films can be stabilized atop a B20 CrSi template layer. A review of the temperature and composition dependence on the structure is also presented. XRR and XRD are used to investigate structure and quality of the films, which reveals that they crystallize as single-phase MnGe, with interfacial roughness less than 6 Å.

3.1 Sample preparation

MnGe thin films were prepared on high resistivity ($\rho > 10\,\mathrm{k\Omega\,cm}$) Si(111) wafers. The wafers were first ultrasonically degreased for 15 minutes in acetone and methanol, followed by a rinse and overflow in de-ionized nanopure water. A 1:2:10 solution of NH_4OH, H_2O_2 and H_2O was prepared at 70 °C and the wafer was soaked for 10 minutes, followed by another rinse in de-ionized nanopure water. The wafer was then dried with nitrogen gas and immediately loaded into the MBE system and brought to UHV over 3 hours. The wafer was then degassed for longer than 12 hours at a temperature of approximately 570 °C. The SiO_2 layer on the surface of the Si was desorbed by rapidly flashing the substrate to 830 °C and holding for 1 hour. The substrate was then allowed to cool to 640 °C at a rate of less than $1\,^{\circ}\mathrm{C\,s^{-1}}$. At this temperature, a 20 nm buffer layer of Si was deposited before the sample was cooled to room temperature again at a rate of less than $1\,^{\circ}\mathrm{C\,s^{-1}}$.

In-situ RHEED with an electron energy of 15 keV revealed a sharp (7x7) reconstruction which is indicative of a flat surface. Complementary *ex-situ* atomic force microscopy (AFM) images reveal that the surface is flat, with step heights of approximately 3 Å, which corresponds to the atomic spacing between Si(111) planes of 3.14 Å. The terrace widths were approximately 150 nm, corresponding to a wafer miscut of approximately 0.1°. The root-mean-square (RMS) roughness was found to be between 2 Å and 8 Å for each substate, measured over an area of 10 µm × 10 µm.

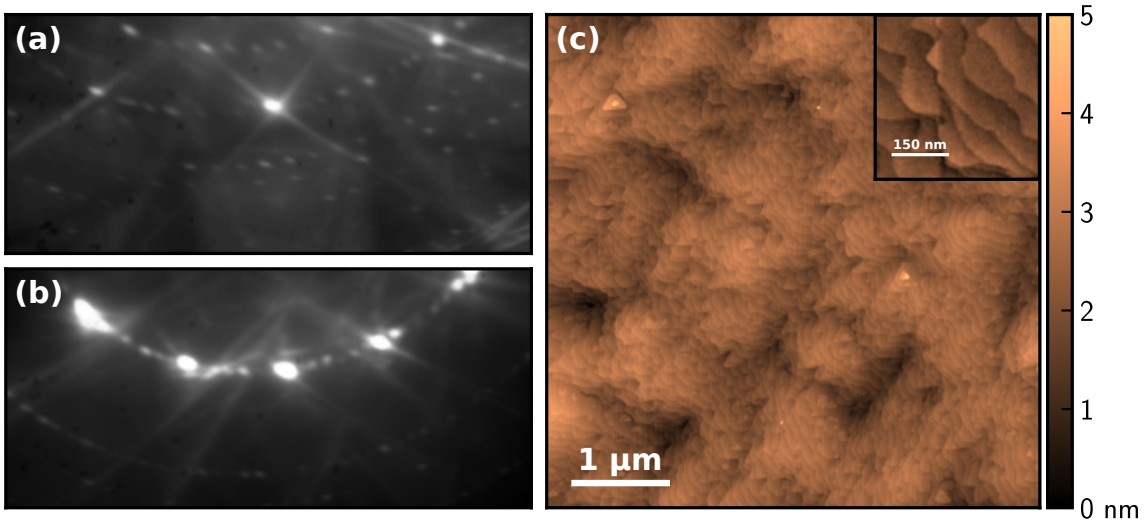

Figure 3.1: (a) and (b) RHEED patterns of a Si substrate showing a (7x7) reconstruction. The electron energy was 15 keV. The beam is along ⟨110⟩ in (a) and ⟨112⟩ in (b). Kikuchi lines are visible in both orientations. (c) AFM image of the surface, showing a surface with low roughness comprised of atomic-scale terraces. The inset shows the terraces in greater detail.

The RHEED and AFM from the substrate are shown in Figure 3.1.

The CrSi template was grown using the method described by Higashi *et al.* for MnSi. A 2 QL template of nominal thickness 5.3 Å was grown by depositing a stack consisting of 0.5 QL Si / 1 QL Cr / 0.5 QL Si. The nominal thickness of 1 QL of Cr is 1.4 Å and 1 QL of Si is 2.2 Å. The 2 QL stack was deposited at room temperature and then heated under periodic RHEED observation to a temperature no greater than 400 °C, above which hexagonal $CrSi_2$ is reported to form. Annealing times ranged from 30 to 75 minutes. Figure 3.2 shows RHEED typical of a CrSi template. The simulated patterns in Figure 2.6 are observed, indicating the formation of a thin, flat layer of CrSi. Comparison of the observed and simulated RHEED patterns is the best method of confirming that B20 CrSi has formed.

Though the expected RHEED pattern of $CrSi_2$, (1×1)R30°, is difficult to distinguish from CrSi, the epitaxy of $CrSi_2$ is reported to be poor below an annealing temperature of 1100 °C. When the CrSi stack was annealed above 400 °C, the quality of the RHEED pattern dropped considerably and transmission spots indicated a

rough surface. The presence of a high-quality $\sqrt{3} \times \sqrt{3}$ pseudo-reconstruction below 400 °C provides strong evidence for the case that B20 CrSi has formed. To add to this, AFM reveals that the surface is indeed extremely smooth, with roughness commensurate to that of the substrate. No impurity crystallites are observed. *In-situ* surface-sensitive techniques such as XPS or Auger electron spectroscopy (AES) would be useful in further confirming the structure of the annealed CrSi (as in References [60, 61]), although production of a reference $CrSi_2$ film may prove difficult. This should be addressed in future studies.

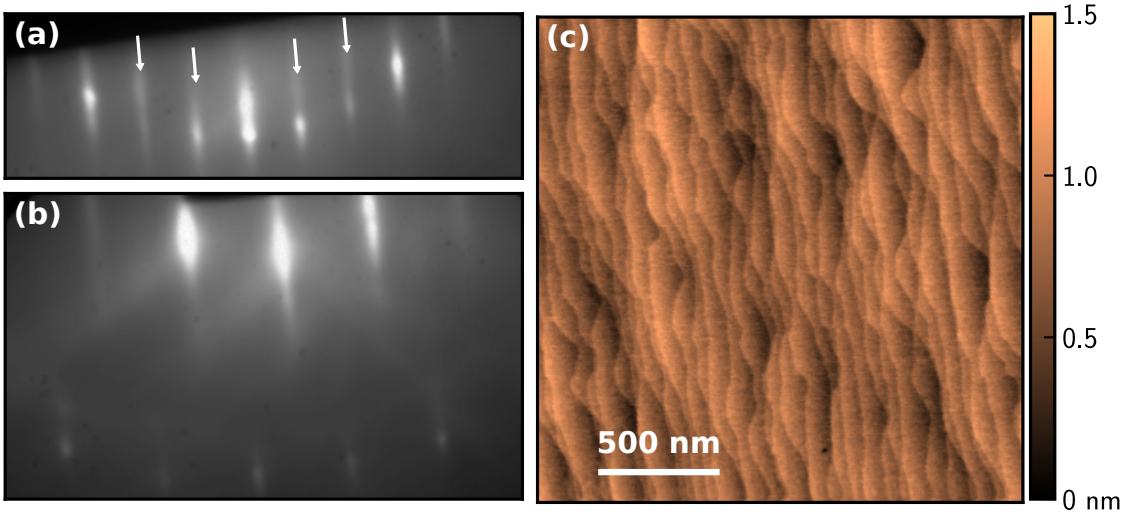

Figure 3.2: (a) and (b) RHEED exhibiting $\sqrt{3} \times \sqrt{3}$ pseudo-reconstruction of the 2 QL CrSi template. In (a), the arrows indicate dim diffraction streaks from the larger periodicity of the CrSi overlayer relative to the substrate. (c) AFM image of the CrSi template which shows low roughness, commensurate to the substrate.

The MnGe was grown using two methods. For the first samples, the Mn and Ge were co-deposited at elevated temperatures. This method is molecular beam epitaxy, where the structure is crystallized as the precursor elements are deposited. The rates of Mn and Ge were matched to achieve the desired stoichiometric ratio. After the desired thickness was deposited, the sample was cooled to below 75 °C at a rate of less than $1\,°C\,s^{-1}$, and a capping layer of amorphous Si or Ge was deposited with thicknesses ranging from 8 to 20 nm.

It was found that room temperature deposition leads to smoother films, as evidenced by calibrations such as in Figure 2.7 or the CrSi template. To exploit this, subsequent MnGe films were grown by co-deposition at a relatively cold temperature

of approximately 100 °C. After the desired thickness was reached, the temperature was then increased to 250 °C and held for 30 to 120 minutes. This technique is known as solid phase epitaxy, where the film undergoes a transition from an amorphous phase to a crystalline phase. The RHEED beam was periodically turned on to check the progress of the annealing. The beam was not left on for extended periods of time, as it will crack CO molecules in the chamber and lead to the deposition of reactive C and O radicals on the surface of the sample. After the desired RHEED pattern was achieved, the sample was allowed to cool to room temperature at a rate of less than 1 °C s^{-1}, after which an amorphous Si or Ge cap was deposited, with thickness between 8 and 20 nm.

After crystallization, RHEED on the MnGe films showed streaks consistent with a flat, highly crystalline surface. This agrees with AFM, which shows circular islands that have coalesced to form a smooth film. Figure 3.3 depicts representative RHEED and AFM images. The RHEED was found to be largely independent of thickness.

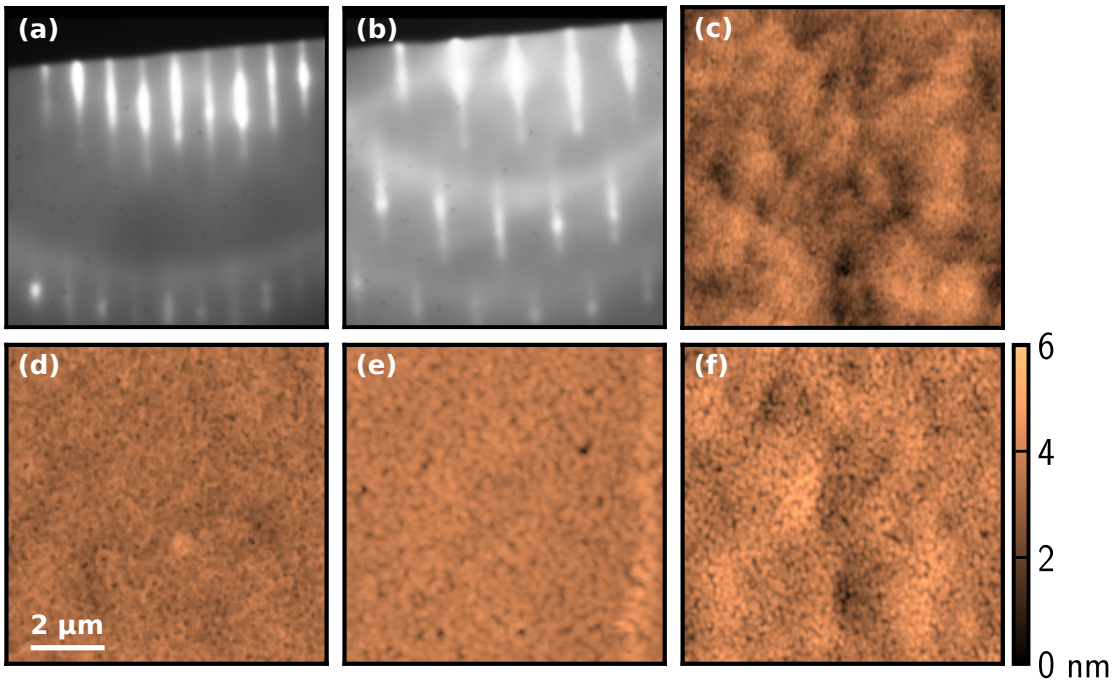

Figure 3.3: (a) and (b) RHEED from MnGe film after cooling to room temperature. Sharp streaks indicate a flat crystalline surface. (c)-(f) AFM micrographs for MnGe films of thickness (c) 11.6 nm (d) 29.4 nm, (e) 22.9 nm and (f) 18.4 nm. In each case, the RMS roughness is between 3 and 6 Å. The scale bar and height colourmap apply for all micrographs.

3.2 Optimal growth conditions

The B20 crystal structure was realized in films grown by co-deposition at elevated temperature, but with limited success. Figure 3.4 details XRD patterns from films which were annealed at increasing temperatures, each for 60 minutes. At 250 °C, single-phase MnGe formed, based on the absence of any peaks other than the MnGe(111) peak near $2\theta = 32.5°$. The nominal as-deposited thickness of the film was less than 20 nm, meaning that its MnGe(111) peak will resemble the peak shown in Figure 2.4. The lack of distinct Kiessig fringes indicates that the MnGe layer has large roughness. The shoulder on the right side of the peak may be attributed to a small amount of CrSi, or MnSi.

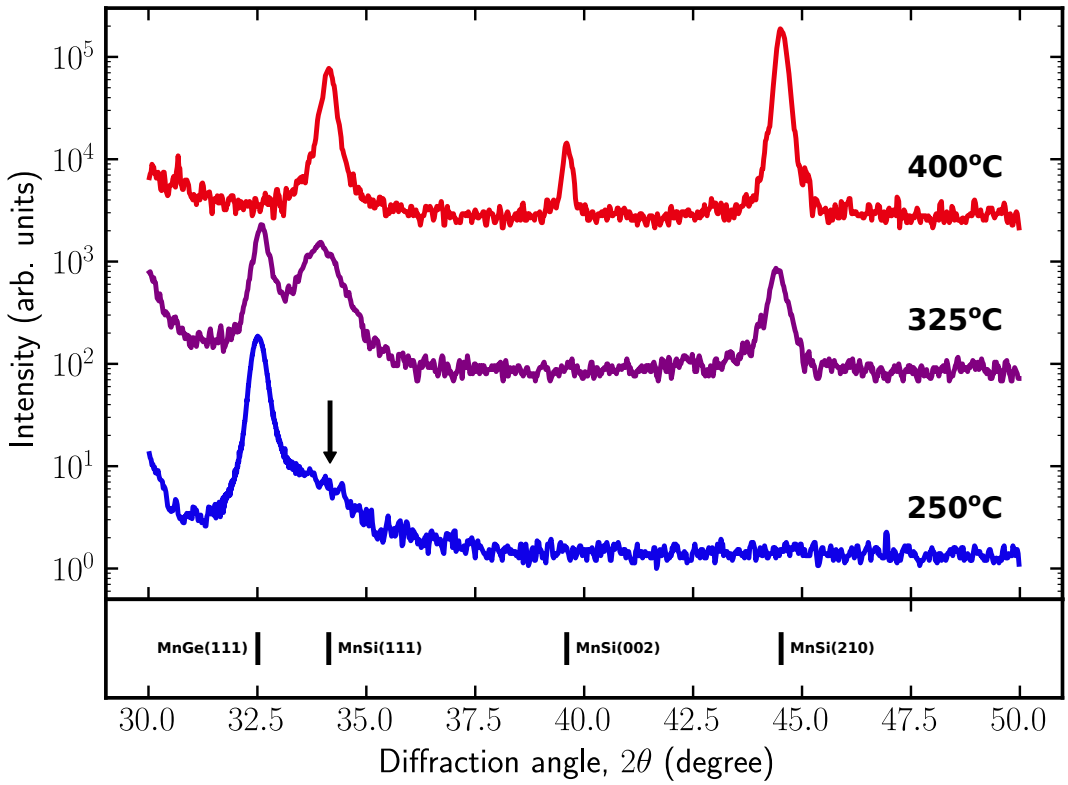

Figure 3.4: XRD of MnGe films co-deposited at elevated temperature. At 250 °C, the film is predominantly (111) oriented MnGe, except for an additional shoulder on the MnGe(111) peak indicated by the arrow, which my be due to either CrSi or MnSi. As the growth temperature increases, textured MnSi forms due to the diffusion of Mn into the substrate.

At annealing temperatures of 325 °C and 400 °C, the intensity of the MnGe(111) peak diminishes and gives way to multiple peaks corresponding to different orientations of MnSi. At 400 °C, the MnGe(111) peak is completely extinguished. This can be explained by the diffusion of Mn into the Si substrate with increasing temperature. Above a critical temperature between 325 and 400 °C, the growth of MnGe is inhibited by the reaction of deposited Mn with the substrate to primarily form MnSi, or possibly $MnSi_{1-x}Ge_x$. In the growth of MnSi thin films, common impurity phases include Mn_5Si_3 and $MnSi_{1.7}$ and these were not observed.

The composition was also varied for a small number of samples. For these samples, the Mn and Ge were co-deposited at 100 °C and the film was crystallized under periodic RHEED observation at 250 °C. In films co-deposited with excess Ge, single-phase MnGe formed with large roughness. Additionally, the Ge(111) peak near $2\theta = 27°$ indicates that epitaxial Ge(111) is in coexistence with the MnGe. This is consistent with the lack of equilibrium Ge-rich phases on the binary phase diagram [35]. In samples with excess Mn, the impurity phase Mn_5Ge_3 formed. With increasing Mn concentration, more Mn_5Ge_3 is formed compared to MnGe. When deposited atop the CrSi template, this phase was observed up to the deposited Mn:Ge stoichiometry of 5:1, with no other Mn-rich germanides definitively identified.

Hexagonal $Mn_5Ge_3(0001)$ on CrSi(111) has a lattice misfit of less than 10%. The formation of only MnGe and Mn_5Ge_3 further illustrate the ability of the CrSi layer to stabilize expitaxial phases. Mn-rich samples were grown with a Ge capping layer. As evidenced by XRD patterns in Figure 3.5, *ex-situ* annealing at 250 °C for 60 minutes allowed the Mn_5Ge_3 to react with the excess Ge, resulting in the conversion of nearly all Mn_5Ge_3 into MnGe for stoichiometries sufficiently close to $Mn_{1.0}Ge_{1.0}$.

So far it has been shown that the formation of B20 MnGe is made possible by the 2 QL CrSi template. For temperatures above 250 °C and Mn:Ge stoichiometries above 1:1, the formation of single-phase MnGe is inhibited by Mn_5Ge_3 impurities. A sample was grown to test whether the Mn_5Ge_3 impurity phase could be removed by annealing without excess Ge. In Figure 3.6, it can be seen that this results in a mixture of MnGe, MnSi and Mn_5Ge_3. This is somewhat expected based on the data in Figures 3.4 and 3.5. Surprisingly, the epitaxy of the Mn_5Ge_3 is significantly improved, with Kiessig fringes fit to Equation 2.12 yielding a Mn_5Ge_3 thickness of

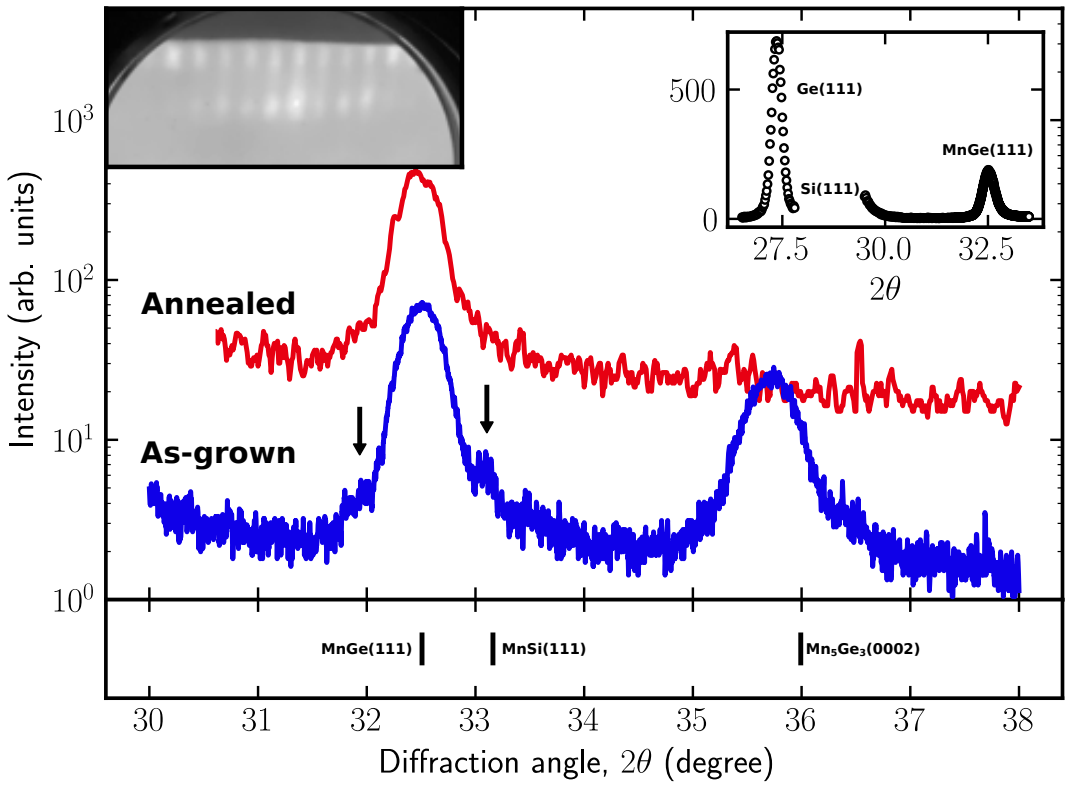

Figure 3.5: XRD of non-stoichiometric MnGe films. The blue data represents an as-grown Mn-rich film which exhibits both B20 MnGe and Mn_5Ge_3. The arrows indicate the location of the first-order Kiessig fringes flanking the MnGe(111) peak. Upon *ex-situ* annealing in excess Ge at 250 °C for 60 minutes, the red data is obtained, where all the Mn_5Ge_3 has been converted to MnGe, at the cost of increased roughness. The right inset shows the Ge(111) peak observed in films grown with excess Ge. The left inset shows the RHEED pattern typical of a film contaminated with Mn_5Ge_3.

12.2 nm. Roughness between 1 nm and 2 nm could be reliablly fit to the data.

Mn and Ge were co-deposited at 100 °C, followed by a 60 minute anneal at 250 °C where RHEED revealed a pattern typical of Mn_5Ge_3 (shown in Figure 3.5). After second stage annealing to 325 °C, a pattern resembling those in Figure 3.3 emerged. While the RHEED improved significantly, possibly indicating the Mn_5Ge_3 had been converted to MnGe, XRD revealed that the film was actually mixed-phase.

These experiments illustrate that the substrate temperature needs to be maintained below 250 °C after the deposition of Mn and Ge, and that deviations from the stoichiometric ratio will result in the nucleation of secondary phases.

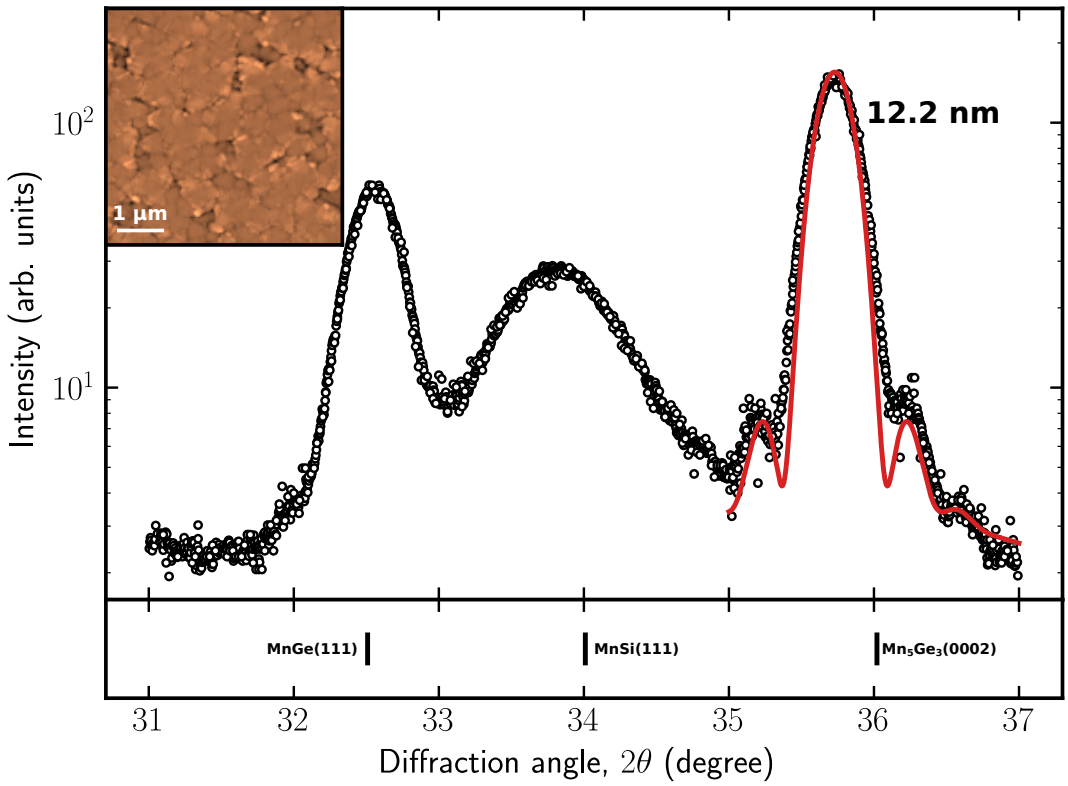

Figure 3.6: XRD of Mn-rich MnGe film after two-stage annealing of 60 minutes at 250 °C, then 325 °C. As expected, Mn diffusion into the substrate leads to a MnSi(111) peak. The Mn_5Ge_3(0002) peak has sharp Kiessig fringes which are fit by the red line using Equation 2.12. The inset shows the surface of a film predominantly comprised of Mn_5Ge_3 as revealed by AFM. The surface of the film is very flat and continuous, consistent with the Kiessig fringes commonly observed on Mn_5Ge_3(0002) peaks.

3.3 Determination of film thickness and quality

The procedure detailed in Section 3.1 allowed for epitaxial MnGe films to be grown for thicknesses between 2.5 nm and 41 nm. To prevent the formation of MnSi, the annealing temperature was kept at or below 250 °C. To prevent the formation of segregated Ge or Mn_5Ge_3, the deposition rates were re-calibrated using the trilayer in Figure 2.7. It was found during calibrations that the flux of Mn as determined by the ionization gauge (see Figure 2.1) was not linear in pressure. A different proportionality constant between the pressure and Mn deposition rate is needed for each deposition rate. The nominal Mn and Ge deposition rates of 2.97 Å min^{-1} and 5.46 Å min^{-1}

respectively, were used for every sample to ensure consistency among samples and the calibration.

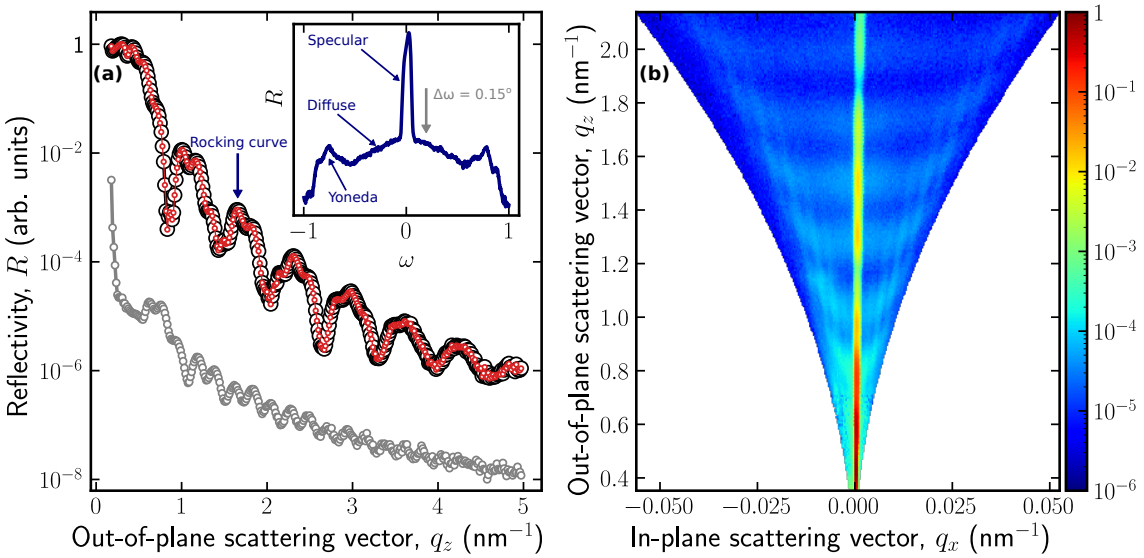

Figure 3.7: (a) XRR for the MnGe film with thickness of 9.1 nm (black circles), along with diffuse reflectivity (grey circles). The inset shows reflectivity from a rocking curve around $2\theta = 2.3°$ (indicated by the blue arrow). The peaks in this rocking curve near $\omega = \pm 1$ are the Yoneda peaks, arising from anomalous surface reflectivity. The diffuse reflectance was measured using an offset of $\Delta\omega = 0.15°$, indicated by the grey arrow. The specular reflectivity, the difference of the measured and diffuse reflectivity, is given by the red circles. (b) Small-angle mapping of reciprocal space for a 6.1 nm thick film. The Kiessig oscillations can be seen in the intense band at $q_x = 0$. The off-specular reflectivity is much smaller than the specular reflectivity. The region outside the intensity cone is not accessible by the geometry of the diffractometer.

In a real sample, interfacial roughness and defects produce diffuse scattering, which is measured by the detector during the measurement. Figure 3.7 depicts XRR measurements for the MnGe film with a thickness of 9.1 nm. The Si cap was 20 nm with 2.2 nm of SiO_2 at surface. The diffuse reflectivity was measured by offsetting the sample by $\Delta\omega = 0.15°$. When the diffuse component to the measured reflectivity is subtracted, there is little change to the the data. Inspection of the diffuse reflectance shows that it is mostly comprised of short-period oscillations which correspond to a large ($\sim$ 20 nm) structure in real space: the Si cap, not the MnGe film. It also can be seen from the reciprocal space map for the 6.1 nm film that the off-specular components are small across a wide range of scattering vectors. This behaviour was

observed in all samples. In the subsequent fits of XRR data, the diffuse component to the specular intensity is neglected.

Representative XRR fits, along with the calculated SLD are given in Figure 3.8. Each fit includes the Si substrate, CrSi template, MnGe film, Si capping layer, and SiO_2. For each layer, the bulk electron density was used. The density of MnGe was only refined in cases necessary to achieve a good fit. In these cases, the need for a refinement in density was obvious because the observed and calculated critical angle (wavevector) did not match. The density was never refined more than a few percent.

The refined roughness of the substrate was in agreement with AFM discussed in Section 3.1, typically ranging between 2 and 8 Å. The CrSi template is difficult to resolve with XRR as its small extent in real space corresponds to extremely broad Kiessig oscillations in q-space. The available X-ray flux from the diffractometer limits the maximum scattering vector to approximately $5\,\mathrm{nm}^{-1}$. This only allows the first order Kiessig fringe to be observed. It was found, however, that the addition of CrSi into the model was necessary to achieve a satisfactory fit. The roughness of this layer was constrained to be less than 1 Å due to its small thickness.

The refined MnGe thicknesses were within a few percent of the nominal thickness calculated from the deposition of Mn and Ge. The roughnesses were also consistent with AFM. Many samples exhibited roughness below 5 Å. In each sample measured, the thickness of the cap matched the thickness recorded by the crystal oscillator to within a few Å. Each fit required a native oxide of either SiO_2 or GeO_2, depending on the capping layer. The thickness of this overlayer was found to consistently lie between 1.6 and 2.8 nm, which is in agreement with previously reported thicknesses determined by XPS.

The models determined by XRR were also tested by systematic fitting of the MnGe(111) XRD peaks. A fit of XRR data is not necessarily unique, so agreement between multiple fitting procedures will add additional confidence to the model. The MnGe(111) peaks were observed near the bulk position of $2\theta = 32.3°$. The mean position was $2\theta = 32.5°$, indicating that (111) plane spacing is smaller than bulk. This peak is also in the vicinity of the Si(111) peak, which has immense intensity compared to the film peaks. The tail from the Si(111) peak had to be subtracted to fit the Kiessig fringes of the MnGe(111) peak.

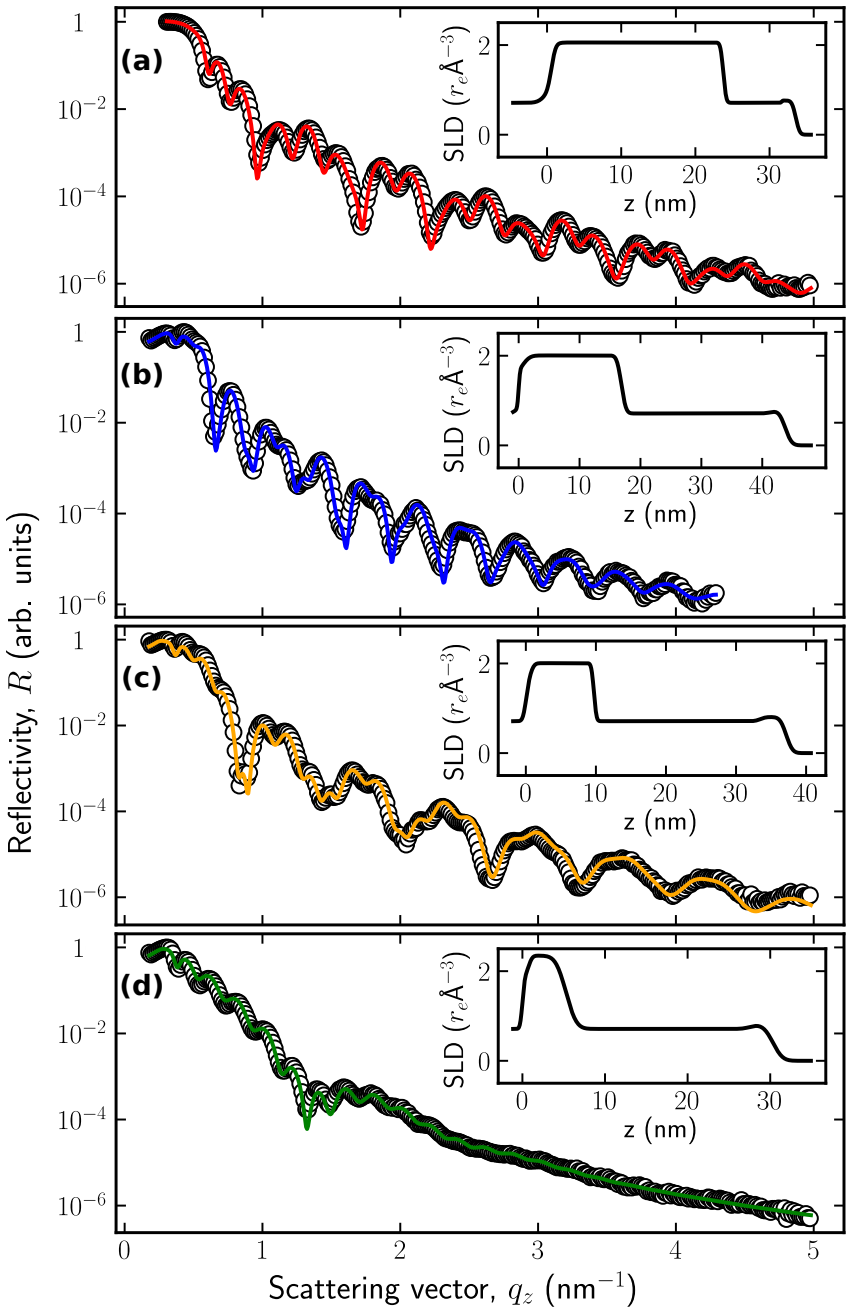

Figure 3.8: Representative XRR fits of MnGe films. Thicknesses were found to be (a) 22.9 nm, (b) 16.4 nm, (c) 9.1 nm, and (d) 4.6 nm. The inset in each gives the SLD. Each fit includes the Si substrate, CrSi template, MnGe film, Si cap, and SiO_2. For (a)-(c) the Kiessig oscillations are clearly visible to high q, indicating low roughness. In (d), the short period oscillatons correspond to the Si cap and the long period signal is from the MnGe. This sample has a larger roughness, indicated by the extinction of oscillations above $q = 2\,\text{nm}^{-1}$.

The natural lineshape of the Si peak is Lorentzian, which must be convolved with Gaussian instrumental broadening. The result is a Voigt function, which has no closed form expression and is often approximated as a pseudo Voigt function, which is just the product of the two profiles. The lineshape of the Si(111) subsrate peaks was found to be well described by Lorentzian. The peak is approximated to be Lorentzian, of the form

$$L(2\theta;\gamma) = \frac{\gamma}{\pi(\gamma^2 + (2\theta - 2\theta_0)^2)}\,, \tag{3.1}$$

where γ is the width and $2\theta_0$ is the peak centre. The intensity of the Si(111) peak is enough to saturate the detector on the diffractometer. An attenuator must be used if the Si(111) peak is to be measured, but the intensity of the MnGe(111) peak is too small to be seen with the attenuator. The attenuated and unattenuated data could not be scaled in such a way that one Lorentzian fit could be applied to both regions simultaneously. To ensure an accurate subtraction of the background intensity, the Lorentzian profile of the Si(111) peak was approximated in the region where the attenuator was not necessary, $2\theta > 29°$.

Equation 3.1 may be expanded using the geometric series, yielding a function B which approximates the background of the Si(111) peak asymptotically far away. A blank Si wafer was measured with XRD and the background was fit to:

$$B(2\theta) = \frac{b_2}{(2\theta)^2} - \frac{b_4}{(2\theta)^4} + \frac{b_6}{(2\theta)^6} - \frac{b_8}{(2\theta)^8} + \frac{b_{10}}{(2\theta)^{10}}\,. \tag{3.2}$$

This function was determined phenomenologically by adding terms to the series until the data was fit in the range $29° \leq 2\theta \leq 38°$ with deviations less than 10^{-3}. The refined parameters were:

$$b_2 = -5.47\,, \quad b_4 = -695.370\,, \quad b_6 = -6698.685\,, \quad b_8 = -37170.082\,, \quad b_{10} = 247.152\,.$$

The background function was then appropriately scaled to match the background observed on each MnGe(111) peak, and subtracted. The parameters b_i remained constant, whereas the scaling parameters where chosen to such that the first order Kiessig fringes on either side of the main MnGe peak had the same intensity.

Representative XRD fits are given in Figure 3.9 and the background subtraction is shown in the inset. Least squares fitting was attempted but it was found that fitting by eye was able to produce better fits. The thicknesses determined by the separation

of the Kiessig fringes were in excellent agreement with XRR, differing by less than 1 nm for all samples. The amplitude of the fringes was captured in general, but the observed fringes are much broader than are captured in the model (Equation 2.12). This broadening explains why the intensity minima are less sharp than in the fit.

To further confirm the B20 structure, reciprocal space maps were performed on select films. The MnGe (112), (221) and (331) reflections were observed at their expected positions. The epitaxial relationship of MnGe(111) on Si(111) (same as in Figure 2.6) was also confirmed, by comparing the observed peaks from the substrate and film. Peaks were found corresponding to both chiralities of MnGe, with an approximately equal intensity ratio. This suggests that the MnGe films nucleate in domains with equal amounts of left and right handedness, as has been observed with films of other B20's. Though there may be many structures with a similar out-of-plane spacing to MnGe, only the B20 structure will account for every observed peak.

3.4 Measurement of the film strain

The out-of plane lattice parameter of the MnGe films was probed using XRD. For each sample, the positions of the Si(111), MnGe(111), Si(333) and MnGe(333) peaks was recorded. The substrate peaks can be used as internal references which are independent of the alignment offset $\Delta\omega$. The separation between (333) peaks is much larger than the (111) peaks, so no background subtraction is required. The substrate peaks were fit with a doublet Lorentzian (Equation 3.1) and the film peaks were fit according to Equation 2.12. The relative location of the film peaks to the subtrate were recorded and used to find the plane spacing. This was transformed to an effective cubic lattice parameter.

The out-of-plane lattice parameter versus film thickness is plotted in Figure 3.10. The error bars are the difference between the values determined from using the (111) and (333) peaks. The large uncertainty for small thicknesses originates from both the small extent of the XRD peaks, especially MnGe(333), as well as the background subtraction on MnGe(111). Also given is the behaviour from MnSi thin films from Reference [62].

The behaviour in Figure 3.10 reveals that the out-of-plane lattice parameter is smaller than bulk. This is unexpected based on the epitaxial relationship of MnGe

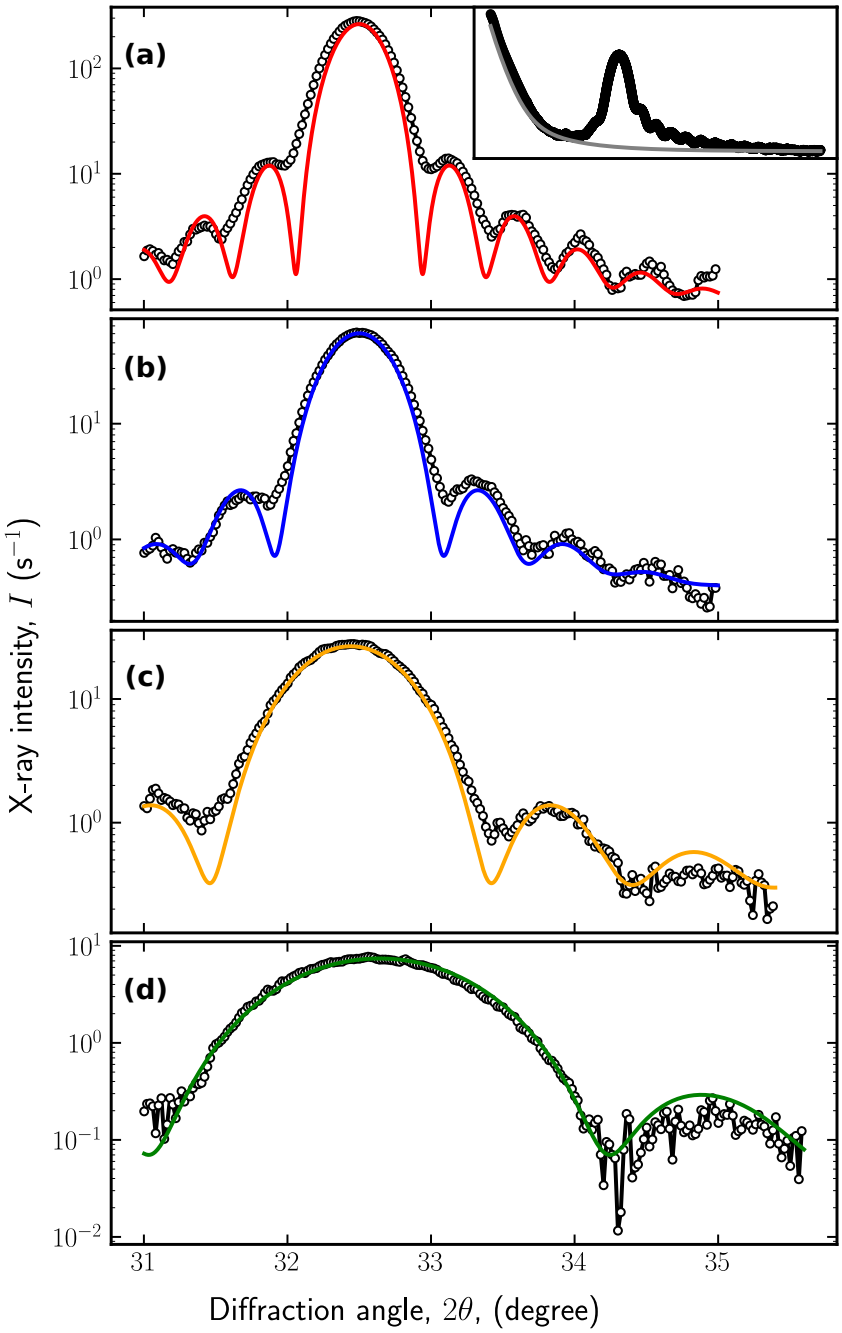

Figure 3.9: Representative XRD fits of MnGe films. Thicknesses were found to agree with XRR values of (a) 20.5 nm, (b) 16.4 nm, (c) 9.1 nm, and (d) 4.6 nm to within less than 1 nm. The inset in (a) shows the background fit in grey for the 22.9 nm sample. The amplitude of the Kiessig fringes is captured in general by the fit, but the observed fringes are broader than can be captured in the model.

on Si(111), which indicates that pseudomorphic MnGe(111) should be under an in-plane compressive strain. Assuming the Poisson ratio of MnGe behaves similarly to other B20 compounds, this means that the out-of-plane lattice parameter should be larger in thin films than in bulk. The strain of epitaxial MnGe films was measured using TEM in the supplemental of Reference [34], where in-plane strain was found to be tensile for the three films studied. MnSi thin films are expected to be under an in-plane tensile strain and that is reflected in a decrease in the out-of-plane lattice parameter in Figure 3.10. A similar unexpected behaviour was observed for MnSi films on SiC(0001). While MnSi is supposed to be under compression, it was found that the high temperatures necessary to stabilize the B20 structure resulted a dewetting of the film, and produced a thermal residual in-plane tensile strain rather than the compressive strain expected [75]. A similar scenario may be occuring here for MnGe on Si(111).

The reciprocal space map of the MnGe(111) peak for the 29.4 nm sample in Figure 3.11 shows a large extent in q_z due to finite size broadening. The peak also has a relatively large extent in q_x; approximately $1\,\mathrm{nm}^{-1}$. This broadening is not accompanied by broadening in the Si(531) peak ($0.08\,\mathrm{nm}^{-1}$ width), or the XRR rocking curves in Figure 3.10 which were consistently close to the diffractometer resolution of $0.03\,\mathrm{nm}^{-1}$ (FWHM 0.02° in ω). The lack of broadening in the substrate and XRR rocking curves indicates that there is no bending of the substrate detectable by X-rays and the broadening on the MnGe(111) peak is due to the film. Since the FWHM of the XRR rocking curve is low, this means that the undulation of the crystallographic MnGe planes is larger than undulations in the surface morphology. The broadening in q_x may indicate that there is mosaicity in the film. A mosaic film is comprised of many domains, each with their normal slightly misaligned with respect to the surface of the substrate. The island structure of the films is displayed in Figure 3.3 and the boundary between these domains is well defined. The coalescing of these island as the B20 structure nucleates may cause a buckling or small corrugation in the film leading into an increase in diffuse scattering in q_x.

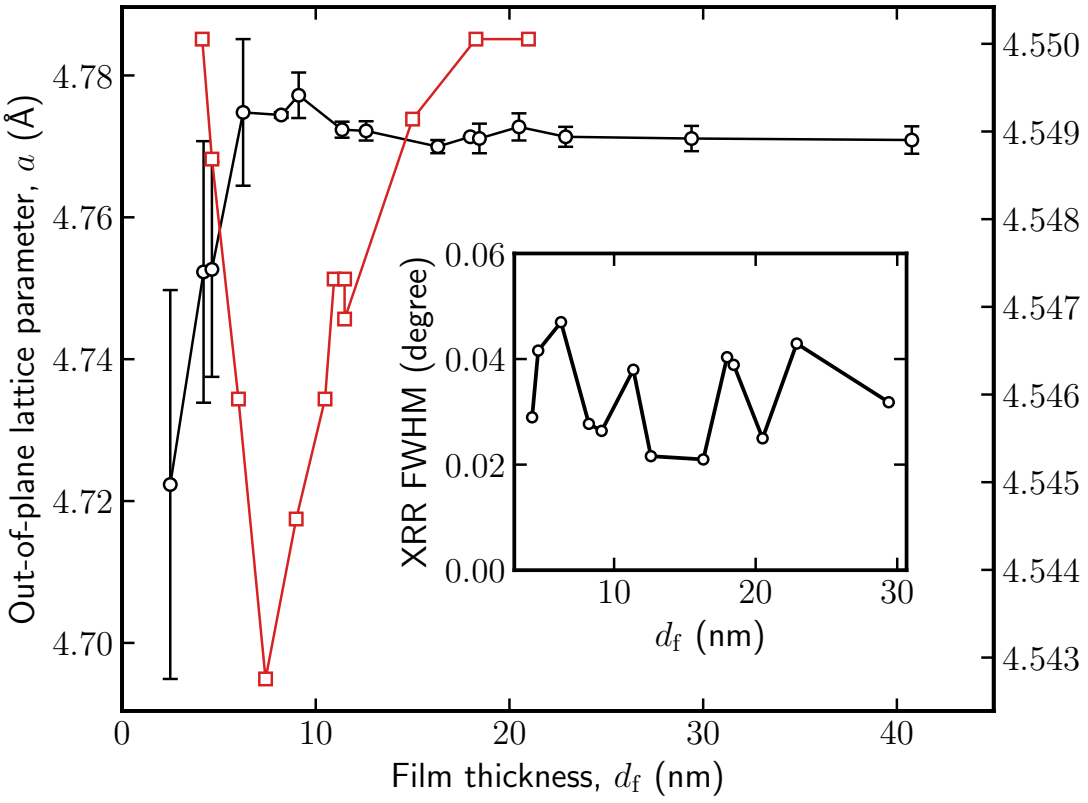

Figure 3.10: Out-of-plane strain of MnGe films versus thickness. The black circles are the out-of-plane lattice parameters, as determined by XRD. The error bars represent the difference of calculated lattice parameter between the (111) and (333) peak, and the value is the average. The red squares are data for MnSi thin films in Reference [62]. The inset shows the FWHM of the XRR rocking curve taken below the critical angle θ_c.

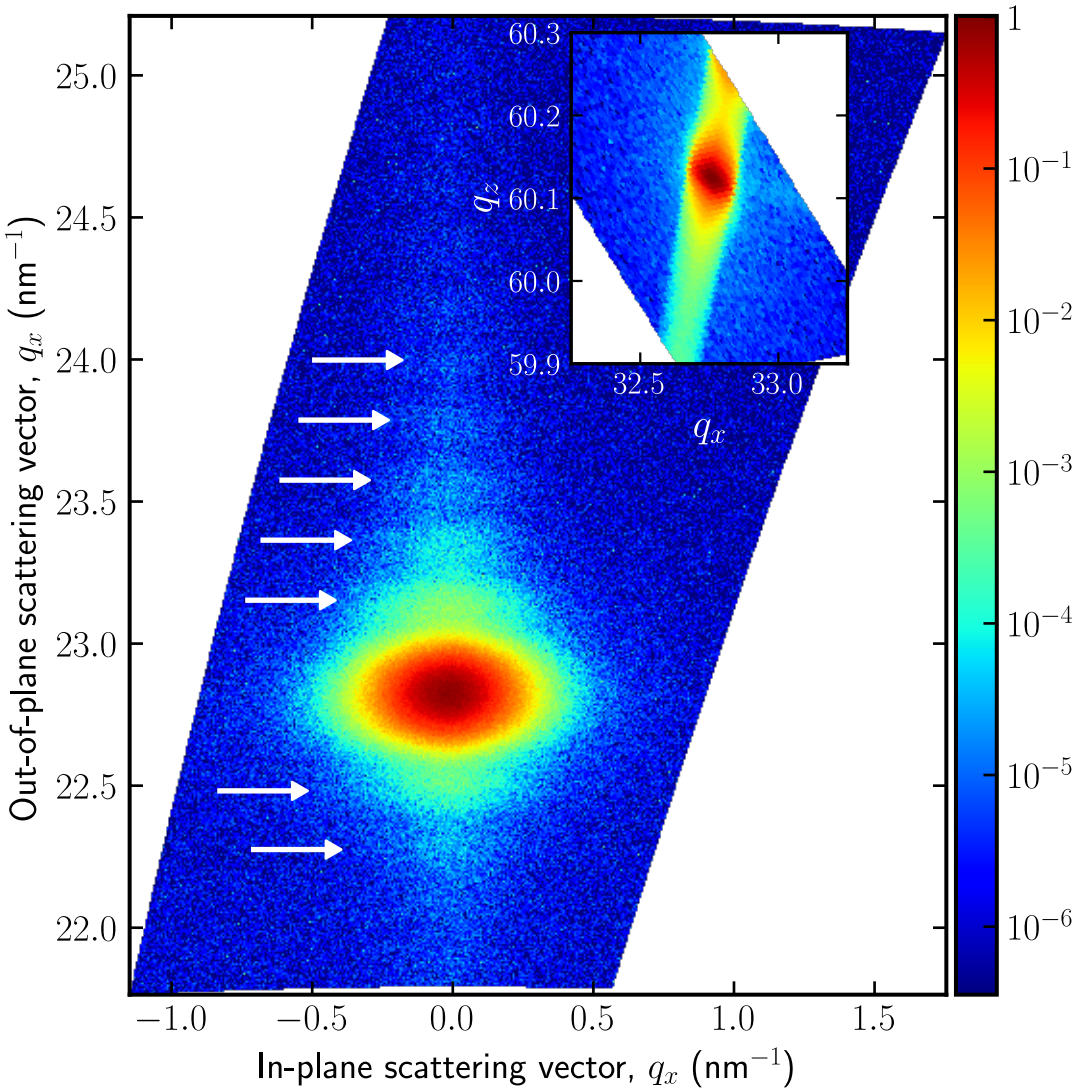

Figure 3.11: Reciprocal space mapping of the MnGe(111) peak for the 29.4 nm sample. The colour map is the normalized X-ray intensity. Extent in q_z is caused by finite size broadening and Kiessig fringes are denoted by the arrows. The extent in q_x is surmised to be due to the island structure of the film. The inset shows a map of the Si(531) peak, which only exhibits broadening in q_z.

Chapter 4

Magnetic characterization with H in-plane

This chapter presents the first study of the magnetism of MnGe thin films with in-plane fields. It was found that a large first-order-like jump in the magnetization signaled the transition from a helicoid phase to a twisted ferromagnet. Analysis of the temperature dependence of the magnetization provides evidence for thermal induced unwinding of the helix. The chapter culminates in a magnetic phase diagram of MnGe thin films for in-plane fields.

4.1 SQUID magnetometry

SQUID magnetometry measurements were performed on select samples. Three samples with thickness 22.9 nm, 16.4 nm and 9.1 nm and were chosen to allow for the study of the thickness dependence of the magnetic properties. These samples also had XRR fits with low residuals and low film roughness which are featured in Figure 3.8 (a)-(c).

The magnetization was measured in two types of measurements: at constant temperature ($M-H$) and constant field ($M-T$). When a phase change occurs, there are features in the order parameter (in this case, the magnetization) and its derivatives. These features are used to identify boundaries between magnetic phases. Isothermal $M-H$ curves are sensitive to phase that are mostly temperature-dependent (horizontal on a magnetic phase diagram), and $M-T$ curves are sensitive to field-dependent transitions (vertical on a magnetic phase diagram). These scans are complementary and allow the identification of any magnetic phase transition.

Firstly, representative $M-H$ curves are presented. The sample was field cooled at 7 T to the desired temperature. The moment was measured as the applied field was cycled to -7 T, then back to 7 T, after which the temperature was changed and the loop was repeated. Figure 4.1 depicts $M-H$ loops for the 22.9 nm sample. The curves are all qualitatively similar across the three samples. At low fields, there is a region where the magnetization increases linearly. This is followed by a sharp increase in

the magnetization, until it flattens off to its saturation value. At lower temperatures, the magnetization does not completely reach its saturation value at 7 T. The curves also exhibit hysteresis which vanishes above approximately 50 K, likely due in part to the fact that the film is not completely saturating.

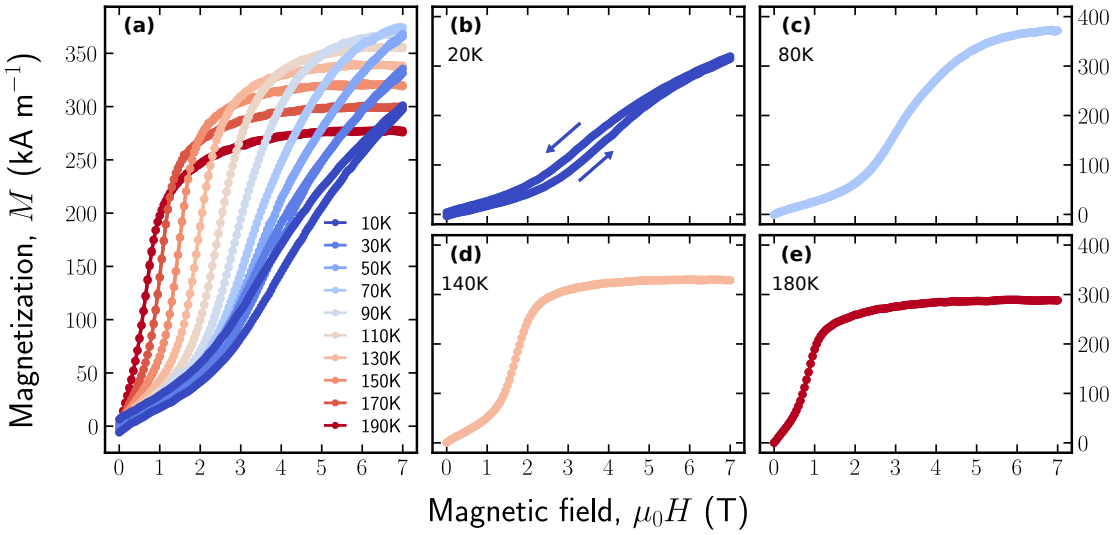

Figure 4.1: (a) Representative $M - H$ loops for the 22.9 nm sample across the temperature range measured. (b)-(e) Selected curves to show the temperature evolution. Significant hysteresis is present for temperatures less than 50 K. The arrows in (b) indicate whether the field is increasing or decreasing. Above 50 K, the two branches lie on top of each other.

The one remarkable feature in all $M - H$ curves is the dramatic increase in the magnetization at intermediate fields. To align with the convention used for MnSi thin films, this first-order-like jump in the magnetization is said to occur at a field H_α. This is srongly indicitive of a phase transition. To characterize this transition, it is instructive to plot the static magnetic susceptibility by differentiating the magnetization as a function of applied field. Figure 4.2 depicts a series of curves detailing the evolution of the susceptibility with temperature. The large peak in the susceptibility marks the location of a phase transition at H_α. The value of H_α at each temperature was extracted by fitting the peak with a Gaussian and recording the field of maximum susceptibility.

It is useful to compare the observed behaviour to previous work on MnSi thin films, as well as theoretical calculations. It was found in MnSi that for in-plane fields,

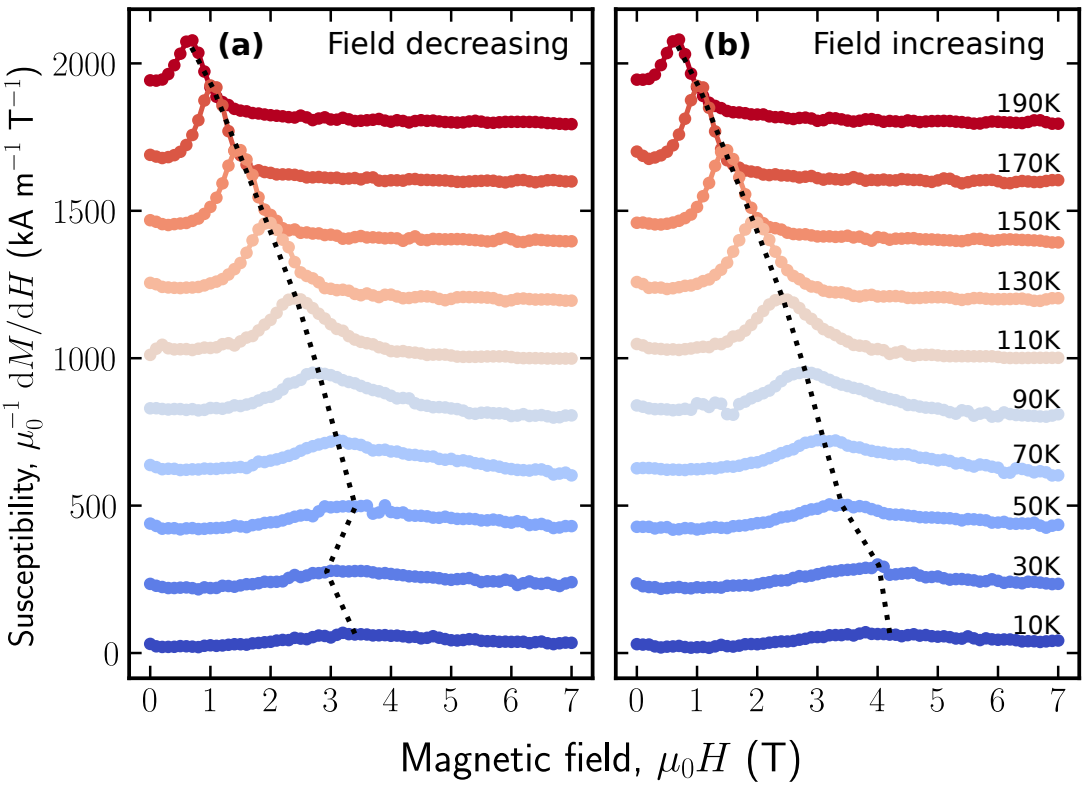

Figure 4.2: Magnetic susceptibility versus (a) decreasing fields and (b) increasing fields for the 22.9 nm sample. The susceptibility was calculated by taking the derivative of the $M - H$ curves for each branch separately. The dotted line is a guide to the eye which tracks the position of the transition at H_α.

ground state is a helical state with propagation vector **Q** that points out of plane. This is referred to as a Q_z state. At 5 K, PNR studies showed that the Q_z helicoid persists until it saturates [76, 77]. Above approximately 10 K, the helicoid transitions into a broadly stable skyrmion lattice phase [75, 77] above a field between 200 mT and 500 mT, which is evidenced by a peak in the susceptibility. Upon exiting this phase, the in-plane magnetization increases drastically as the film transitions into a mostly saturated structure. It was found that instead of fully saturating at high fields, the sample enters a twisted ferromagnetic state. In the preceeding discussion, when saturation is mentioned, it is assumed to be the twisted ferromagnetic state.

In MnSi, peaks in the susceptibility are observed upon entering and exiting the

skyrmion phase. They are also observed during the discrete unwinding of the helicoid [23] and upon entering the twisted ferromagentic state. In Figure 4.2, only one peak is seen in $\mathrm{d}M/\mathrm{d}H$. This is similar to MnSi at 5 K where only the helicoid state is observed.

Micromagnetic simulations were performed by C. D. Rudderham to help understand the origin of the single peak in the susceptibility. The same framework as in Reference [31] was used. The result of the calculation is reproduced in this thesis with permission. Three phases were considered: a one-turn helicoid, a two turn helicoid, and the twisted ferromagnetic state. The film thickness was $2.0\,L_{\mathrm{D}}$. The magnetization of these phases versus field is given in Figure 4.3. The energy of each phase was also calculated. To model the behaviour at finite temperature, the magnetization was given a Boltzmann weight according to its energy and the average in-plane magnetization of the sample is given in the figure. The thermal energy in the Boltzmann weight was chosen empirically.

The calculated $M - H$ curve qualitatively reproduces those in Figure 4.1. There is a flat region, followed by a sharp increase as the twisted ferromagnetic state is energetically preferred. This is reflected as the sharp peak in the susceptibility, much like those in Figure 4.2. Also captured in this calculation is the small feature in the susceptibility (seen in Reference [28] for MnSi thin films) where there the helicoid winding number changes. Such a feature is not observed in the $M - H$ data presented for MnGe thin films and it is unclear why this is the case. Nonetheless, this simulation implies, along with comparison to MnSi, that MnGe transitions from a helicoid directly into a twisted ferromagnetic state. There is no evidence for an in-plane skyrmion phase in the magnetometry.

The field at which the sample enters the twisted ferromagnetic phase was not reliably determinable by a minimum in $\mathrm{d}^2M/\mathrm{d}H^2$. Instead, this field was estimated to be the location of the knee in the $M-H$ loop, H_{k_2}. The inflection point corresponding to the field H_α was linearly extrapolated to the point where it reached the saturation magnetization (see Figure 4.4). This method allows for a consistent identification of H_{k_2} despite the broad, rounded behaviour of M as the film saturates. There is also a knee in the curve where the sample exits the linear region. This was determined in a similar way and is labelled as H_{k_1}. The last feature occured exclusively at low

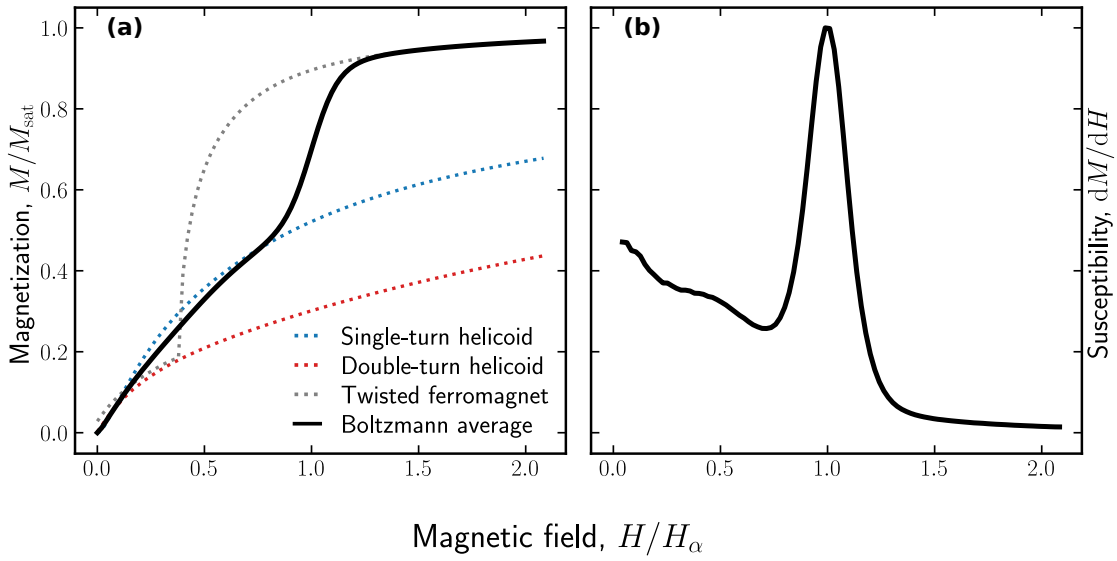

Figure 4.3: Micromagnetic simulation of the helicoid to twisted ferromagnet transition. The model contains a one-turn helicoid, a two turn helicoid, and the twisted ferromagnetic state. (a) The magnetization of each phase versus field, and the thermal obtained by weighting the energy of each phase by a Boltzmann factor. The temperature was chosen empirically. (b) The susceptibility versus applied field, which shows a large peak where the film transitions from a helicoid to the twisted ferromagnet. A smaller feature in the susceptibility is seen when the film discretely changes from a two turn helicoid to a one turn helicoid, which washes out at higher temperatures. The data in this figure is courtesy of C. D. Rudderham.

temperatures. Above H_α, the susceptibility drops sharply. Below 100 K, there was a shoulder which broadened the peak. The location of the shoulder was determined qualitatively and is labelled as $H_{\rm s}$.

The magnetization $M_{\rm sat}$ in the saturated (twisted ferromagnetic) state was recorded for the appropriate temperatures (where saturation was reached) and are shown in Figure 4.5. The value decreases monotonocally with temperature. At 70 K, this was 374 kA m^{-1}, 368 kA m^{-1} and 351 kA m^{-1} for the 22.9 nm, 9.1 nm and 16.4 nm samples, respectively. These magnetizations were converted into the moment per Mn atom after scaling by the bulk number density of Mn atoms. At 70 K, the measured moment of approximately 1 $\mu_{\rm B}$ per Mn atom is in rough agreement to the value of 1.4 $\mu_{\rm B}$ per Mn atom at 100 K reported for bulk[17]. For the 160 nm film in Reference [34], this was reported to be 1 $\mu_{\rm B}$ per Mn atom at 100 K, in excellent agreement with the value reported here. The in-plane remanent magnetization of the MnGe films was found

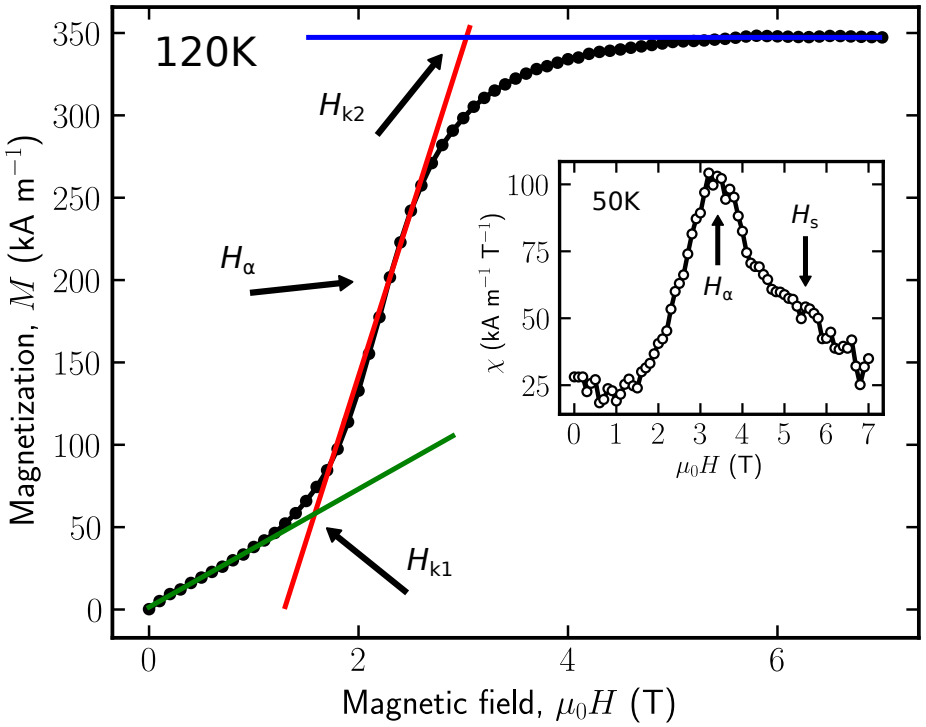

Figure 4.4: Determination of fields H_{k_1} and H_{k_2} in $M - H$ curves. The data shown is from the 22.9 nm sample, measured at a temperature of 120 K. The linear region and saturation magnetization are extrapolated to the line of maximum slope, fit at H_α. The inset shows the suscebility at 50 K. The transition H_α is easily identified by the peak. The location of the shoulder H_s is also indicated.

to be small, but finite. This is in contrast to the out-of-plane remanence which was below the detection limits of the SQUID magnetometer. A similar behaviour was observed in MnSi thin films and is consistent with a helix that points out of the plane.

In thin films which exhibit a Q_z helical phase, the remanent in-plane magnetization varies due to finite size effects. The magnetic moments lie in the plane and ferromagnetically align within each layer, spiraling around **Q** throughout the depth of the film. When the film thickness is an integer multiple of the helical pitch, the total magnetization will sum to zero. The in-plane magnetization should then vary

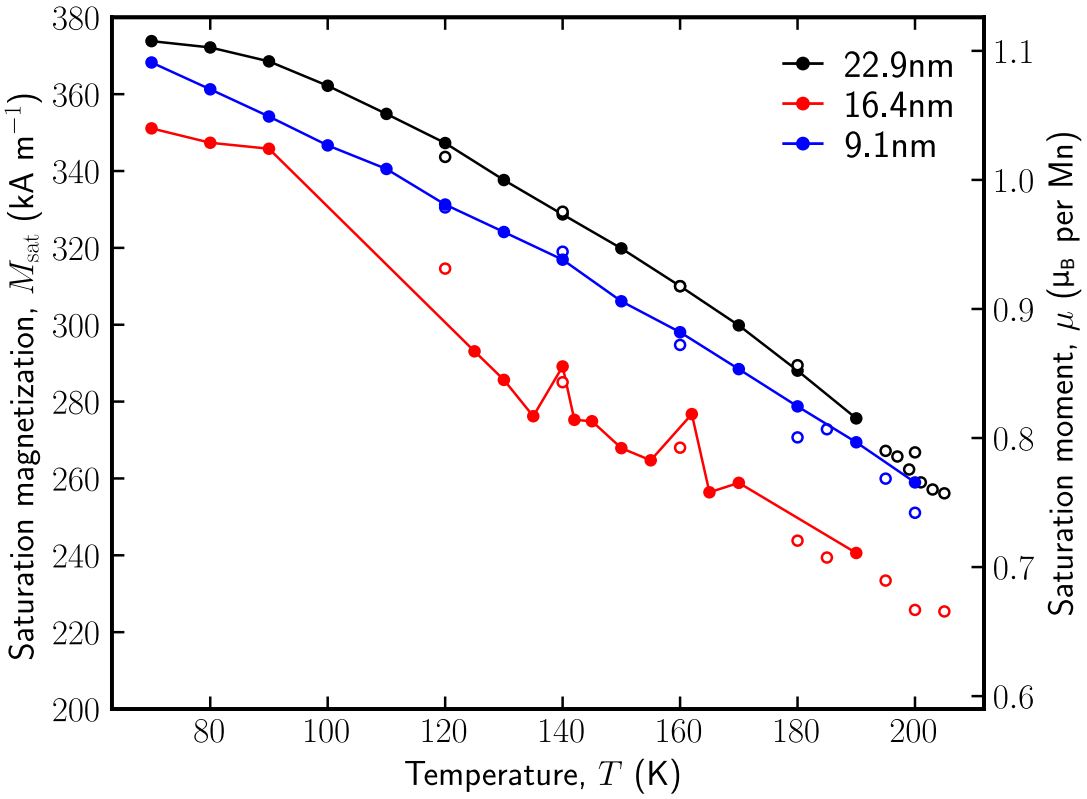

Figure 4.5: Temperature dependence of the saturation magnetization. Filled (unfilled) circles are the magnetization measured in-plane (out-of-plane). Values are given only for temperatures where the film saturated.

according to the film thickness as [62]:

$$\frac{M_{\mathrm{rem}}}{M_{\mathrm{sat}}} \propto \frac{1}{M_{\mathrm{sat}} d_{\mathrm{f}}} \int_{-d_{\mathrm{f}}/2}^{d_{\mathrm{f}}/2} \mathrm{d}z \, M_{\mathrm{sat}} \cos(Qz) = \frac{\sin(Qd_{\mathrm{f}}/2)}{Qd_{\mathrm{f}}/2} \,. \tag{4.1}$$

The ratio of the remanent magnetization to the magnetization at $\mu_0 H = 7\,\mathrm{T}$ is shown in Figure 4.6. The ratio is large at lower temperatures, since $M(7\,\mathrm{T})$ is less than the manetization of the twisted ferromagnetic phase for temperatures less than 100 K. The temperature at which the ratio drops is commensurate with the disappearance of hysteresis in the $M-T$ curves, and flattening of the magnetization after a well-defined H_{k_2}. For a helix which is elongating with temperature (Q decreases), Equation 4.1 predicts that the ratio will oscillate in temperature, with an amplitude which increases with increasing temperature; as the helix is composed of fewer turns and there is less cancellation of the net moment.

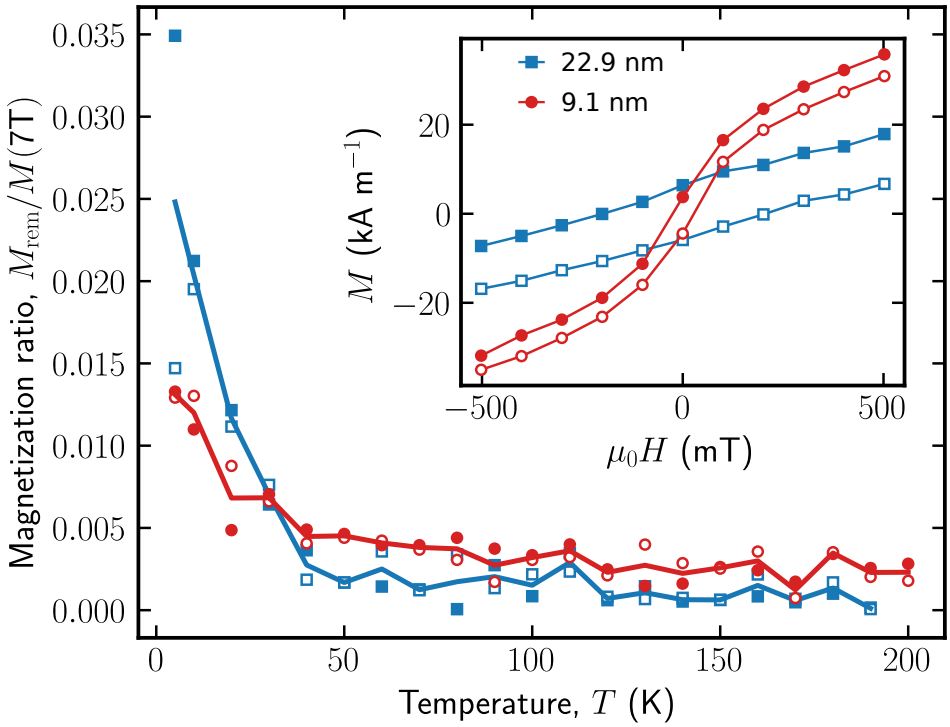

Figure 4.6: The ratio of the remanent magnetization to the magnetization at $\mu_0 H = 7\,\mathrm{T}$ for the 22.9 nm and 9.1 nm samples. The filled (unfilled) circles represent data obtained with decreasing (increasing) fields. The inset illustrates the remanent magnetization with $M - H$ loops obtained at $T = 10\,\mathrm{K}$.

This analysis is complicated by the measurement of the remanence as a function of temperature, which mostly gave an unreliable near-zero moment, where V_{RSO} was comprised of noise significantly offset from the established centre, likely due to small deformations and inhomogeneities in the straw. Inspection of V_{RSO} for each of these points confirmed that no moment could be confidently extracted. Despite multiple attempts at measuring M_{rem} versus temperature, only one successful curve was recorded (shown in the inset of Figure 4.8). This was obtained by field cooling the 22.9 nm sample at 10 mT before the field was lowered to zero and the magnetization was measured on warming. The unreliablility in determining M_{rem} versus T is in contrast to the remanent magnetization that is systematically observed on the $M - H$ curves, as seen in the inset of Figure 4.6.

This behaviour may be due to the relaxation of the helical domains into random orientations at remanence. In MnSi thin films, a glassy behaviour was observed [62]. The temperature dependence of the remanent magnetization was similar to that in Figure 4.8; a linear decrease which reaches zero at the expected ordering temperature. It was demonstrated that this was due in part to the presence of chiral domains. The interface between the domains gives rise to magnetic frustration due to competing windings of adjacent helices of opposite chirality. Given that the MnGe films are also expected to crystalize with equal numbers of left and right handed crystal orientations, the relaxation of the helices at the domain interfaces can explain why no magnetization is observed in the absence of a field.

To remove the cancellation effects of possible helical domains, $M - T$ measurements were also performed in static magnetic fields. To facilitate comparison between different applied fields, the static susceptibility is shown in Figure 4.7. The curves have a similar shape: the magnetization is relatively small for low temperatures, and it increases with increasing temperature until the film passes into the twisted ferromagnetic state at temperature which corresponds to H_α. This is different from the ferromagnetic-like behaviour of the $M - T$ curves for MnSi thin films. One reason for this could be the strength of the helical winding. In MnSi films, the helix appears to be relatively soft, as a small field will easily induce a magnetization. For MnGe, the magnetization is much more tightly coiled until the temperature is high enough to unwind the helix. This change in behaviour could be due to the increase in thermal fluctuations, or a temperature-induced elongation of the helical pitch, which drives the effective interaction toward that of MnSi. Due to the relatively long helical pitch of MnSi and FeGe, the angle between successive planes of spins is small ($\approx 7^\circ$ and 1°, respectively) and the system is ferromagnetic-like. The short pitch of MnGe means that this angle could be as large as 32°, and it is antiferromagnetic-like, which may explain why the susceptibility versus temperature is peaked near T_N like an antiferromagnet.

In these curves, there are also shoulders which appear at fields lower than 500 mT, occuring at temperatures labelled T_s. These features in the temperature-dependent susceptibility are not observed in the field-dependent susceptibility. The fact that these features appear only for low fields means that they may be caused by domains,

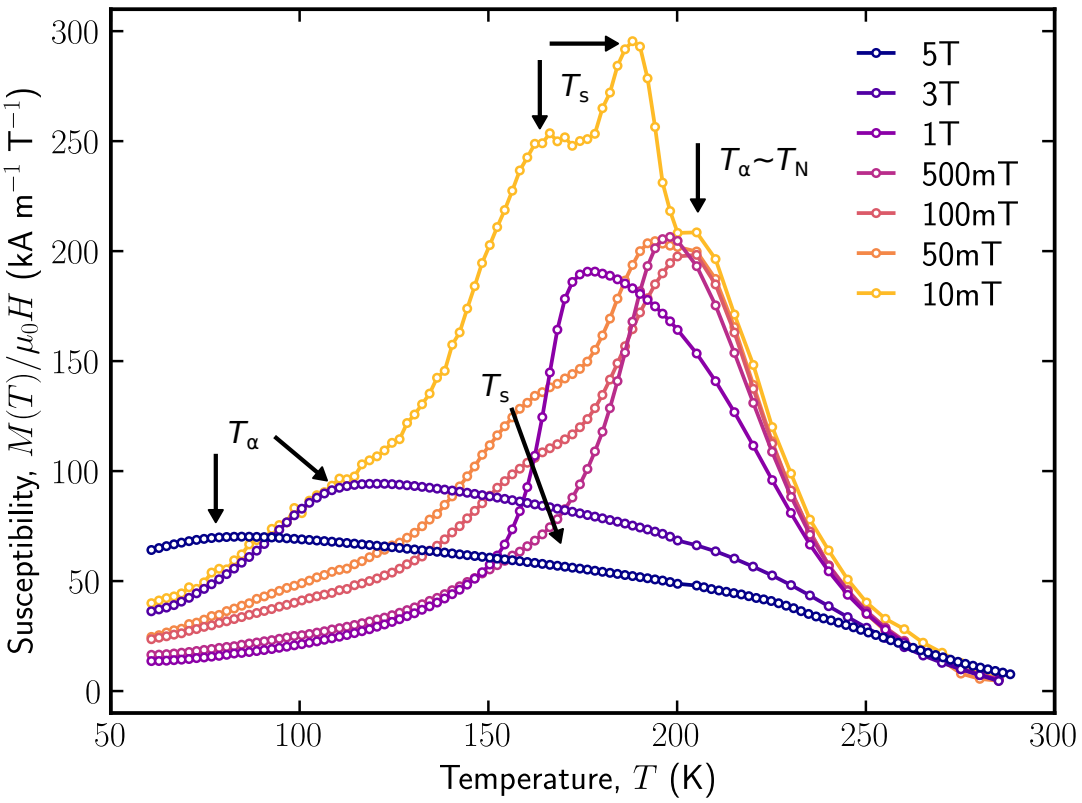

Figure 4.7: Field-normalized $M/\mu_0 H$-T curves for the 16.4 nm sample. The magnetization is small at low temperatures, which suggests that the helix of MnGe is rigid, which softens as temperature is increased. The best estimate of the ordering temperature comes from analysis of these curves for very low fields for H_α. The shoulders at fields below 500 mT are denoted by T_s.

some of which require more thermal energy to overcome their local environment and align to the relatively weak field.

These features could also possibly be attributed to the helical unwinding that was not observed in Figure 4.6. Based on Equation 4.1, a peak should be observed in the magnetization when Q changes by approximately $2\pi/d_f$. The data for $\mu_0 H = 10$ mT exhibits three such peaks. This means that the change in helical wavevector can be estimated as $\Delta Q = 3(2\pi/16.4\,\text{nm}) = 1.05\,\text{nm}^{-1}$. In Reference [34], it is interpreted from SANS data that Q elongates from $2.7\,\text{nm}^{-1}$ at 2 K to $4.7\,\text{nm}^{-1}$ at 205 K in a 160 nm film, which corresponds to $\Delta Q = 0.99\,\text{nm}^{-1}$. The agreement between these two values suggests that T_s are due to discrete unwinding of the helix. This discrete behaviour is not expected from the thicker film in Reference [34] since

the field is applied out-of plane. Finite size effects are not relevant in this geometry which explains why a continuous change in Q is reported. It is unknown why this effect is not observed in the $M-H$ data as predicted in Reference [28] and Figure 4.3. A direct method of measuring the configuration of the helix, such as PNR, would be required to resolve this issue.

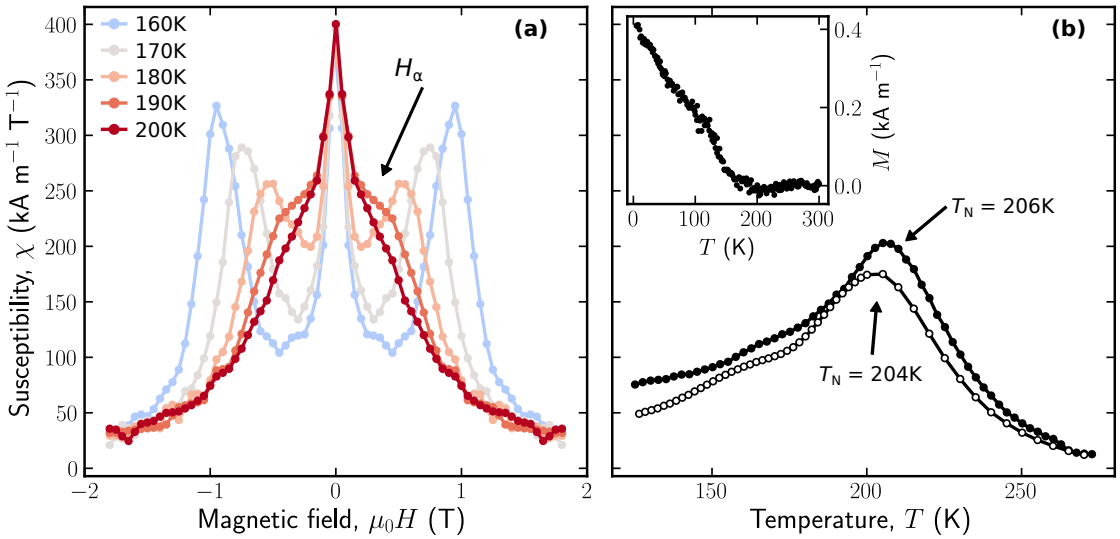

Figure 4.8: (a) Illustration of the disappearance of H_α in the 9.1 nm sample at temperatures near 200 K. (b) Susceptibility obtained from $M-T$ curves at low field, illustrating a peak near the ordering temperature. Filled (unfilled) circles are data from the 22.9 nm (16.4 nm) sample at 10 mT (100 mT). The inset is the remanent magnetization for the 22.9 nm sample.

The ordering temperature T_N of the MnGe films is difficult to systematically determine from the magnetometry data, although there are two ways in which an estimate can be obtained. The first is by recording the position of the maximum of the $M-T$ curve for sufficiently low fields. This is the temperature T_α. The field must be finite though, as measurements of the temperature-dependent remanent magnetization are not appropriate for the reasons discussed previously. This is the method that has been used in the literature and it agrees with the disappearence of magnetic order according to neutron diffraction and SANS [15, 17, 34, 47].

For the three samples studied, T_α was consistently found to be approximately 205 K, which migrates to lower temperatures above $\mu_0 H = 100$ mT. Estimates of T_N using this method are therefore only appropriate below $\mu_0 H = 100$ mT. The second

method involves analysis of the $M - H$ curves. The transition field H_α was found to disappear in the vicinity of 200 K (see Figure 4.8). This is consistent with the transition to a paramagnetic state and agrees with the $M - T$ curves.

The interesting fields from the $M - H$ and $M - T$ curves were combined to create a magnetic phase diagram for the films studied. This phase diagram is shown in Figure 4.9 and includes three main regions. Below H_{k_1}, MnGe films are in a Q_z helicoidal state. Above, H_{k_2}, the twisted ferromagnetic state is realized. Nominally at H_α, the system transitions from the Q_z helicoid into a twisted ferromagnet. The field-extent of this transition is given by $H_{k_2} - H_{k_1}$ and is also noted on the diagram. This is denoted as the transition region, where the helicoid is in the process of unwinding into the ferromagnetic phase.

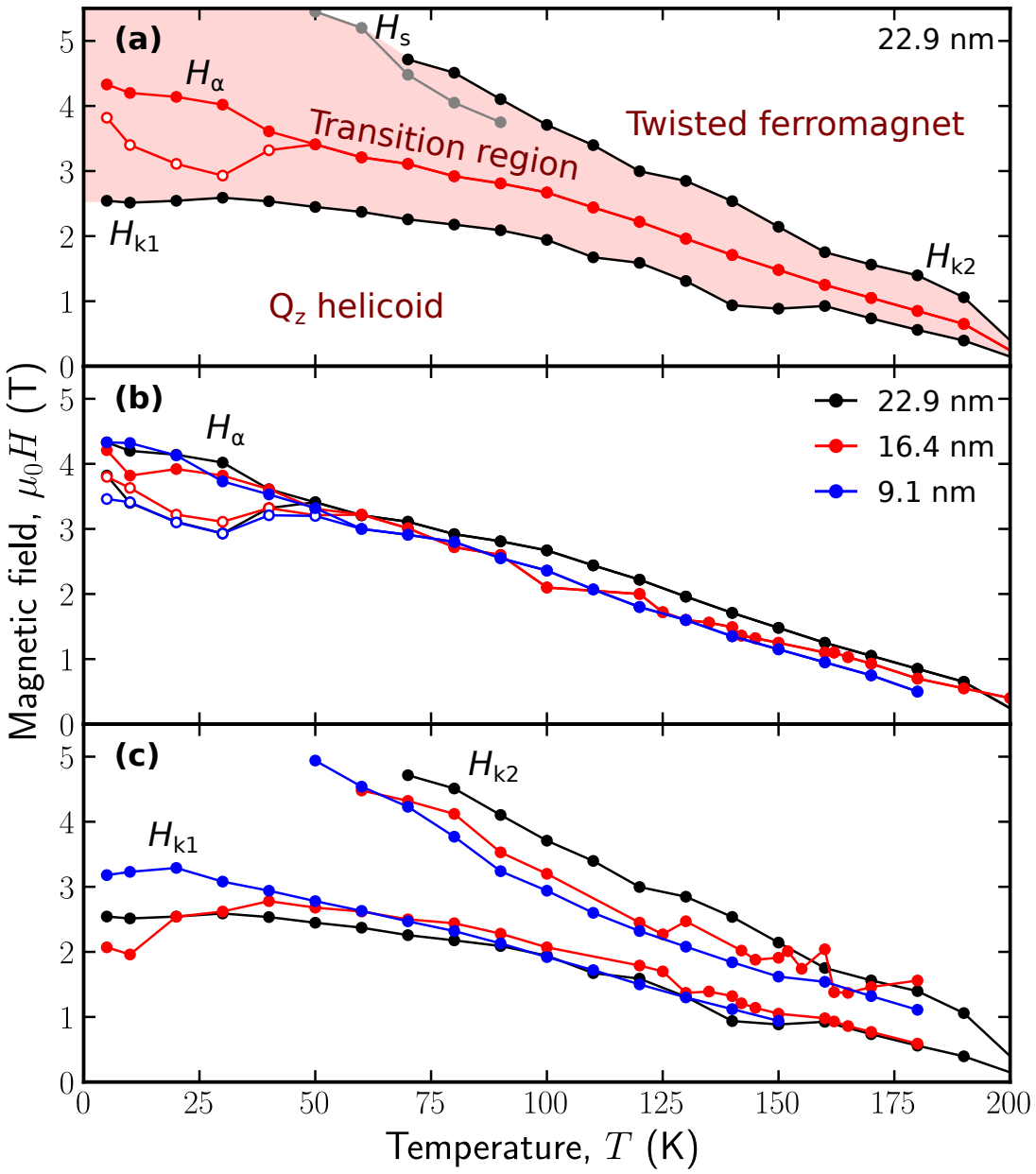

Figure 4.9: Magnetic phase diagram for in-plane fields. Closed circles are points measured at increasing fields and open circles are for decreasing fields. (a) Transitions for the 22.9 nm sample. Below H_{k_1}, the film is in a Q_z helicoid phase. Above H_{k_2}, the film is a twisted ferromagnet. The transition between these phases is nominally H_α but the width of the transition $H_{k_2} - H_{k_1}$ is shown in red. (b) The temperature dependence of H_α for the three thicknesses measured. (c) The temperature dependence of H_{k_1} and H_{k_2} for the three thicknesses measured.

Chapter 5

Magnetic characterization with H out-of-plane

This chapter reports on the magnetic response of MnGe thin films to an out-of-plane field. The magnetometry indicates a trivial conical phase which saturates into a ferromagnetic state. The transport measurements, on the other hand, reveal a state that is more complex than observed in the magnetometry.

5.1 SQUID magnetometry

SQUID magnetometry was also performed on the three samples with the field applied out of the plane. Again, data from the three samples was qualitatively similar and measurements presented here are representative of all three samples. Isothermal $M-H$ loops, and $M-T$ curves were recorded. For $M-H$ curves sample was field cooled at 7 T to the desired temperature. The out-of-plane moment was measured as the applied field was cycled to -7 T, then back to 7 T. It was found that the field at which the magnetization reaches its saturation value is much larger than for in-plane fields. For this reason, the magnetometry is most meaningful at higher temperatures, where this field is reduced. The low-temperature magnetization is still of interest, since the proposed triple-Q hedgehog state is said to occur at lower temperatures. The predicted phase boundary between the triple-Q and single-Q state occurs for fields less than 5 T for a 160 nm film. Evidence of a phase transition from the proposed triple-Q state to a single-Q should be accessible in the mangetometry.

It is again worth comparing with MnSi thin films, for which it was found that the ground state was a helicoid with $\mathbf{Q}$ along [111]. The application of a field parallel to [111] causes the spins to cant out of plane to align with the field and the system continuously evolves into the conical state. No evidence for an out-of-plane skyrmion phase found, due to the strong hard-axis anisotropy.

Representative $M-H$ curves for the 22.9 nm sample are shown in Figure 5.1. The curves have a linear region that flattens off after saturation, consistent with

MnSi thin films [28]. While the in-plane remanent magnetization was small, it is zero for these curves, for $M - H$ loops measured at temperatures where the saturation field is low enough to be reached with the 7 T magnet. At low temperatures where saturation is not reached, a small residual moment is found below 40 K. Although it is not clear what is the magnetic texture that is giving rise to this feature, a remanent out-of-plane moment is not expected from a Q_z helical state. For in-plane fields, the hysteresis disappeared at approximately the same temperature at which H_{k_2} became well-defined. Here, this happens at a lower temperature. The field at which the cone phase saturates is H_c. Below 120 K, this field was found to be greater than the maximum field of 7 T, as evidenced by the lack of a knee in the $M - H$ curves.

Interestingly, the plots of M versus H do not show any features other than H_c. A similar behaviour is actually reported in the magnetometry of the purported spin-hedgehog hosting 160 nm MnGe film (shown in the supplemental of Reference [34]). Modelling the magnetization versus field of a spin-hedgehog lattice is beyond the scope of this thesis, and is not found in the literature, although some papers have constructed a model of the spin structure from neutron diffraction data [36]. One must remark, however, that it seems unusual that the unwinding of a topologically non-trivial lattice of emergent monopoles and anti-monopoles into a topologically trivial conical state will occur with no signature in the magnetization. Simultaneous analysis of complementary techniques would be required to confirm the presence of this exotic state. Nonetheless, the magnetometry collected for this thesis does not suggest the presence of a phase transition. This will be further discussed in Section 5.2.

The saturation field H_c was determined from fitting the minimum of $\mathrm{d}^2M/\mathrm{d}H^2$. An illustration of this procedure is given in Figure 5.2. The differences between the $M - H$ loops for in-plane and out-of-plane fields are also detailed in Figure 5.2. As expected, the magnetization flattens off to the same value in both orientations. It was found that H_c was systematically larger than H_{k_2}, which is consistent with an out-of-plane hard-axis anisotropy. This was found with MnSi thin films under in-plane tensile strain, which is likely the case for these MnGe samples.

Interestingly, $M - T$ curves for out-of-plane field have a similar form to those for in-plane fields. The magnetization is small at low temperatures and there is a peak at the temperature at which the film exits the conical phase, T_c. There are no features

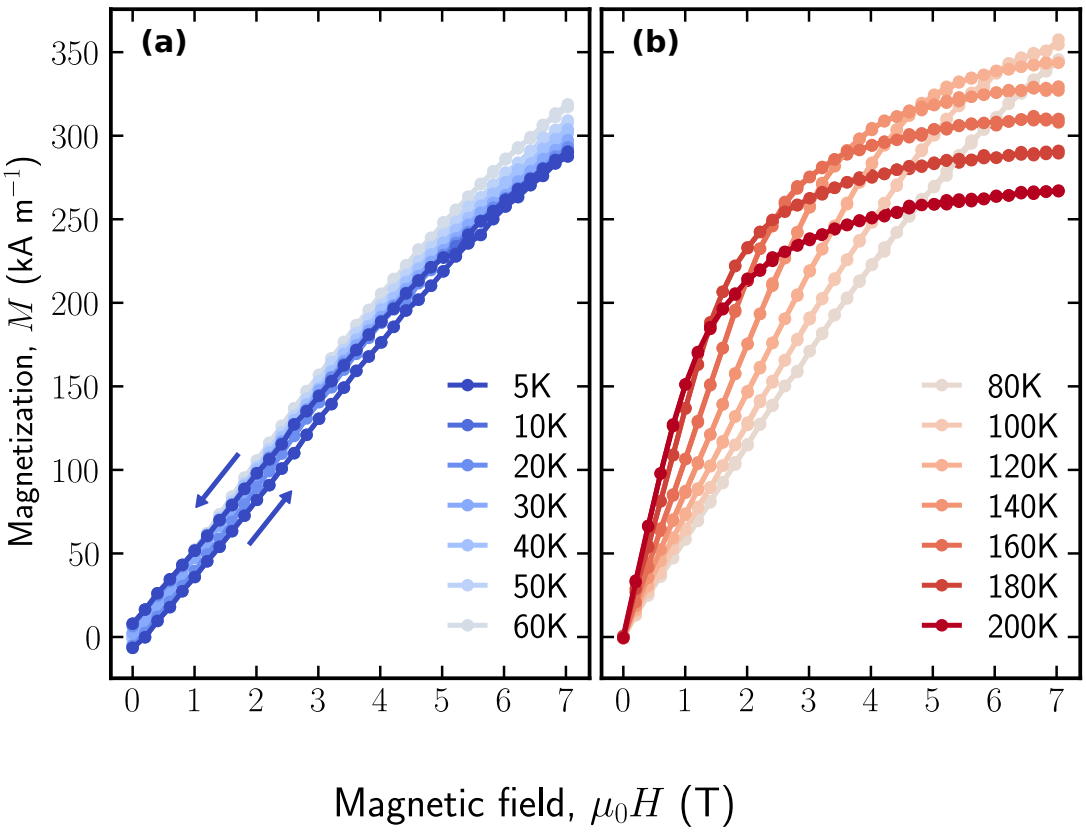

Figure 5.1: Representative $M - H$ loops at (a) low temperatures, and (b) high temperatures. Measurements shown for the 22.9 nm sample with field applied in-plane. There is hysteresis present at low temperatures. The arrows in (a) indicate whether the field is increasing or decreasing. Above 60 K, the two branches lie on top of each other.

at low temperatures, which is in agreement with the M versus H loops. Furthermore, T_c and H_c are in agreement between isothermal and isomagnetic measurements.

5.2 Magnetotransport

The longitudinal and Hall resistivities were measured for out-of-plane fields for the 22.9 nm and 16.4 nm samples. The resistivity of the substrate was substantially larger than that of the film, so this technique only (to good approximation) probes the film. Electronic transport in a magnetic material is strongly influenced by its magnetic phase. In the same way that features in the magnetization can be used to detect magnetic phase transitions, the resistivity can also be used. The $\rho - H$ loops were

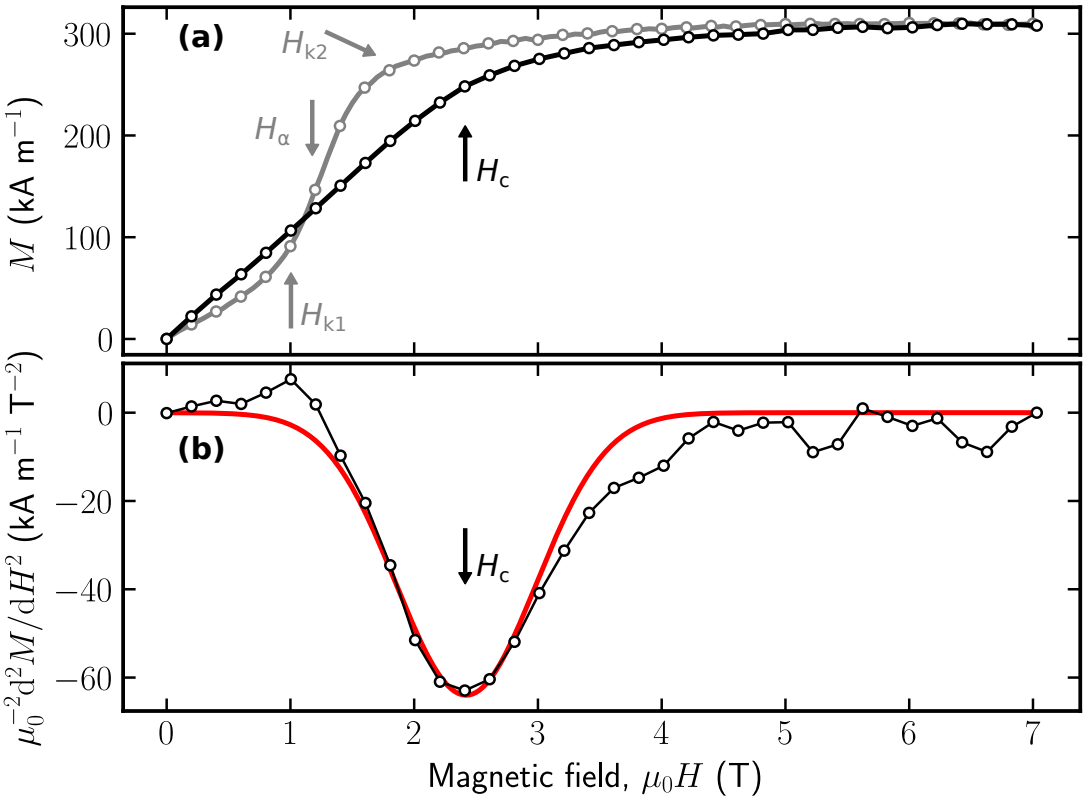

Figure 5.2: Determination of out-of-plane saturation field H_c. (a) A representative magnetization curve is at 160 K is shown in black (grey) circles for the magnetic field out-of-plane (in-plane). The transitions are labelled. The second derivative of the out-of-plane magnetization $\mathrm{d}^2M/\mathrm{d}H^2$ is shown in (b). The red line is a Gaussian fit used to find the minimum.

recorded by field cooling the sample at 14 T and cycling the field to −14 T, and back. The data was symmetrized according to Equations 2.22 and 2.23. For the $\rho - T$ measurement, the sample was field cooled at 14 T and the resistivity was measured at zero field on warming. The sample was then field cooled at −14 T and the zero field resistivity was again measured on warming. These two curves were used for symmetrization. Like magnetometry, the behaviour of the resistivity was qualitatively similar in the two samples measured.

Figure 5.4 shows the longitudinal and Hall resistivity as a function of temperature for the 22.9 nm sample. The longitudinal resistivity is presented as $\rho_{xx}^{\mathrm{rel}} = \rho_{xx}(T)/\rho_{xx}(T = 5\,\mathrm{K})$ for reasons discussed in Section 2.5.

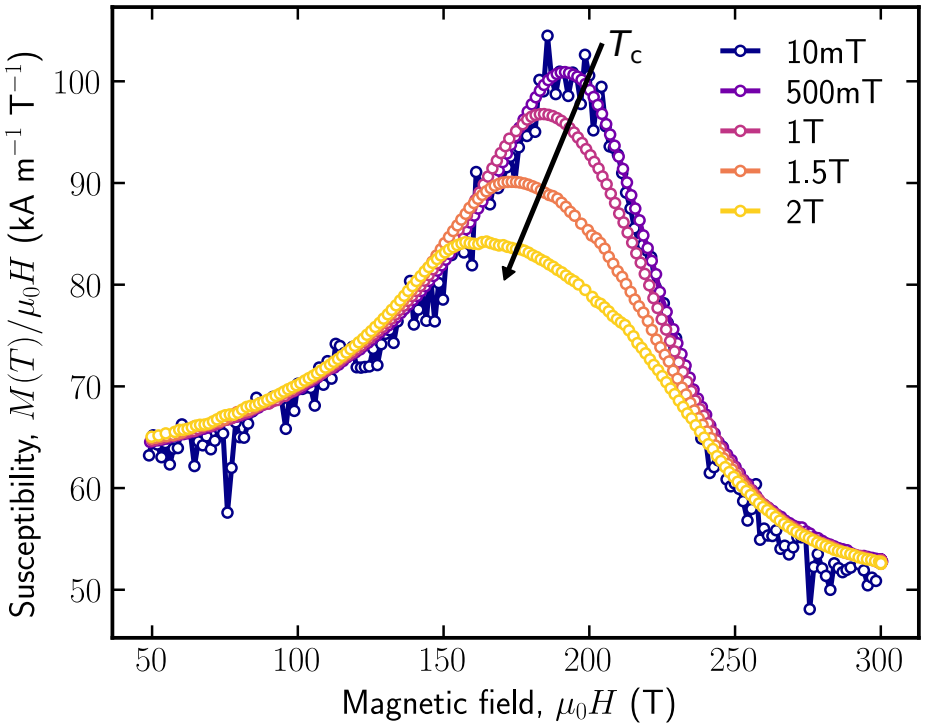

Figure 5.3: Field-normalized $M/\mu_0 H$-T curves for the 9.1 nm sample. The field is applied parallel to the [111] direction. The peak in the magnetization corresponds to the film entering a field-induced ferromagnetic phase from the cone phase.

The residual resistivity ratio (RRR) is commonly used in the literature as a measure of the defect scattering in the sample. It was found for the 22.9 nm and 16.4 nm samples that the RRR was 4.9 and 6.9, respectively. The RRR for the MnGe single crystal in and thin film in References [39] and [49] were approximately 14 and 47, respectively. The MnGe films are likely to have an equal amount of opposite chiral domains, as has been seen with other B20 thin films. The fact that Reference [49] reports a higher RRR for a film (which was shown with TEM to exhibit chiral domains) than for a single crystal likely rules out these domains as a cause for the low RRR observed. The defects evidenced by the RRR may be caused by a deviation in the Mn:Ge stoichiometry. If the Mn:Ge ratio is different from 1:1, this would manifest in deviations in the electron density determined from XRR (which deviated from

the bulk value in some samples). The stoichiometry can be estimated from the refined XRR densities, but this is difficult to decouple from the effect of strain-induced changes in the unit cell volume. The in-plane strain could not be determined by XRD and require TEM meeasurements. A future study should measure the composition of the films to ascertain the origin of the low RRR.

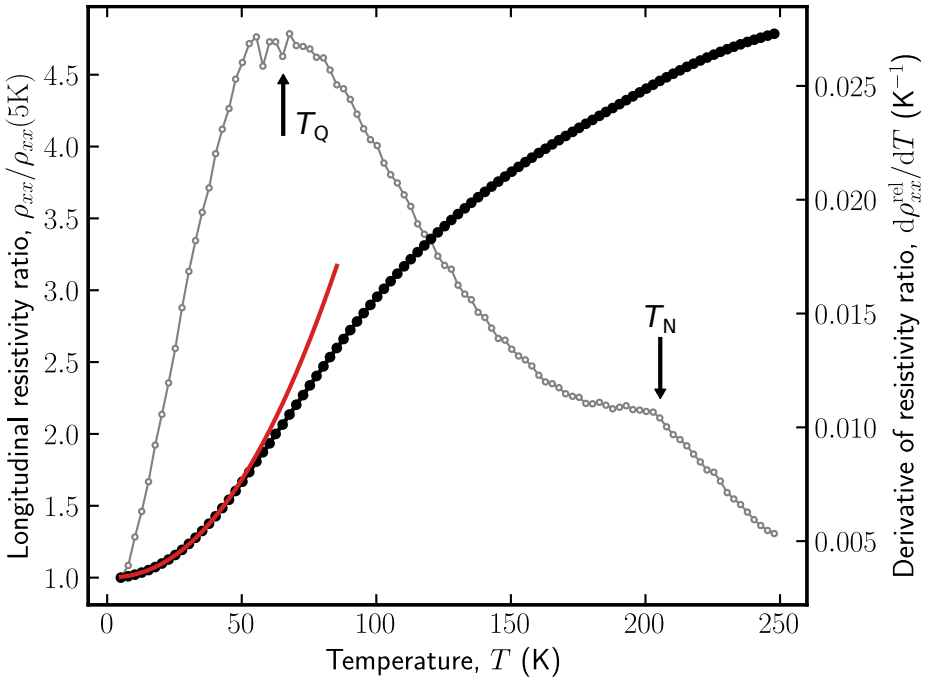

Figure 5.4: Longitudinal resistivity ratio (black circles; left axis) and its derivative (grey circles; right axis) versus temperature for the 22.9 nm sample. The red curve is a power law fit fit used to extrapolate to $T = 0\,\mathrm{K}$. The derivative has two features: one at 63 K labelled T_{Q}, and another at the ordering temperature T_{N} of 205 K.

The temperature dependence of the longitudinal resistivity ratio is given in Figure 5.4. There is a feature in the resistivity ratio at $T = 205\,\mathrm{K}$, which is in excellent agreement with the ordering temperature $T_{\mathrm{N}} = 206\,\mathrm{K}$ as estimated by magnetometry. There is an additional broad peak which occurs at $T = 63\,\mathrm{K}$, which is labelled as T_{Q}.

At temperatures below approximately 50 K, a power law of the form

$$\rho_{xx}(T)/\rho_{xx}(T = 5\,\mathrm{K}) = \kappa_0 T^{\kappa} + 1\,, \tag{5.1}$$

was fit to the data. The exponent was found to be $\kappa = 2.16$ for the 22.9 nm sample and $\kappa = 2.14$ for the 16.4 nm sample. This indicates that MnGe thin films exhibit

Fermi liquid-like behaviour, which is characterized by an exponent $\kappa = 2$.

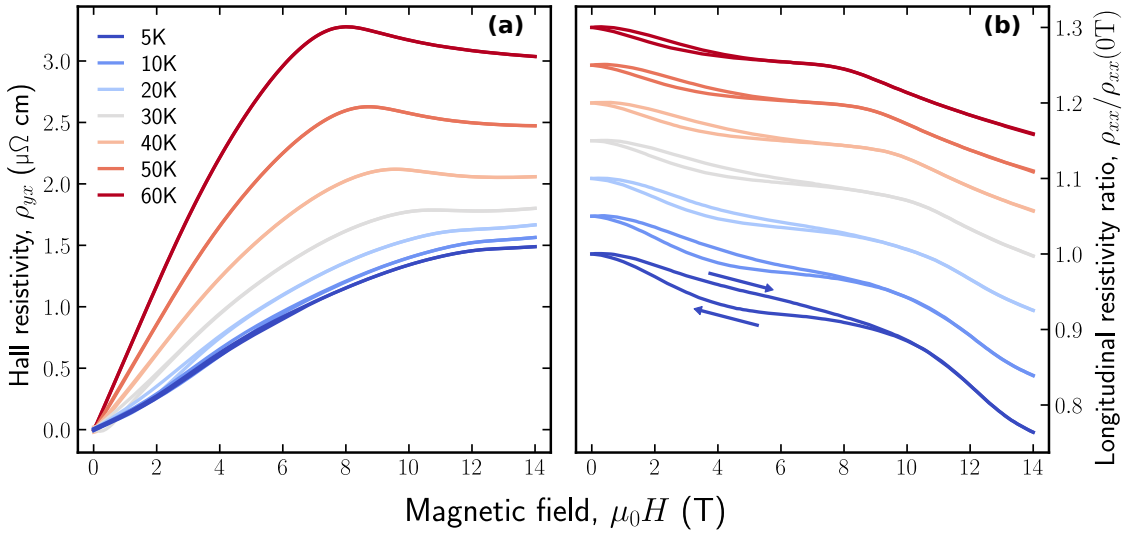

Figure 5.5: (a) Transverse and (b) longitudinal resistivity versus field for the 16.4 nm sample. Hysteresis is evident in all temperatures presented here, despite the cone saturation field H_c being reached. Curves in (b) are offset by 0.05 for clarity. The arrows indicate whether the field is increasing or decreasing.

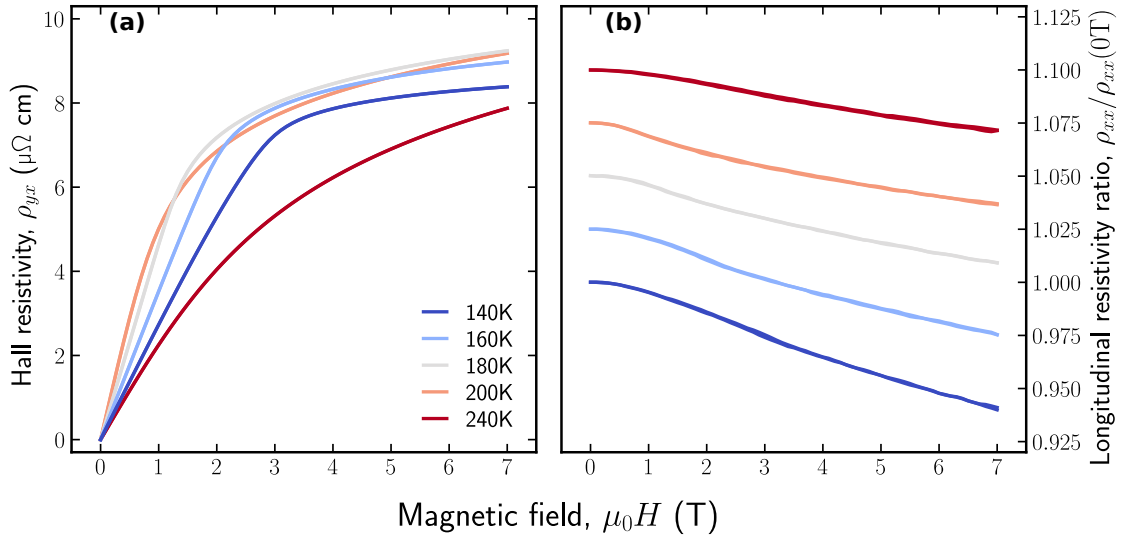

Figure 5.6: (a) Transverse and (b) longitudinal resistivity versus field for the 16.4 nm sample. At the high temperatures shown here, there is no hysteresis or features other than H_c. The $T = 240$ K curve is taken above the ordering temperature and exhibits behaviour characteristic to the resistivity of a paramagnet, and does not exhibit H_c.

Representative ρ versus H curves are shown in Figures 5.5 and 5.6 for the 16.4 nm sample. There is significant hysteresis exhibited below $T = 60\,\mathrm{K}$. This is contrary to the lack of hysteresis found in magnetometry for out-of-plane fields. Anomalies in the Hall resistivity have been used to infer the presence of a topological spin-hedgehog phase despite trivial magnetometry curves in Reference [34]. This Hall resistivity is also much larger than what was found for MnSi thin films (on the order of tens of $\mathrm{n\Omega\,cm}$) which was attributed to the cone phase [78].

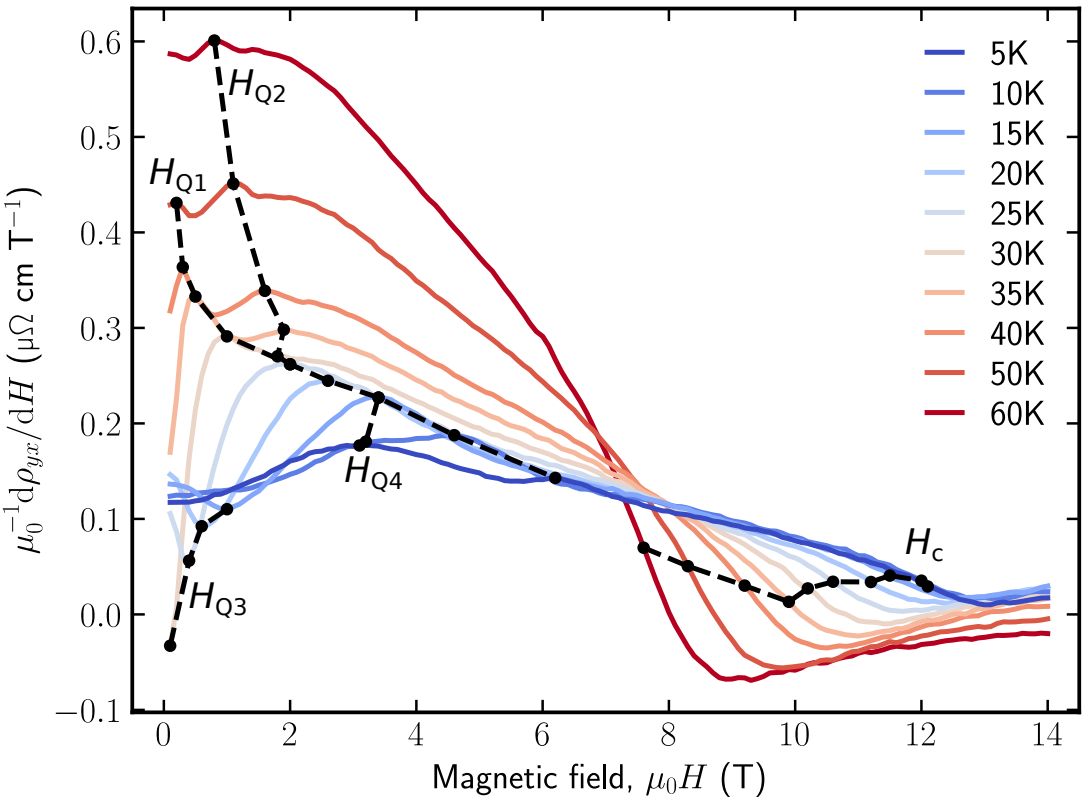

Figure 5.7: Derivative of the Hall resistivity versus magnetic field for the 16.4 nm sample. Various phase boundaries are indicated by the black dots and the dashed lines are a guide to the eye. The cone to ferromagnetic transition H_c was determined from minima in $\mathrm{d}^2\rho_{yx}/\mathrm{d}H^2$ and the four H_Q transitions were found from peaks in $\mathrm{d}\rho_{yx}/\mathrm{d}H$. The H_Q were grouped according to the similar form of their peaks in $\mathrm{d}\rho_{yx}/\mathrm{d}H$.

The derivative of the resistivity was used to search for magnetic phase transitions. A minimum in the second derivative $\mathrm{d}^2\rho_{yx}/\mathrm{d}H^2$ was used to determine the saturation field H_c, in a similar fashion to the magnetometry curves. Unlike the magnetometry,

interesting features appeared in derivatives of the Hall resistivity. These only occured in the increasing branches of ρ_{yx}. Plots of $\mathrm{d}\rho_{yx}/\mathrm{d}H$ for the 16.4 nm sample are given in Figure 5.7. Apart from H_{c}, several sets of peaks were found. These are labelled H_{Q_1}, H_{Q_2}, H_{Q_3} and H_{Q_4} since they coincide with the phase boundary that is claimed in References [34, 48] to be a triple-Q hedgehog lattice.

The evolution of these critical fields with temperature is annotated on the figure. The form of the phase boundary H_{Q_1} is similar to what has been previously reported for MnGe thin films, but the additional transitions observed have not been reported in the literature. The presence of H_{Q_2}, H_{Q_3} and H_{Q_4} may indicate a partitioning of the disputed low-field, low-temperature phase which only occurs for very thin films, like those studied in this thesis.

The magnetic phase transitions detected by SQUID magnetometry and magnetoresistivity have been summarized into a phase diagram for out-of-plane fields in Figure 5.8. The pocket below H_{Q_1} is comparable to the pocket attributed to the spin-hedgehog lattice in References [34, 48], although this region has also been interepreted as a multi-domain helicoid state in multiple studies [40, 41, 42, 43, 44]. The measurements performed for this thesis have not directly probed the magnetic structure of this phase and it is therefore impossible to conclude which of these interpretations is correct. This pocket will be labelled as the Q-phase and future studies should determine the origin of the observed anomalies in the Hall resistivity, as well as an explanation for the lack of such anomalies in the magnetometry data. The region between H_{Q_1} and H_{c} is inferred to be a conical phase upon comparison to the literature for both MnGe and other B20 compounds.

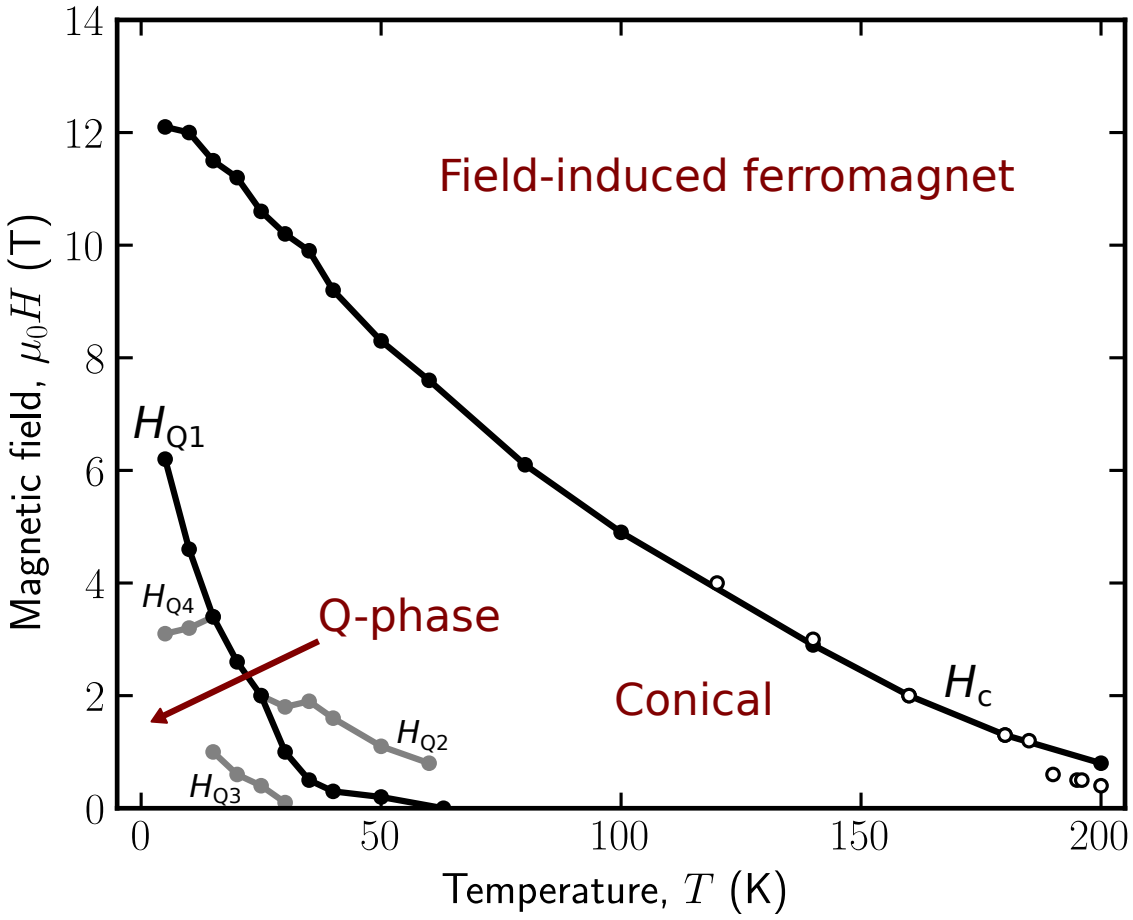

Figure 5.8: Magnetic phase diagram for out-of-plane fields. Transitions shown here are for the 16.4 nm sample. The filled circles are determined from the Hall resistivity and the unfilled circles are from magnetometry. The field-induced ferromagnet phase is separated from the single-Q conical phase by the transition H_c. The various H_Q transitions separate the conical phase from the Q-phase. The Q-phase may be either a spin-hedgehog lattice, or multi-domain helicoid phase.

Chapter 6

Conclusion

A novel approach was taken to fabricate epitaxial MnGe thin films on a non-magnetic template layer of B20 CrSi. *In-situ* RHEED and *ex-situ* AFM reveal that the 5 Å template crystallizes in a uniform layer with high coverage and a roughness commensurate to the Si(111) substrate. Low-temperature (100 °C) co-deposition of Mn and Ge at stoichiometric ratios, followed by annealing to 250 °C was found to give the best epitaxy. The MnGe films exhibited interfacial roughnesses of less than 5 Å in some samples found by *ex-situ* XRR across a wide range of film thicknesses.

Though the films exhibit low interfacial roughness, steps should be taken to improve the RRR. It has been demonstrated that Mn-rich impurity phases can be annealed out in the presence of excess Ge, so it may be possible to improve the RRR with a different annealing procedure.

The first study of the magnetism of MnGe(111) thin films with an in-plane applied field was conducted. SQUID magnetometry data suggests that a helicoid phase transitions into a twisted ferromagnetic state, evidenced by an abrupt first-order-like jump in the magnetization. The static susceptibility exhibits a large peak at this magnetic fields corresponding to this transition. The lack of any other peaks in the susceptibility versus field rules out the possibility of an in-plane skyrmion phase for film thicknesses of 22.9 nm, 16.4 nm and 9.1 nm.

Since the literature suggests that skyrmions may be suppressed for certain film thicknesses (depending on the helical pitch), further magnetometry measurements should be performed. A comprehensive analysis of the magnetism over many film thicknesses is needed to definitively conclude whether or not in-plane skyrmions can exist in MnGe thin films. To augment this analysis, future studies should aim to measure the pitch of the helix using PNR, and its temperature dependence. Oscillations in low field $M-T$ measurements should be compared to micromagnetic modelling to support the hypothesis that these are due to temperature-driven helical unwinding.

This modelling will be much easier to perform once PNR measurements have been completed, which will enable a determination of the exchange and DMI in this material. The lack of a field-driven helical unwinding, like seen in MnSi films should also be addressed.

Out-of-plane magnetometry revealed only the transition from a conical phase to a field-polarized ferromagnet. There was no evidence for an out-of-plane skyrmion phase, or a triple-Q state at low temperature. Transport measurements, on the other hand, reveal an additional low-temperature transition. The location of this transition on the magnetic phase diagram is in agreement with the proposed spin-hedgehog phase reported by Kanazawa *et al* for a thicker MnGe film. This work identifies the phase boundary, but does not report on its magnetic structure. The study of this phase is an interesting avenue for future experiments.

The films show a reduction in the saturation magnetization relative to bulk. Strain and film composition could be responsible for this. Measurements of the film composition should be performed and correlated with RRR from transport and electron densities obtained from the reflectometry critical angle. Both strain and film stoichiometry affect the electronic structure, which would impact both the exchange and DMI, and so could impact the helical wavelength.

Subsequent studies can build upon these results and, the growth recipe may also be repurposed in an attempt to stabilize other metastable B20 structures. The behaviour of MnGe thin films has been shown to be vastly different from MnSi, which begs for further investigation into the applicability of the model used to describe B20 chiral magnets.

Bibliography

[1] M. N. Baibich, *et al.* Giant magnetoresistance of (001)Fe/(001)Cr magnetic superlattices. *Physical Review Letters*, **61** 2472 (1988)

[2] G. Binasch *et al.* Enhanced magnetoresistance in layered magnetic structures with antiferromagnetic interlayer exchange. *Physical Review B*, **39** 4828 (1989)

[3] L. Berger. Low-field magnetoresistance and domain drag in ferromagnets. *Journal of Applied Physics*, **49** 2156 (1978)

[4] P.P. Freitas and L. Berger. Observation of s-d exchange force between domain walls and electric current in very thin permalloy films. *Journal of Applied Physics*, **57** 1266 (1985)

[5] I.N. Krivorotov *et al.* Time-domain measurements of nanomagnet dynamics driven by spin-transfer torques. *Science*, **307** 228 (2005)

[6] M. Yamanouchi *et al.* Current-induced domain-wall switching in a ferromagnetic semiconductor structure. *Nature*, **428** 539 (2004)

[7] X. Z. Yu *et al.* Skyrmion flow near room temperature in an ultralow current density. *Nature Communications*, **3** 988 (2012)

[8] S. S. P. Parkin, M. Hayashi, and L. Thomas. Magnetic domain-wall racetrack memory. *Science*, **320** 190 (2008)

[9] R. Tomasello, *et al.* A strategy for the design of skyrmion racetrack memories. *Scientific Reports*, **4** 1 (2014)

[10] K. M. Song *et al.* Skyrmion-based artificial synapses for neuromorphic computing. *Nature Electronics*, **3** 148 (2020)

[11] J. Kishine, I. V. Proskurin, and A. S. Ovchinnikov. Tuning magnetotransport through a magnetic kink crystal in a chiral helimagnet. *Physical Review Letters.*, **107** 017205 (2011)

[12] I. G. Bostrem, J. Kishine, and A. S. Ovchinnikov. Theory of spin current in chiral helimagnets. *Physical Review B*, **78** 064425 (2008)

[13] A. B. Borisov, *et al.* Magnetic soliton transport over topological spin texture in chiral helimagnet with strong easy-plane anisotropy. *Physical Review B*, **79** 134436 (2009)

[14] H Takizawa *et al.* High-pressure synthesis and electrical and magnetic properties of MnGe and CoGe with the cubic B20 structure. *Journal of Solid State Chemistry*, **73** 40 (1988)

[15] O. L. Makarova *et al.* Neutron diffraction study of the chiral magnet MnGe. *Physical Review B*, **85** 205205 (2012)

[16] K. Momma and F. Izumi. VESTA 3 for three-dimensional visualization of crystal, volumetric and morphology data. *Journal of Applied Crystallography*, **44** 1272 (2011)

[17] N. Kanazawa *et al.* Large topological hall effect in a short-period helimagnet MnGe. *Physical Review Letters*, **106** 156603 (2011)

[18] P. Bak and M. H. Jensen. Theory of helical magnetic structures and phase transitions in MnSi and FeGe. *Journal of Physics C: Solid State Physics*, **13** L881 (1980).

[19] S. Chikazumi. *Physics of ferromagnetism.* Oxford University Press, 1997.

[20] I. E. Dzyaloshinskii. Theory of helicoidal structures in antiferromagnets. *Soviet Physics, Journal of Experimental and Theoretical Physics*, **19** 960 (1964).

[21] U. K. Rößler, A. A. Leonov, and A. N. Bogdanov. Chiral skyrmionic matter in non-centrosymmetric magnets. In *Journal of Physics: Conference Series*, **303**, 012105 (2011).

[22] N. A. Porter *et al.* Manipulation of the spin helix in FeGe thin films and FeGe/Fe multilayers. *Physical Review B*, **92** 144402 (2015)

[23] M. N. Wilson *et al.* Discrete helicoidal states in chiral magnetic thin films. *Physical Review B*, **88** 214420 (2013)

[24] S. A. Meynell *et al.* Surface twist instabilities and skyrmion states in chiral ferromagnets. *Physical Review B*, **90** 014406 (2014)

[25] A. N. Bogdanov and D. A. Yablonskii. Thermodynamically stable "vortices" in magnetically ordered crystals. the mixed state of magnets. *Soviet Physics, Journal of Experimental and Theoretical Physics*, **95** 178 (1989)

[26] U. K. Rößler, A.N. Bogdanov, and C. Pfleiderer. Spontaneous skyrmion ground states in magnetic metals. *Nature*, **442** 797 (2006)

[27] S. Mühlbauer *et al.* Skyrmion lattice in a chiral magnet. *Science*, **323** 915 (2009)

[28] M. N. Wilson *et al.* Chiral skyrmions in cubic helimagnet films: The role of uniaxial anisotropy. *Physical Review B*, **89** 094411 (2014)

[29] H. Wilhelm *et al.* Confinement of chiral magnetic modulations in the precursor region of FeGe. *Journal of Physics: Condensed Matter*, **24** 294204 (2012)

[30] F.N. Rybakov, A. B. Borisov, and A.N. Bogdanov. Three-dimensional skyrmion states in thin films of cubic helimagnets. *Physical Review B*, **87** 094424 (2013)

[31] C. D. Rudderham, M. L. Plumer, and T. L. Monchesky. The influence of film thickness and uniaxial anisotropy on in-plane skyrmions: Numerical investigations of the phase space of chiral magnets. *arχiv preprint arχiv:2309.12419* (2023)

[32] T. Tanigaki *et al.* Real-space observation of short-period cubic lattice of skyrmions in MnGe. *Nano Letters*, **15** 5438 (2015)

[33] N. Kanazawa, *et al.* Critical phenomena of emergent magnetic monopoles in a chiral magnet. *Nature Communications*, **7** 11622 (2016)

[34] N. Kanazawa *et al.* Topological spin-hedgehog crystals of a chiral magnet as engineered with magnetic anisotropy. *Physical Review B*, **96** 220414 (2017)

[35] A. B. Gokhale and R. Abbaschian. The Ge-Mn (germanium-manganese) system. *Journal of Phase Equilibria*, **11** 460 (1990)

[36] V. Pomjakushin *et al.* Topological magnetic structures in MnGe: Neutron diffraction and symmetry analysis. *Physical Review B*, **107** 024410 (2023)

[37] N. Kanazawa *et al.* Possible skyrmion-lattice ground state in the B20 chiral-lattice magnet MnGe as seen via small-angle neutron scattering. *Physical Review B*, **86** 134425 (2012)

[38] N. Kanazawa *et al.* Direct observation of the statics and dynamics of emergent magnetic monopoles in a chiral magnet. *Physical Review Letters*, **125** 137202 (2020)

[39] A. Kitaori *et al.* Enhanced electrical magnetochiral effect by spin-hedgehog lattice structural transition. *Physical Review B*, **103** L220410 (2021)

[40] M. Deutsch *et al.* Stress-induced magnetic textures and fluctuating chiral phase in MnGe chiral magnet. *Physical Review B*, **90** 144401 (2014)

[41] E. Altynbaev *et al.* Hidden quantum phase transition in $Mn_{1-x}Fe_xGe$ evidenced by small-angle neutron scattering. *Physical Review B*, **94** 174403 (2016)

[42] A. Yaouanc *et al.* Magnetic structure of the MnGe helimagnet and representation analysis. *Physical Review B*, **95** 174422 (2017)

[43] E. Altynbaev *et al.* Magnetic structure in $Mn_{1-x}Co_xGe$ compounds. *Physical Review B*, **97** 144411 (2018)

[44] N. Martin *et al.* Partial ordering and phase elasticity in the MnGe short-period helimagnet. *Physical Review B*, **99** 100402 (2019)

[45] N. Martin *et al.* Magnetic ground state and spin fluctuations in MnGe chiral magnet as studied by muon spin rotation. *Physical Review B*, **93** 174405 (2016)

[46] R. Viennois *et al.* Observation of various magnetic-field–induced states in B20 cubic MnGe. *Europhysics Letters*, **111** 17008 (2015)

[47] J. Engelke, D. Menzel, and V. A. Dyadkin. Thin film MnGe grown on Si (111). *Journal of Physics: Condensed Matter*, **25** 472201 (2013)

[48] Y. Fujishiro *et al.* Giant anomalous Hall effect from spin-chirality scattering in a chiral magnet. *Nature Communications*, **12** 317 (2021)

[49] Y. Hayashi *et al.* Magneto-optical spectroscopy on Weyl nodes for anomalous and topological Hall effects in chiral MnGe. *Nature Communications*, **12** 5974 (2021)

[50] T. Koretsune, N. Nagaosa, and R. Arita. Control of Dzyaloshinskii-Moriya interaction in $Mn_{1-x}Fe_xGe$: a first-principles study. *Scientific Reports*, **5** 13302 (2015)

[51] T. Koretsune, T. Kikuchi, and R. Arita. First-principles evaluation of the Dzyaloshinskii-Moriya interaction. *Journal of the Physical Society of Japan*, **87** 041011 (2018)

[52] S. Mankovsky *et al.* Composition-dependent magnetic response properties of $Mn_{1-x}Fe_xGe$ alloys. *Physical Review B*, **97** 024403 (2018)

[53] J. Gayles *et al.* Dzyaloshinskii-moriya interaction and hall effects in the skyrmion phase of $Mn_{1-x}Fe_xGe$. *Physical Review Letters*, **115** 036602 (2015)

[54] M. Bornemann *et al.* Complex magnetism of B20-MnGe: from spin-spirals, hedgehogs to monopoles. *Journal of Physics: Condensed Matter*, **31** 485801 (2019)

[55] S. Grytsiuk *et al.* Topological–chiral magnetic interactions driven by emergent orbital magnetism. *Nature Communications*, **11** 511 (2020)

[56] E. Mendive-Tapia *et al.* Short period magnetization texture of B20-MnGe explained by thermally fluctuating local moments. *Physical Review B*, **103** 024410 (2021)

[57] I.Z. Radovskii *et al.* The magnetic susceptibility of chromium silicides. *Soviet Powder Metallurgy and Metal Ceramics*, **4** 115 (1965)

[58] A. K. Mishra *et al.* Transport and calorimetric properties of CrSi. *AIP Conference Proceedings*, **2115** 030436 (2019)

[59] Y. Kousaka *et al.* Weak ferromagnetism in chiral inorganic compound CrSi. In *JPS Conference Proceedings (SCES2013)*, **3** 014037 (2014)

[60] P. Wetzel *et al.* Formation of CrSi and $CrSi_2$ upon annealing of Cr overlayers on Si(111). *Physical Review B*, **35** 5880 (1987)

[61] P. Wetzel *et al.* Epitaxial growth of CrSi and $CrSi_2$ on Si(111). *Solid State Communications*, **65** 1217 (1988)

[62] E. A. Karhu *et al.* Structure and magnetic properties of MnSi epitaxial thin films. *Physical Review B*, **82** 184417 (2010)

[63] U. W. Pohl. *Epitaxy of semiconductors: physics and fabrication of heterostructures*. Springer Nature, 2020.

[64] S. Matteucci *et al.* Transport of gases and vapors in glassy and rubbery polymers. *Materials science of membranes for gas and vapor separation*, 2006.

[65] N. W. Ashcroft and N. D. Mermin. *Solid state physics*. Cengage Learning, 1977.

[66] E. A. Karhu. Structural and magnetic properties of epitaxial MnSi(111) thin films. 2012.

[67] A. Boulle, R. Guinebretière, and A. Dauger. X-ray diffraction from epitaxial thin films: an analytical expression of the line profiles accounting for microstructure. *Zeitschrift für Kristallographie*, **23** 123 (2006)

[68] S. Hasegawa. Reflection high-energy electron diffraction. *Characterization of Materials*, **97** 1925 (2012)

[69] B. Heinrich, and J .A .C. Bland. *Ultrathin Magnetic Structures II: Measurement Techniques and Novel Magnetic Properties*, 1994.

[70] J. Daillant and A. Gibaud. *X-ray and neutron reflectivity: principles and applications*, 2008.

[71] A. Glavic and M. Björck. Genx 3: the latest generation of an established tool. *Journal of Applied Crystallography*, **55** 1063 (2022)

[72] B. D. Josephson. Possible new effects in superconductive tunnelling. *Physics Letters*, **1** 251 (1962)

[73] R. Doll and M. Näbauer. Experimental proof of magnetic flux quantization in a superconducting ring. *Physical Review Letters*, **7** 51 (1961)

[74] P. W. Anderson and J. M. Rowell. Probable observation of the Josephson superconducting tunneling effect. *Physical Review Letters*, **10** 230 (1963)

[75] S. A. Meynell *et al.* Neutron study of in-plane skyrmions in MnSi thin films. *Physical Review B*, **96** 054402 (2017)

[76] E. A. Karhu *et al.* Helical magnetic order in MnSi thin films. *Physical Review B*, **84** 060404 (2011)

[77] M. N Wilson *et al.* Extended elliptic skyrmion gratings in epitaxial MnSi thin films. *Physical Review B*, **86** 144420 (2012)

[78] M. N. Wilson. Magnetic skyrmion phase in MnSi thin films. 2013.